
University of Glasgow

# Split Ring Resonator (SRR) based Metamaterials

**A thesis for the degree of**
**Doctor of Philosophy (Ph.D.),**
**submitted to the Faculty of Engineering,**
**University of Glasgow**

**By**

Basudev Lahiri

Department of Electronics and Electrical Engineering

# Abstract

Metamaterials are artificial materials that are known to produce extraordinary electromagnetic responses, due to their constituent artificially-engineered micro- or nanostructures with dimensions smaller than that of the wavelength of light. The Split Ring Resonator (SRR) is one such nanostructure that forms the basic unit of a metamaterial. Since the dimensions of the SRRs are required to be smaller than the resonance wavelength, they become critical when a response is required at near infrared and optical wavelengths. In this thesis the various properties are studied of nanoscale SRRs that resonate in the infrared and visible spectrum. The SRRs studied in this thesis are made of both aluminium (Al) and gold (Au) and have been fabricated on silicon and silica substrates using electron beam lithography (EBL) techniques.

The effect of the different properties of metals (Al and Au) on the resonances of SRRs is studied. A substantial shift is reported in the response of arrays of similarly sized SRRs, made respectively of aluminium and of gold. It is shown that, by using aluminium based SRRs instead of gold ones; the magnetic resonance of SRRs can be shifted well into the visible spectrum. The effects of titanium adhesion layers on the properties of SRRs are considered and it is shown that even a 2 nm thick layer of titanium can red-shift the SRR resonance by 20 nm.

It is shown that, by adding asymmetry between the geometries of similar size, doubly-split SRRs, it is possible to produce a steeper resonance response, thereby increasing the quality factor of the SRRs. This steep response of these asymmetric split ring resonators (A-SRRs) is utilised for the optical detection of very thin films of organic compounds. It is further shown that by localising the organic compound to specific regions of the A-SRRs, a considerable enhancement in the sensitivity of optical detection can be achieved. Finally, essentially the same property of A-SRRs is utilised for the enhanced detection of, and differentiation between, different strands of DNA.

# List of publications from this thesis

### Peer reviewed journal publications

1. **Basudev Lahiri**, Ali Z. Khokhar, Richard M. De La Rue1, Scott G. McMeekin and Nigel P. Johnson, "Asymmetric split ring resonators for optical sensing of organic materials," Optics Express. Vol. 17, No. 2, 1107-1115, 19 Jan 2009. *(Also appeared in the Virtual Journal for Biomedical Optics).*

2. **Basudev Lahiri**, Scott G. McMeekin, Ali Z. Khokhar, Richard M. De La Rue and Nigel. P. Johnson, "Magnetic response of split ring resonators (SRRs) at visible frequencies," Optics Express. Vol. 18, No. 3, 3210-3218, 1st Feb 2010.

3. **Basudev Lahiri**, Rafal Dylewicz, Richard M. De La Rue, and Nigel P. Johnson, "Impact of titanium adhesion layers on the response of metallic split-ring resonators (SRRs)," Optics Express. Vol. 18, No. 10 (05/10/2010).

4. Rafal Dylewicz **, Basudev Lahiri**, Richard M. De La Rue, and Nigel P. Johnson, "Tuning of material properties in simulations of single and dual-layer metallic split ring resonators," *in preparation.*

5. **Basudev Lahiri**, Huabing Yin, Richard M. De La Rue and Nigel P. Johnson, "Asymmetric nano-antennas for the label-free detection of DNA oligonucleotides," *in preparation.*

**Conference publications**

1. A. Z. Khokhar, S. G. McMeekin, **B. Lahiri**, R. M. De La Rue and N. P. Johnson, "Investigating Split Ring Resonators from 1.3 to 10 microns," Optics and Optoelectronics, Proc. SPIE Vol.6581, 65816, Prague, 16 April 2007.

2. S. G. McMeekin, A. Z. Khokhar, **B. Lahiri**, R. M. De La Rue and N. P. Johnson, "Analysis of Split Ring Resonators Using Conformal Mapping Techniques", Optics and Optoelectronics, Proc. SPIE Vol. 6581, 65810V, 4 May 2007.

3. Nigel P. Johnson, Ali Z. Khokhar, Scott G McMeekin, **Basudev Lahiri**, Richard M. De La Rue, Ahmad R. Md Zain, C. Debus, and P. Haring Bolivar "Recent advances in photonic crystals and metamaterials," International Conference on Telecommunications and Optical Networking, Rome, 3 July 2007.

4. Nigel P. Johnson, **Basudev Lahiri**, Richard M. De La Rue, Dorota A. Pawlak, Sebastian Turczyński, Katarzyna Kołodziejak, "Reflectance measurements of self-organized microstructure of Tb3Sc2Al3O12-TbScO3 eutectic," *Invited paper*, First International Congress on Advanced Electromagnetic Materials in Microwaves and Opticsl Rome, Italy, 22 October 2007.

5. **Basudev Lahiri**, Ali Z. Khokhar, Richard M. De La Rue and Nigel P. Johnson, "Modification of the resonant response of Split Ring Resonators (SRRs) at optical frequencies by the inclusion of nanowires," European Cooperation in the Field of Scientific and Technical Research (COST) P11, Warsaw, 8 May 2007.

6. **Basudev Lahiri**, Ali Z. Khokhar, Richard M. De La Rue and Nigel P. Johnson, "Investigation of modifications to the resonant response of Split Ring Resonators (SRRs) at near IR frequencies produced by the inclusion of nanowires," Metamorphose-EU conference, Belfast, 11 August 2007.

7. Nigel P. Johnson, **Basudev Lahiri**, Ali Z. Khokhar, Richard M. De La Rue and Scott G. McMeekin, "Optical Properties of Split Ring Resonator Metamaterial Structures on Semiconductor Substrates," Proc. of SPIE Vol. 6987, 69871F-1, Strasbourg, 7April 2008.

8. Della Villa, F. Capollino, **B. Lahiri**, N. P. Johnson, S. Turczynski, D. A. Pawlak, "Electromagnetic bandgap calculations of Tb3Sc2Al3O12-TbScO3 eutectic with rod-like microstructure," NATO Advanced Research Workshop Metamaterials for Secure Information and Communication, Marrakesh, Marocco, 7 May 2008.

9. **Basudev Lahiri,** Ali Z. Khokhar, Scott G. McMeekin, Richard M. De La Rue and Nigel P. Johnson, "Effect of metals on the response of Split Ring Resonators (SRRs) on semiconductor substrates at NIR frequencies," International conference on optoelectronics and photonics, IIT Delhi, 12 Dec 2008.

10. **Basudev Lahiri**, Ali Z. Khokhar, Richard M. De La Rue, Scott G. McMeekin and Nigel P. Johnson, "Asymmetric split ring resonators for optical sensing," SPIE Europe Optics and Optoelectronics, Prague, 14 April 2009.

11. Nigel P. Johnson, **Basudev Lahiri**, Ali Z. Khokhar, Richard M. De La Rue, and Scott G. McMeekin, "Asymmetric split ring resonators for Infra Red optical sensing of organic materials," The third international congress on advanced electromagnetic materials in microwaves and optics, Metamaterials, London, 30 Aug 2009.

12. **B. Lahiri**, R. Dylewicz, S.G. McMeekin, R. M. De La Rue and N. P. Johnson, "The effect of titanium adhesion layers on the optical resonance of split ring resonators," 2nd International conference on Metamaterials, Photonic crystals and Plasmonics, Cairo, Egypt, 22 Feb 2010.

# Acknowledgement

This work would not have been possible without the active support, encouragement and care from my supervisors Dr. Nigel P. Johnson and Prof. Richard M. De la Rue. Dr. Johnson has been my mentor throughout these years, supporting me academically, financially and above all motivationally. He has always believed in me and has encouraged me to take on new challenges and endeavours. Dr. Johnson is the supervisor that every aspiring PhD student dreams to have. It's his guidance and support that I refer to whenever in need. Prof. De La Rue is perhaps the most brilliant man I have met in my life. His knowledge and wisdom in a variety of matters surpasses everything I have encountered so far. Every meeting with him has been a source of inspiration and admiration. I am grateful to both of them from the bottom of my heart for considering me as a PhD student under their supervision. It has been an absolute honour and privilege to work under their guidance.

I would like to thank Dr. Harold M. H. Chong to guide me through the process of nanofabrication at the early stages of my career. It's his teachings and hands on approach that has enabled me to take on severe nanofabrication challenges. My sincere gratitude to my senior Dr. Ali Z. Khokhar for guiding me throughout my PhD years. My relationship with Ali, from the very beginning has transcended the academic boundaries and has become a very personal one. In every respect, Ali has been the elder brother that I never had.

I would like to thank Dr. Scott G. McMeekin and Dr. Rafal Dylewicz for carrying out the simulation work in this thesis. I thank Dr. Huabing Yin for carrying out the processes for immobilizing the DNA strands onto the A-SRR and gold samples. I thank all of them for the fruitful discussions and analysis of results.

My deepest gratitude towards the staff, members and technicians of the James Watt Nanofabrication Centre (JWNC) to let me use their facilities as well as provide me with invaluable suggestions for further improvements. I am grateful to Dr. Mike Jarvis of the chemistry department to allow me to use their FTIR machine.

Special thanks to the European Commission through the Metamorphose NoE, ECONAM and COST action MP0702 for support towards the financial aspects of this project.

No words can justify the immense support and encouragement that I have received from my parents in pursuing this endeavour. It's the sheer determination; support and love of my mother that has placed me where I am today. My father has been my oldest and best teacher. It's his teachings and encouragements from a very early age that has driven me to pursue this path of academic research. And finally to myself, what else can I say except *"It is the cause, it is the cause, my soul--. Let me not name it to you, you chaste stars!--. It is the cause*."

*"To my parents, to my supervisors, to the University. To Glasgow and to Scotland. The country whose warmth, hospitality and generosity I will cherish forever.*
*And to India, my much-loved motherland, the ancient, the eternal and the ever-new."*

# *Mind without fear*

*"Where the mind is without fear and the head is held high;*

*Where knowledge is free;*

*Where the world has not been broken up*

*into fragments by narrow domestic walls;*

*Where words come out from the depth of truth;*

*Where tireless striving stretches its arms towards perfection;*

*Where the clear stream of reason has not lost its way into the dreary desert sand of dead habit;*

*Where the mind is led forward by thee into ever-widening thought and action---*

*Into that heaven of freedom, my Father, let my country awake."*

***Rabindranath Tagore** (7 May 1861 – 7 August 1941)*

# Table of Contents

# Description of the SEM images at the beginning of each chapter

1. SEM image at page 15- Silver globule of diameter ~ 30 µm deposited on gold based lollypop electrode surface using a potentiostat.

2. SEM image at page 41- Gold based SRRs of size (length) ~ 500 nm fabricated over silicon substrate.

3. SEM image at page 63- Gold based SRRs of size (length) ~ 400 nm fabricated over silicon substrate.

4. SEM image at page 85- Gold based A-SRRs of diameter ~ 1.2 µm fabricated in a quasi-periodic arrangement on silica substrate.

5. SEM image at page 109- PMMA blocks localised near the centre of the left-hand arc of A-SRRs of diameter ~ 1.55 µm.

6. SEM image at page 132- Silver infiltration onto 3-D photonic crystals of polystyrene spheres of diameter ~ 230 µm using a potentiostat.

7. SEM image at page 154- Double A-SRRs (DA-SRRs) of outer diameter ~ 2 µm fabricated over silica substrate.

## Outline of the thesis

This thesis is divided into two parts. Part I contain the chapters from 1 to 3 and discuss the response of Split Ring Resonators (SRRs) and their characteristic dependence on various external factors such as choice of metals and substrates.

Part II, which contain the chapters 4 to 6 deals with Asymmetric Split Ring Resonators (A-SRRs) and their application in optical bio-sensing of organic compounds and bio-molecules.

Chapter 1 gives the very basic definitions of refraction, refractive index and negative refractive index. It provides the definition of metamaterials and describes the Split ring Resonators (SRRs) as the basic units of metamaterials.

Chapter 2 gives a comprehensive report on the dependence of the resonances of SRRs on the choice of metallization and substrates. This chapters describes how, by using different metals e.g. aluminium and gold, a shift is obtained in the resonance position of similar sized SRRs and goes on further to utilise this property to produce the LC resonance in the visible part of the spectrum for the very first time.

Chapter 3 deals with the effect of adhesion layers on the overall resonances of gold based SRRs at optical frequencies. In order to stick gold on dielectric substrates, an adhesive layer is required. Usually, the effect of this adhesive layer is ignored in determining the

overall resonance of gold based SRRs. In this chapter the effect of titanium adhesion layer over gold is studied and quantified.

Chapter 4 describes the Asymmetric split ring resonators (A-SRRs). In this chapter it is shown that by adding asymmetry to the overall geometry of the split ring resonators, it is possible to increase their quality factor by a factor of two or more.

Chapter 5 utilises this high quality factor of A-SRRs for detection of very thin layers (~100 nm) of organic compounds e.g. PMMA. It is also shown in this chapter that by localising the organic compounds near the electromagnetic hot-spots of the A-SRRs, a much enhanced detection of the organic compound is possible.

Chapter 6 describes the uses of A-SRRs in detecting and differentiating between different DNA base pairs of adenine and thymine.

Chapter 7 discusses all those experiments that are still in progress and suggests on the future works. It provides a brief summary of the entire thesis and makes the overall conclusion.

# Chapter 1

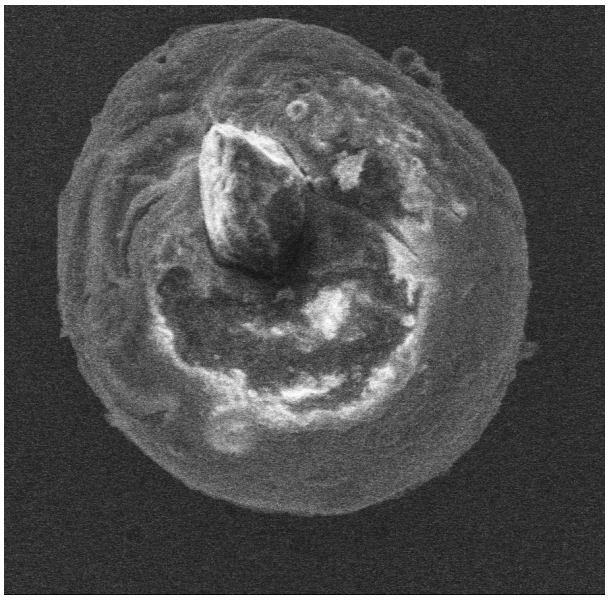

# Introduction: Metamaterials and Split Ring Resonators (SRRs)

The scanning electron microscope images given at the beginning of each chapter have very little relevance to the material inside. The primary purpose of placing these images is to interest the reader and break the monotony from reading this serious thesis. For a description of all these images, please refer to the page 12.

During recent years, Metamaterials have generated a tremendous amount of research interest due to their extraordinary response to electromagnetic waves. In fact, Science magazine named it as one of the “top ten scientific breakthroughs” of 2003. At present, metamaterials are among some of the rapidly emerging fields of scientific research. In this chapter, the basic definition of a metamaterial is described. A very brief introduction is given to refraction, refractive index and Snell’s law. Finally the operation of a split ring resonator (SRR) as a unit of a metamaterial is described, along with the fabrication and measurement techniques used throughout this thesis.

## 1.1 Introduction

Metamaterials are artificially created or engineered materials that typically have periodically arranged features of dimensions smaller than that of the wavelength of light. They demonstrate electromagnetic properties quite different from those of naturally occurring materials. Metamaterials derive their properties from a combination of composition and structure, rather than from their composition alone.

Metamaterials exhibit electromagnetic responses not readily available in naturally occurring materials and structures - such as negative refractive index [1], artificial magnetism [2], super focusing [3], electromagnetic invisibility (cloaking) [4]. They typically contain fabricated micro or nano structures (often made of metals) smaller than the wavelength of radiation in the region of interest, which is the guiding factor behind their unusual response to electromagnetic waves. The on-line encyclopedia of Wikipedia provides a huge list of potential applications of metamaterials - including sensor detection, infrastructure monitoring, battlefield communication and public safety. In later chapters of this thesis the properties of metamaterials are harnessed for accurate detection of very small amounts of organic and biochemical substances.

The engineered structures of metamaterials replace the atoms and molecules that determine the overall electromagnetic response of a conventional material [2, 4-5]. Because of the smallness of the structuring in comparison with the wavelength of the light, the incident electromagnetic radiation encounters a nearly homogeneous material during wave-material interaction. The electrons oscillating in highly conductive metals,

such as gold (Au), aluminium (Al), silver (Ag), copper (Cu), give rise to the specific electromagnetic response of the metamaterial, in conjunction with the geometries of the metallic features. By adjusting the geometries of the metallic micro/nano structural units, customised electromagnetic responses can be obtained [4-5]. Split-ring resonators (SRR) are arguably the most common metamaterial micro/nano structural unit - and are utilised for their resonant response and negative magnetic properties [4]. The SRRs can be fabricated over a wide range of dimensions to suit a large portion of the electromagnetic spectrum ranging from radio and microwave frequencies (wavelength 100 km to 1 cm) to the infrared and optical frequency range (wavelengths in the range 10 μm to 400 nm).

## 1.2 Refraction

Refraction is a fundamental characteristic of electromagnetism. Whenever an electromagnetic wave travels from one medium to another, a change in the phase velocity of propagation takes place that gives rise to a change in the direction of the travelling wave. This phenomenon is called refraction. The velocity of an electromagnetic wave travelling through a medium depends on the optical density of that medium. The optical density of a material (medium) is different from its physical density, which is the ratio of its mass to volume. The optical density of a material is the tendency of the component atoms and molecules to store and propagate electromagnetic waves through them. The more optically dense a material is, the slower will be the velocity of wave propagation through it. The direction of the travelling wave inside a material thus depends on whether the wave is travelling from a denser (slow) medium to a rarer (fast) medium or from a

rarer medium to a denser medium - and what is its initial direction is. A characteristic indicator of the optical density of a material (medium) is its refractive index (RI) [6-7].

## 1.3 Refractive Index

Every material possesses a refractive index that is almost universally denoted by **"*n*".** The refractive index (RI) of a material is the ratio between the phase velocity of the electromagnetic wave travelling in a reference medium (usually vacuum, where the speed of light is maximum) and the phase velocity of the wave travelling through that particular material. The speed $(c)$ of an electromagnetic wave in general is given by the product of its wavelength $(\lambda)$ and frequency *(f),*

$$\text{i.e. } c = \lambda \times f \qquad (1.1)$$

Whenever the speed of an electromagnetic wave changes through changes in the medium, the wavelength changes, but the frequency of the wave remains constant. Every time an electromagnetic wave travels from a rarer medium (e.g. vacuum) with a velocity *c* into a denser medium, its velocity changes (decreases) to *v*. So the RI of that material is given by.

$$n = c / v \qquad (1.2)$$

Hence, the RI *(n)* of vacuum has a numerical value of *1*.

The direction of the propagation of the electromagnetic wave obeys Snell's law.

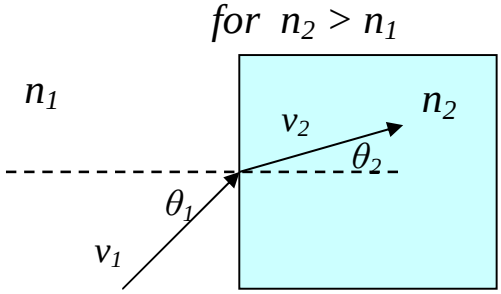


**Figure 1.1:** Refraction of a wave while traveling from one medium to another.

In Fig 1.1 an electromagnetic wave travels from a rarer medium of refractive index $n_1$ at a velocity $v_1$ to that of a denser medium of refractive index $n_2$ - and its velocity reduces to $v_2$. *So,* $n_2 > n_1$ and hence**,** $v_1 > v_2$**.** The incident ray travels with an angle $\theta_1$ (angle of incidence) in the rarer medium $n_1$, with respect to the dotted line that is taken as a reference and is the normal to the interface. The wave undergoes refraction inside the denser medium $n_2$ and travels at an angle $\theta_2$ (angle of refraction) with respect to the normal [6-7].

Snell's law states that the ratio of the *sines* of the angles of incidence and refraction is equal to the ratio of velocities in the two media.

So $$v_1 / v_2 = \sin\theta_1 / \sin\theta_2 \qquad (1.3)$$

*Now since,* $$v_1 / v_2 = n_2 / n_1 \qquad \textit{(from 1.2)} \qquad (1.4)$$

*So* $$n_2 / n_1 = \sin\theta_1 / \sin\theta_2 \textit{ or } n_1 \sin\theta_1 = n_2 \sin\theta_2 \qquad (1.5)$$

It can therefore be concluded that, when light travels from a rarer medium to a denser medium, it bends towards the normal. The exact opposite of this is observed when light travels from a denser to a rarer medium [6-7].

The RI of a material depends on its response to the electric and magnetic components of an electromagnetic wave. The response of a material to the optical electric field is determined by its electric permittivity $(\varepsilon)$

$$\text{Where, } \varepsilon = \varepsilon_r \varepsilon_0 \qquad (1.6)$$

$\varepsilon_r$ is the dielectric constant of that material (relative permittivity) and $\varepsilon_o$ is the permittivity of free space. The permittivity of a material is its degree of response to an electric field, how much the material is polarised with respect to the field and how much it can allow the field to pass through it.

The response to the optical magnetic field is determined by the magnetic permeability $(\mu)$.

$$\text{Where, } \mu = \mu_r \mu_0 \qquad (1.7)$$

$\mu_r$ is the relative permeability of the material and is mostly assumed to be 1 [6] and $\mu_0$ is the permeability of free space. Permeability is the exact magnetic counterpart of permittivity. It depicts the degree of response of the material to a magnetic field.

In an isotropic medium the refractive index (n) is given as [6]

$$n = (\varepsilon_r \mu_r)^{\frac{1}{2}} \qquad (1.8)$$

However, at higher frequencies, the refractive index of the material almost totally depends on its electric permittivity ($\varepsilon$). This dependence is mainly because the magnetic field component of the light typically couples to atoms very weakly, as compared to the electric component - and hence the response of the material depends almost entirely on its permittivity. This is the reason why many naturally occurring magnetic responses are limited to lower frequencies [5].

## 1.4 Negative Refractive Index

However, $\boldsymbol{\varepsilon_r}$ and $\boldsymbol{\mu_r}$ are complex quantities that are written as:

$$\varepsilon_r = \varepsilon_1 + i\varepsilon_2 \tag{1.9}$$

$$\mu_r = \mu_1 + i\mu_2 \tag{1.10}$$

This makes the refractive index (n) complex - and it can be written as:

$$n = n' + in'' \tag{1.11}$$

Where the imaginary part $n''$ characterizes light extinction (losses) and the real part $n'$ gives the factor by which the phase velocity of light is decreased inside the medium.

In 1968 *Victor Veselago* showed that if $\varepsilon_r$ and $\mu_r$ (real parts at least) are negative, Maxwell's equations imply a negative square root for the refractive index [1]. The phase velocity of light in such a material will be directed opposite to the flow of energy [5].

A possible approach [from reference 5] to achieving such a condition in a passive medium is by engineering a material where the (isotropic) permittivity $\varepsilon = \varepsilon_1 + \imath\varepsilon_2$ - and the (isotropic) permeability $\mu = \mu_1 + \imath\mu_2$ obeys the equation,

$$\varepsilon_1|\mu| + \mu_1|\varepsilon| < 0 \qquad (1.12)$$

This leads to a negative real part of the refractive index and

$$n = n' + \imath n'' = -\sqrt{\varepsilon_r \mu_r} \qquad (1.13)$$

The above condition is satisfied when $\varepsilon_1 \langle 0 \; and \; \mu_1 \langle 0$. However this is not a very strict condition and a material could possess a negative refractive index by having only one real component that is negative [5]. A measure of the strength of the negative behaviour for n in such a material is given by the figure of merit (FOM) $= \frac{n'}{n''}$

Interesting consequences can arise for such a material with negative refractive index. It has been shown that, in such a material, many electromagnetic phenomena act in exactly the opposite way to conventional materials. When light enters such a material from the outside, it makes a sharp turn, unlike the situation for normal refraction. The Snell's law of $n_1 \sin\theta_1 = n_2 \sin\theta_2$ still holds, but since $n_2$ is negative, the refracted ray will remain in the same half-plane (bounded by the normal to the interface) as the incident ray. Similarly other electromagnetic phenomena such as the Doppler effect and Cherenkov radiation would exhibit exactly opposite behaviour to that occurring traditionally [1-5].

The refraction of light in such a material is illustrated below

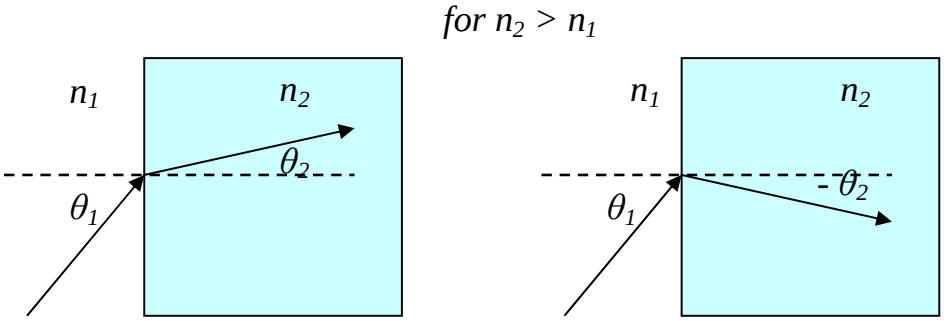


(a) Refraction in a material with positive refractive index

(b) Refraction in a material with negative refractive index

**Figure 1.2:** Phenomenon of Refraction in (a) positive refractive index material and in a (b) negative refractive index material.

Thus, these materials can bend the light in the "wrong way". It has been found that many naturally occurring metals such as gold (Au), silver (Ag), aluminium (Al) etc can show negative permittivity at optical frequencies. However, as discussed earlier, naturally occurring materials have poor response to permeability at optical frequencies and in most cases they are close to 1. So, the refractive index of materials at optical frequency depends mainly on their permittivity [2-5].

## 1.5 The Split Ring Resonator (SRR)

In 1999, it was proposed by Pendry *et. al*. [2] that by creating artificial structures of dimensions smaller than the wavelength of light in a periodic manner can give rise to negative refractive index. These materials were subsequently named as "*metamaterials*" or "*Left handed materials (LHM*)". Pendry proposed that an array of homogeneously

spaced sub-wavelength Split Ring Resonators (SRRs) as metal hoops, which as a whole behave like a composite material. These SRRs can act as an LC oscillating circuit containing a magnetic coil of inductance L and capacitor of capacitance C. In their fundamental resonance, they behave as an LC oscillatory circuit that contains a single turn magnetic coil of inductance - in series with a capacitance produced by the gap between the arms of the SRR. The SRR and its equivalent circuit are illustrated in Figure 1.3.

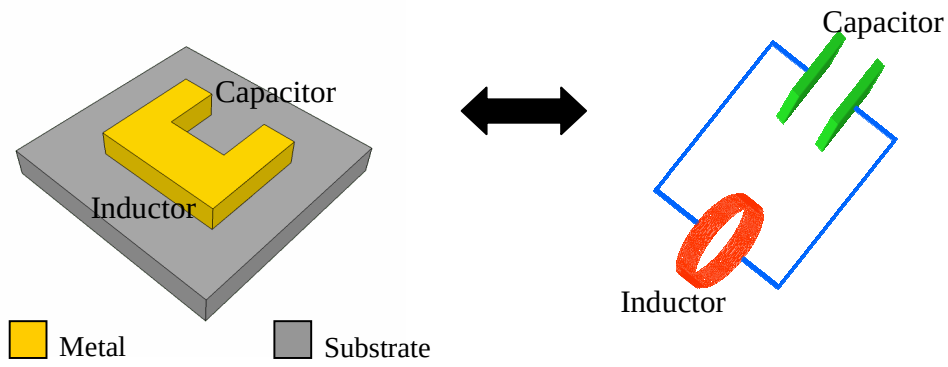


(a) Split ring resonator (SRR) (b) Equivalent circuit

**Figure 1.3:** A single unit cell of the SRR array and its Equivalent LC Circuit. The gap of the SRR acts like a parallel plate capacitor, whilst its base acts as an inductor.

The unit cell of a SRR and its two different polarisation dependent electromagnetic responses are shown in Figure 1.4. For normal incidence with TE polarization mode, when the incident electric field is across the gap (parallel to the X axis), the electric field couples with the capacitance of the SRR and generates a circulating current around it. This circulating current induces a magnetic field in the base of the SRR and also interacts with the external field to generate the magnetic resonance that can be appropriately called

as an LC resonance as identified by Linden et al. [3]. When the incident light is with TM polarisation mode, with the electric field perpendicular to the gap (parallel to Y axis) the electric field cannot couple to the capacitance of the SRR and therefore generates only electric (plasmon) resonances [2-4].

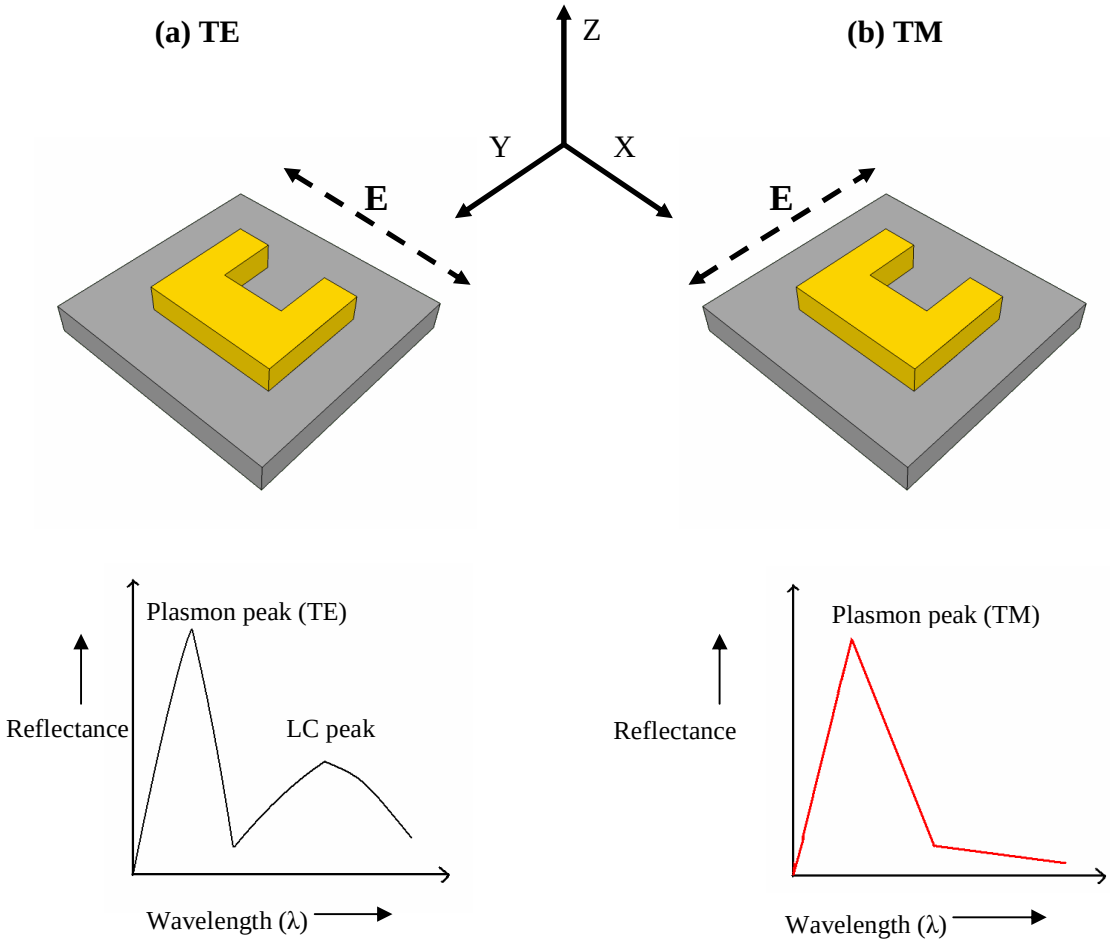


**Figure 1.4:** Schematic of single SRR and their corresponding reflectance spectra (Illustration Only) with (a) TE measurements of normal to surface incidence having the Electric field (dashed line) parallel to the SRR arms (parallel to the X-axis) and (b) TM measurements of normal to surface incidence having the Electric field perpendicular to the SRR arms (parallel to Y-axis).

It should be noted here that there exists a difference in the spectral position as well as the width of the plasmon peaks obtained from two different polarisation configurations. This is explained by Enkrich *et.al* [8] for TE polarisation only the base of the SRR is excited and produces the TE plasmon peak. For TM polarisation, both the arms of the SRR are excited which are coupled via its base. As a result there is a formation of two new symmetric and asymmetric oscillation modes. The asymmetric mode cannot be excited for symmetric SRRs (see chapter 4 for more details on the asymmetric modes), but the symmetric mode gets excited and is slightly red shifted as compared to the uncoupled plasmon resonance of the base in TE measurements. The plasmon resonance of the TM mode hence, has a larger effective electric dipole moment [8].

At the same time, negative permittivity can be achieved by placing a periodic array of thin metallic wires in close proximity. The wires individually act as electric dipoles and their overall response can give rise to negative permittivity. Combining wires with SRRs can give rise to negative refractive index. In 2001 Smith *et al.* [9] created interlocking units of fibre-glass sheets imprinted with copper rings and wires. This structure experimentally confirmed negative refractive index in microwave region and bent the incident wave the “wrong way” [9] when emerging from the metamaterial.

## 1.6 The magnetic response (LC response) of a SRR

As described previously, the SRR acts as a LC circuit and its magnetic response (LC resonance) is due to the circulation of electric current when the electric field of the normally incident wave is parallel to its gap. Hence, the LC resonance is polarisation dependent. A single SRR is shown in Figure 1.5 once again with its dimensions that are used to derive the formula for its magnetic resonance (LC resonance).

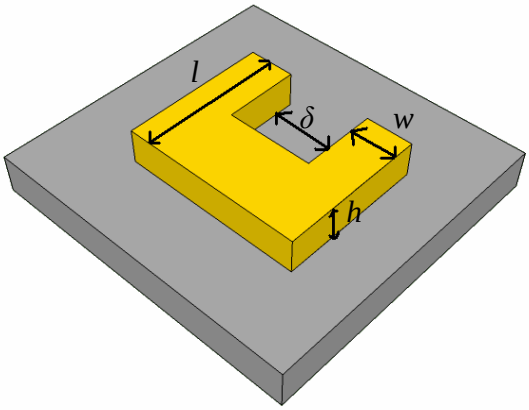


**Figure 1.5:** A single unit cell of the SRR array, with *l* being the overall length, *w* is the width of arm, *h* the thickness (height) of SRR - and *δ* the gap between arms.

From basic textbook formula of capacitance of a parallel plate capacitor with standard approximations as given in reference [10] the capacitance (C) of a SRR is calculated as

$$C\alpha \frac{Area\ of\ the\ plate}{Dis\tan ce\ between\ the\ plates} \qquad (1.14)$$

$$or\ C = \varepsilon_0 \varepsilon_c \frac{wh}{\delta} \qquad (1.15)$$

Where, $\varepsilon_c$ is the dielectric constant of the substrate.

Similarly, the inductance ($L$) of a coil of N turns, where N=1 is given as [10]

$$L\alpha\frac{Area\ of\ coil}{Length} \tag{1.16}$$

$$or\ L=\mu_0\frac{l^2}{h} \tag{1.17}$$

Now, the resonance frequency ( $\omega_{LC}$ ) of an LC circuit is given by [10]

$$\omega_{LC}=\frac{1}{\sqrt{LC}} \tag{1.18}$$

Putting the values of C and L from equations 1.15 and 1.17 into equation 1.18 we get the LC resonance frequency ( $\omega_{LC}$ ) as [10]

$$\omega_{LC}=\frac{1}{l}\sqrt{\frac{\delta}{w}}\frac{c_0}{\sqrt{\varepsilon_c}} \tag{1.19}$$

The LC resonance wavelength ($\lambda_{LC}$) is given as [9]

$$\lambda_{LC}=\frac{2\pi c_0}{\omega_{LC}}=2\pi l\sqrt{\varepsilon_c}\sqrt{\frac{w}{\delta}}\ \alpha\ size \tag{1.20}$$

Thus, from equation (1.20) it could be said that the LC resonance wavelength ($\lambda_{LC}$) is proportional to the size of the SRR.

From equation (1.20) it is seen that the gap between arms ($\delta$) is very important since if the gap of the SRR is closed i.e. $\delta$ = 0 the LC resonance frequency ( $\omega_{LC}$ ) becomes zero and the LC resonance wavelength ($\lambda_{LC}$) becomes infinite [10]. Also from equation (1.20)

the thickness/height (*h*) of the SRR plays no significant role in the determination of its LC resonance frequency.

Thus, it is seen that the response of a SRR is dependent only on its size i.e. dimensions and not on metal properties (and is constant for a given substrate ($\varepsilon_c$) for the surrounding substrate permittivity). As a result there was a sustained effort in the scientific community to scale the sizes of SRRs to smaller (nano scale) levels to push the LC resonance at higher frequencies. It was considered novel as, there were no such magnetic materials exhibiting magnetic resonances at such high frequencies. At low frequency regimes, up to several Terahertz, the magnetic resonance (LC resonance) scales reciprocally with dimensions of SRRs. However, at higher frequencies, this scaling law is no longer valid and the response of a SRR no longer depends on its size. It was explained that at higher frequencies (optical and near infrared regimes) the kinetic energy of the electrons in the metal becomes predominant and this in turn kills the circulating electric current produced by the coupling of the SRR arms, in turn destroying its LC response [11-12]. This phenomenon along with some other novel responses of the SRR is discussed in detail in the subsequent chapters.

## 1.7 Fabrication of SRR structures

In each of the following chapters the nano-fabrication aspects pertaining to that particular topic are discussed in detail. However, in this section a description of the fabrication of nano-scale SRRs is provided to give the reader a general idea of the steps required. The pattern to be written over a semiconductor substrate (e.g. silicon) is first designed in CAD

software, Tanner L-Edit$^{TM}$. The design is then converted to GDS file which is readable by an Electron beam (E-beam) lithography machine. The sample is then prepared as follows.

1) The Silicon wafer of around 2 cm X 1cm is rinsed with acetone in an ultrasonic bath for ~ 55 sec then Methanol in the same way for ~ 55 sec and then in the same way with Isopropyl- Alcohol (99%) (IPA) for ~ 55 sec.
2) An e-beam positive resist 4% 2010 PMMA is then spun over the sample at 5000 rpm for 60 seconds to give a thickness of 110 nm.
3) The sample is then put into an $180^0$C oven for 15 minutes.
4) The sample is then spun with 4% 2041 PMMA at 5000 rpm for 60 seconds to give an additional thickness of 126 nm. The sample is then baked in the $180^0$ C oven for 1 hour so that the resist can better adhere to the wafer.
5) The sample is then submitted for E-beam lithography. The dose is varied from ~ 800 $\mu C/cm^2$ – 5200 $\mu C/cm^2$ for 100 KV beam depending on the feature size required.
6) The resolution is selected from 1.25 nm to 0.50 nm.
7) The written sample is then developed with 2:1 MIPBK at $23^0$C for 45 seconds, and cleaned with IPA.
8) The sample is then given for metal deposition. Typical examples of deposition are 2 nm Ti + 48 nm Au or 50 nm Al.
9) Excess metal and resist is then lifted off using warm acetone.

To summarize: the pattern is designed and then patterned by Electron beam lithography. The Structure is formed during metal lift-off. The patterns are written over an area of ~ 300 μm X 300 μm. The entire steps 1 to 9 are illustrated in the following Figure 1.6.

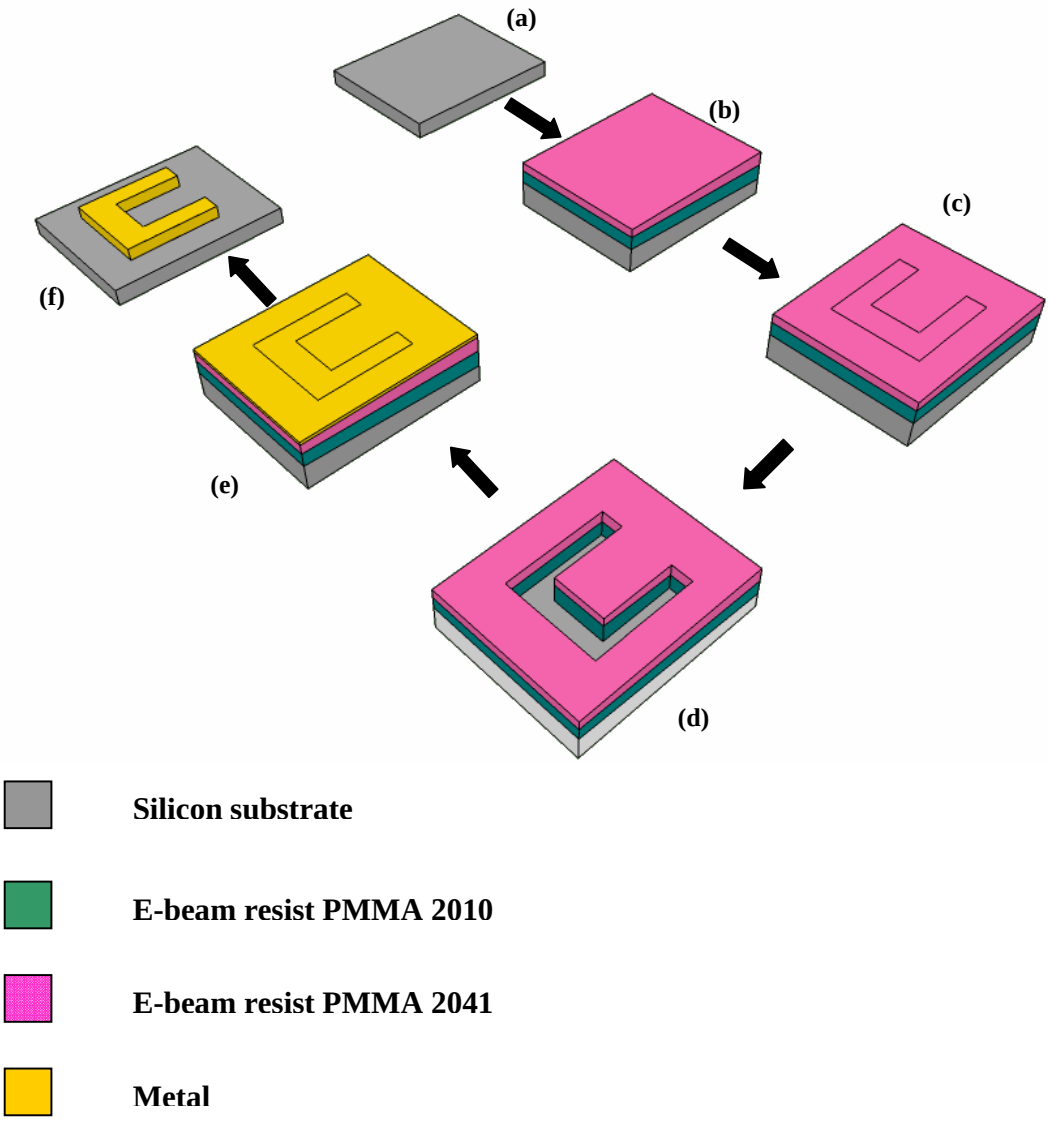


**Figure 1.6:** Fabrication processes of SRR structures (a) cleaning of silicon substrate; (b) spinning of E-beam resist; (c) E-beam exposure; (d) development; (e) Metal deposition; (f) Lift-off in warm acetone.

The Scanning electron microscope (SEM) image of SRRs fabricated using the above process is shown below.

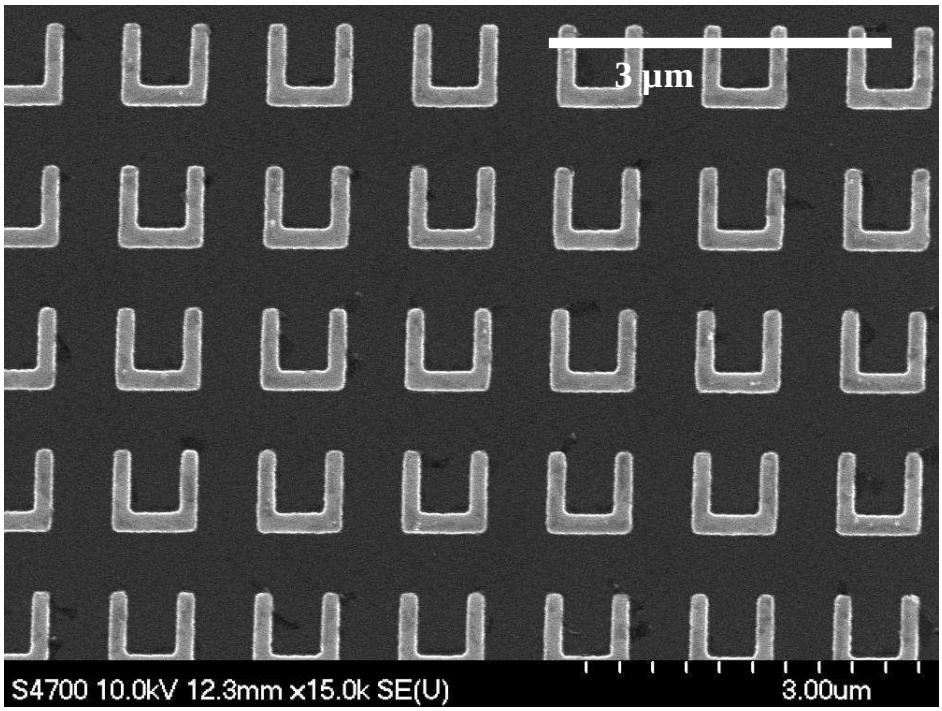


**Figure 1.7:** SEM image of gold SRRs fabricated on a silicon substrate.

## 1.8 Reflectance measurements

The reflectance measurements were always performed at normal incidence with an optical microscope, using a X10 lens with an NA of 0.25, a white light source - and a spectrometer (that also polarizes the white light) with either an InGaAs detector (for operating range: 0.8 µm – 1.6 µm) or a SiGe detector (for operating range 0.4 µm to 0.8 µm) and lock-in amplifier. The polarization control in this case was obtained by rotating the samples by $90^0$ to obtain two different sets of polarization dependent data. Figure 1.8 shows such a measurement setup for the operating range of 0.4 µm to 1.6 µm.

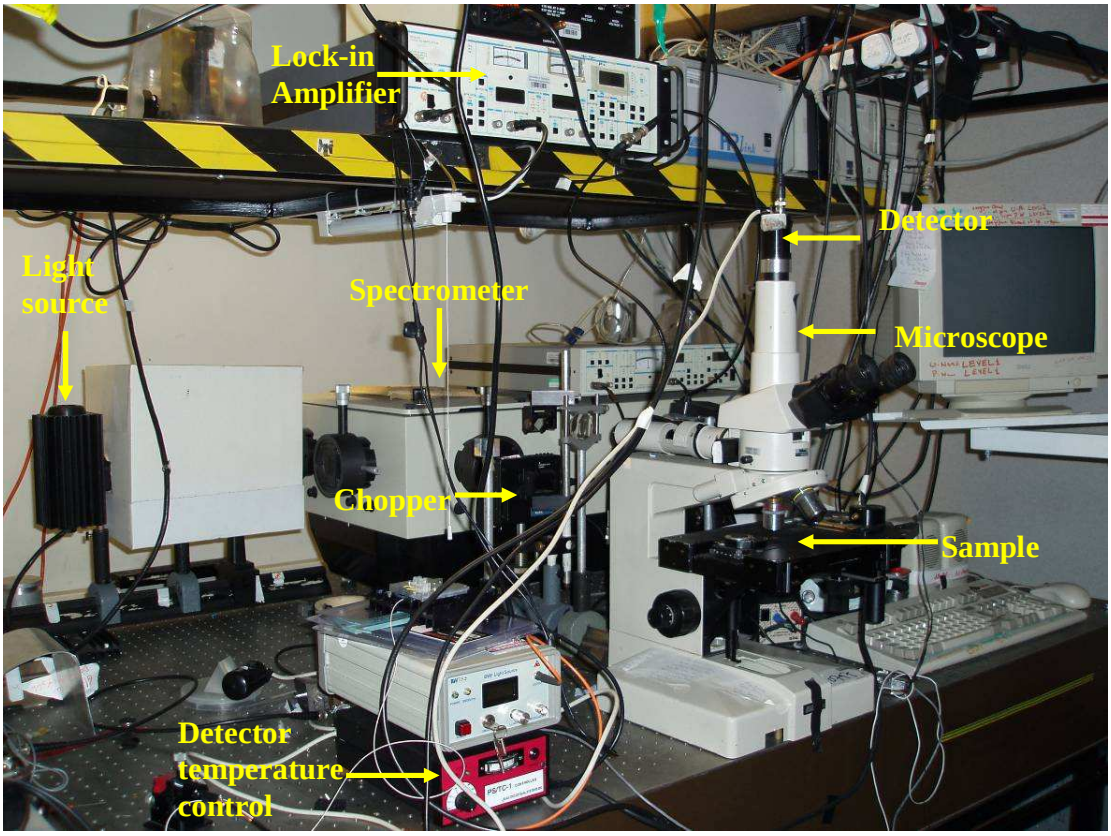


**Figure 1.8:** Reflectance measurement setup for the operating range of 0.4 µm to 1.6 µm.

For the measurements at longer wavelengths (in the range from 1 µm to 3 µm), measurements were taken at normal incidence with a BioRad FTS 60 FTIR spectrometer equipped with a Cassegrain microscope. The FTIR beam was polarized using a KRS5 polarizer adapted to the appropriate wavelength region. A diaphragm was used to restrict the entire incident light beam onto a spot size ~ 250 µm X 250 µm in area. For reflectance measurements at even longer wavelengths (in the range from 2.5 µm to 15 µm), a Nicolet Continuum 6700 FTIR spectrometer equipped with an IR microscope was used. A nitrogen-cooled mercury-cadmium-telluride (CMT) detector was used in

these measurements. This FTIR beam was polarized using a Continuum ZnSe IR polarizer.

**Figure 1.9:** Nicolet Continuμm 6700 FTIR fitted with a IR microscope.

All measurements were performed at normal incidence. The reflectance measurements were taken for two orthogonal linear polarizations of incident light oriented simultaneously with respect to the array axes and the SRR element orientation.

Figure 1.10 shows the SEM image of an array of aluminium based SRRs fabricated on a silicon substrate and its corresponding reflectance spectra measured by the above mentioned methods.

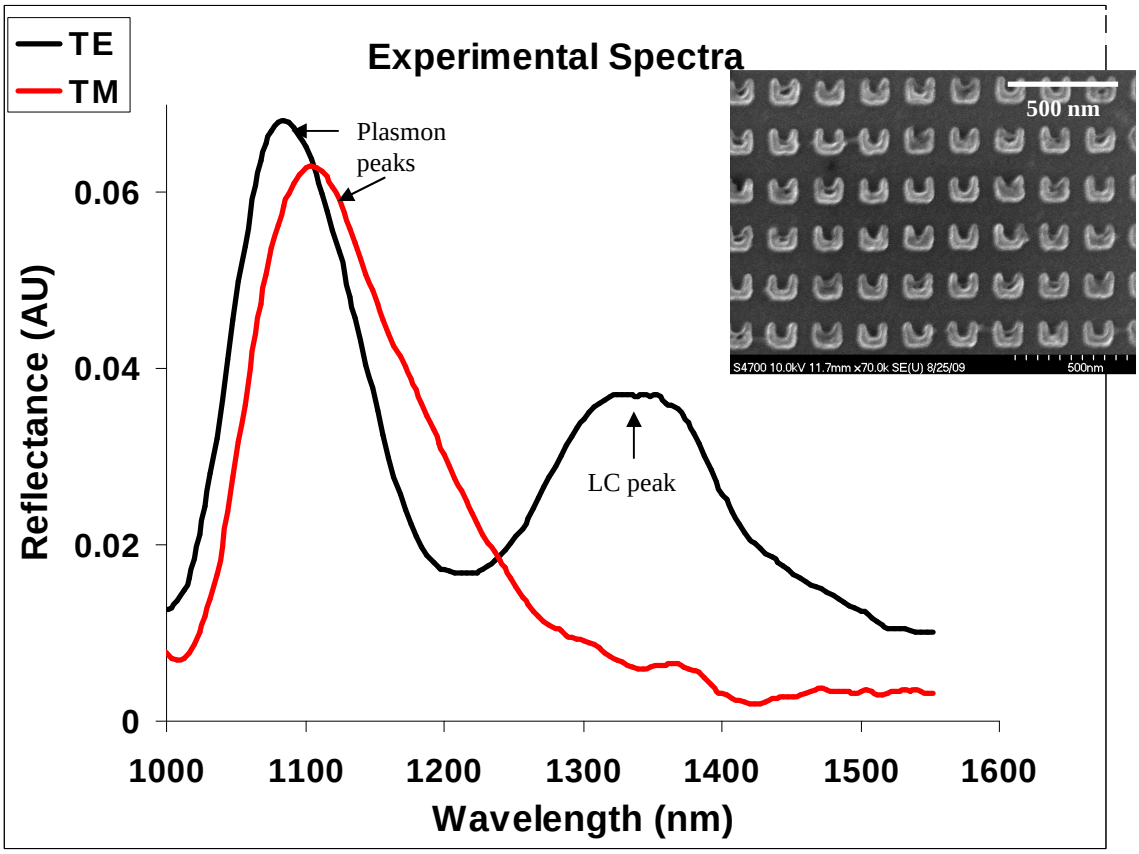


**Figure 1.10:** SEM image (Inset) of aluminium based SRRs fabricated on medium doped silicon substrate and its corresponding normal to plane experimental reflectance spectra. The black curves are for TE polarisation - and the red curves are for TM polarisation measurements. The LC peak for TE polarisation is observed at 1344 nm and the plasmon peaks for TE and TM are observed around ~ 1100 nm.

## 1.9 Extraction of permittivity and permeability of fabricated structures

The method of extraction of permittivity and permeability from transmission and reflection coefficients is a hotly contested topic. In the preliminary analysis an attempt was made to follow the formula suggested by Smith *et al* in reference [13]. The formula states that the real part of the refractive index 'Re (n)' and the imaginary part of the refractive index 'Im (n)' can be given as

$$\text{Re}\,(n) = \pm\,\text{Re}\left(\frac{\cos^{-1}\left(\frac{1}{2t'}\left[1-\left(r^2-t'^2\right)\right]\right)}{kd}\right)+\frac{2\pi m}{kd} \qquad (1.21)$$

$$\text{Im}\,(n) = \pm\,\text{Im}\left(\frac{\cos^{-1}\left(\frac{1}{2t'}\left[1-\left(r^2-t'^2\right)\right]\right)}{kd}\right) \qquad (1.22)$$

Where, r = Reflection coefficient

t' = Normalised transmission coefficient = *exp (ikd)t*

t = Transmission coefficient

k = Wavenumber of incident wave = ω / c

d = Total thickness of the material

m = Integer

However, this formula is since been severely disputed. This formula makes many ambiguous assumptions and is suitable mainly for calculations of refractive indices at microwave frequencies. It also assumes that the dielectric functions of metals are constant at all frequencies. In order to extract the values of permittivity and permeability of SRRs arrays, it is required to have both the transmission and the reflection coefficients at both

normal incidence as well as angular incidence (to generate phase characteristics). To date the experimental set-ups used lacks these features and hence it was not possible to calculate the permittivity and permeability values for the experiments. Hence, based on these shortcomings, it was decided by the author, not to include any experimentally derived permittivity and permeability values in this thesis.

However, it should be mentioned that the lack of permittivity and permeability values from the experiments described in the subsequent chapters has very little effect on the overall outcome of this thesis. This thesis is mostly concerned with exploration the different characteristic resonances of SRRs at optical frequencies and their dependence on various external factors such as choice of metallization and substrates. At the same time this thesis makes an attempt to utilise the different resonances of SRRs for spectral detection of very thin films of organic compounds as well as bio-molecules such as DNA oligonucleotides. The values of the permittivity and permeability play no significant role in the detection of organic compounds.

# References


1. V.G. Veselago, "The electrodynamics of substances with simultaneously negative values of ε and μ," Sov Phys. Usp 10, 509-514 (1968).

2. J.B. Pendry, A.J. Holden, D.J. Robbins and W.J. Stewart, "Magnetism from conductors and enhanced Non-Linear Phenomena," IEEE Trans. Microwave Theory Tech. 47, 2075-2084 (1999).

3. J.B. Pendry, "Negative Refraction Makes a Perfect Lens," Phys. Rev. Lett. 85, 18 3966-3969 (2000).

4. S. Linden, C. Enkrich, M. Wegener, J. Zhou, T. Koschny and C.M. Soukoulis, "Magnetic Response of Metamaterials at 100 THz," Science, 306, 1353-1361 (2004).

5. V.M. Shalaev, "Optical negative index metamaterials," Nature Photonics, 1, 41-48 (2007).

6. John Gowar, *Optical Communication Systems* (Prentice Hall, 2nd Edition 1996) Chapter 3.

7. Gerd Keiser, *Optical Fiber Communications* (McGraw Hill International. 3rd Edition 2000) Chapter 2.

8. C. Enkrich, M. Wegener, S. Linden, S. Burger, L. Zschiedrich, F. Schmidt, J. Zhou, T. Koschny and C. M. Soukoulis, "Magnetic Metamaterials at Telecommunication and Visible Frequencies," Phys. Rev. Lett. 95**,** 203901 1-4 (2005)

9. D.R. Smith and D. Schuring, J.B. Pendry, “Negative refraction of modulated electromagnetic waves,” Appl Phys Lett. 81, 2713-2715 (2002).

10. S. Linden, C. Enkrich, G. Dolling, M. W. Klein, J. Zhou, T. Koschny, C. M. Soukoulis, S. Burger, F. Schmidt amd M. Wegener, “Photonic Metamaterials: Magnetism at Optical Frequencies,” Journal of selected topics in Quantum Electronics, 12, 6 1097-1103 (2006).

11. J. Zhou T. Koschny, M. Kafesaki, E.N. Economu, J.B. Pendry and C.M. Soukoulis, “Saturation of the magnetic response of split ring resonators at Optical frequencies,” Physics Review Letters, 95, 223902 1-4 (2005).

12. M.W. Klein, C. Enkrich, M. Wegener, C.M. Soukoulis and S. Linden, “Single split ring resonators at optical frequencies: limits of size scaling,” Opt. Letters. 31. 1259-1261 (2006).

13. D.R. Smith, S. Schultz, P. Markos and C.M. Soukoulis, “Determination of effective permittivity and permeability of metamaterials from reflection and transmission coefficients,” Physical. Rev. B. 65, 195104 1-5 (2002).

# Chapter 2

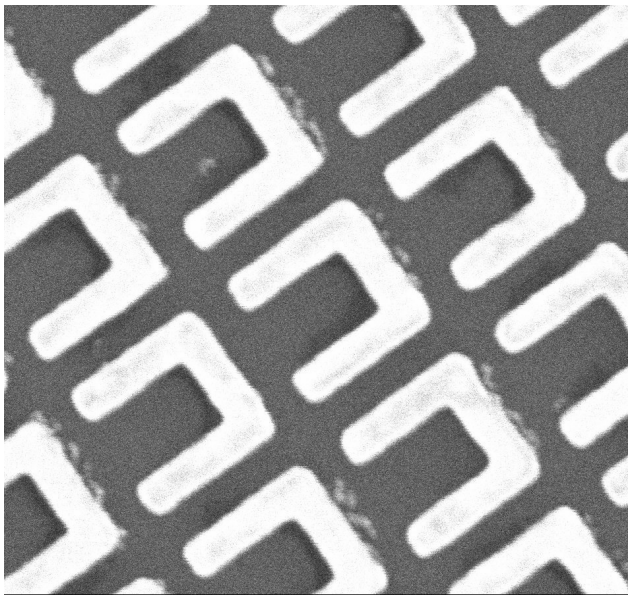

# Magnetic response of split ring resonators (SRRs) at visible frequencies

This chapter investigates the properties and responses of the Split Ring Resonator (SRR) in more detail. A comprehensive comparison between similar sized aluminium and gold based SRRs has been made. At the same time, the effect of two different types of substrate, silicon (active) and silica (passive), on the response of SRRs is studied. Silicon is considered as active substrates for metamaterials, since its properties can be changed by applying an external optical pulse to excite free charge carriers. These free charge carriers can short out the SRR gap, thereby turning off the LC resonance. This process provides a switching mechanism for dynamic control of the resonant response of SRRs. On the other hand, silica is considered as a passive material due to its inertness towards external optical pulses. However, the low refractive index of silica can be used for pushing the resonance response of SRRs at far higher frequencies than their silicon based counterparts. A substantial shift is reported, in the response of arrays of similarly sized SRRs, having a rectangular U-shaped form - and made respectively of aluminium and of gold. A higher frequency limit has been observed in the polarization dependent response (in particular the LC resonance peak) of gold based SRRs in the near infrared region. In this chapter, it is shown that by using aluminium based SRRs instead of gold; the higher frequency limit of the LC resonance can be further shifted into the visible spectrum. This chapter has been partially published in Optics Express Vol. 18, No. 3, 3210-3218 (2010).

## 2.1 Introduction

In the previous chapter, it was observed that metamaterials exhibit electromagnetic effects, such as negative refractive index [1], that are not readily available in naturally occurring materials. They are often fabricated as periodic arrays of metallic microstructures that are individually smaller than the wavelength of radiation in the region of interest. These structures replace the atoms and molecules of conventional materials - and determine the overall electromagnetic response of the material. The oscillation of the electrons in the microstructures of the metamaterial gives rise to specific electromagnetic responses [2]. By adjusting the geometries of the constituent microstructures, a customized electromagnetic response can be obtained. The "U" shaped split-ring resonators (SRR) is arguably the most common element used in forming the basic microstructure of metamaterials. SRRs can be considered, in their fundamental resonance, as behaving like an LC oscillatory circuit that contains a single turn magnetic coil of inductance - in series with a capacitance produced by the gap between the arms of the SRR. For normal incidence with TE polarization mode, when the incident electric field is across the gap, the electric field couples with the capacitance of the SRR and generates a circulating current around it. This circulating current induces a magnetic field in the bottom or horizontal arm of the SRR and also interacts with the external field to generate the magnetic resonance identified as an LC resonance by Linden et al. [3]. When the incident light is TM polarized, the electric field cannot couple to the capacitance of the SRR and therefore generates only electric (plasmon) resonances [2-5]. The LC resonance of the SRR is given as $\omega_{LC} = 1/\sqrt{LC}$ and is inversely proportional to the size (dimension) of SRRs [5].

On the other hand, Rockstuhl *et al*. [6] have examined the various resonances of specifically rectangular U-shaped SRRs and identified all the resonances predicted and observed as plasmonic resonances. A strong test for these conclusions of Rockstuhl and co-workers would be provided by assessing the impact of a major geometrical change such as additional arms (Linden et al [3]) that partially bridge the capacitive gap - thereby increasing the capacitance - while retaining an identical total length for the metallic structure. Similar work has been done by Kante et al [7] where, the SRR gap ($\delta$) is varied by changing the internal angle of the arms from $60^0$ to $180^0$.

In all the cases cited above, the interpretation of the behaviour of the SRRs, formed in arrays, was based primarily on their dimensions - and the detailed properties of the metal were not examined closely. Consequently there has been a considerable effort to scale the sizes of SRRs to nanometer levels - and push the LC resonance to higher frequencies. From low frequencies up to several Terahertz, the magnetic resonance (LC resonance) scales reciprocally with the dimensions of the SRRs. However, at higher frequencies, the resonance of the SRRs no longer shifts to higher frequencies as the SRRs are reduced in size. At these higher frequencies (in the visible and near infrared regimes) the kinetic energy of the electrons in the metal becomes a dominant feature, which in turn limits the circulating electric current produced by the coupling of the SRR arms, in turn limiting its LC response [8-9].

## 2.2 High frequency saturation of the response of metallic SRR structures

It has previously been found that the magnetic response of the "rectangular C" shaped SRR structures typically saturates just before the visible region is reached - and cannot be shifted indefinitely to higher frequencies by reducing the size of the SRRs [8-9]. Tretyakov has studied this phenomenon in the scaling of SRRs and the saturation of the frequency response, using an LC equivalent circuit model [10]. This model considers the dependence of the achievable resonant frequency on the geometric shape of the SRR, as well as arguing for the involvement of an additional kinetic inductance term and an additional distributed capacitance term. In the present chapter, the model of Tretyakov is used in order to help explain some of the results obtained. In order to overcome the saturation behaviour associated with the kinetic inductance, other geometries have been explored, e.g. SRRs in combination with wires [11], nano-strip pairs of wires [12], and nano fishnet structures [13-14]. Yuan et al were able to demonstrate negative permeability at red light wavelengths using pairs of thin silver strips [15].

The "rectangular C" shaped structure studied by Zhou et al. [8] and Tretyakov [10] suffers from extra capacitance, due to the presence of additional pieces at the ends of the arms and giving a reduced SRR gap dimension, thereby decreasing the resonance frequency. By reducing the total capacitance, the "four gap" structure proposed by Zhou et al. [8], '*in principle*', can give a higher resonant frequency, comparable with that achieved later in this chapter. But the "four gap" structure requires extremely small

overall dimensions (~35 nm) and presents a very severe fabrication challenge. Here it is shown that, with suitably reduced arms, “rectangular U” shaped SRRs can give LC resonance at wavelengths down to 530 nm, thus demonstrating the advantage of this geometry. The “rectangular U” shaped SRRs fabricated in this chapter has very similar geometries as described by Linden *et.al.* [16] in which the base of the “U” shaped SRR is increased that in turns reduces the inductance and pushes the resonant response at higher frequencies.

The changes in the properties of metals at higher frequencies, where the metal properties behave according to the Drude model and both the real and the imaginary parts of the dielectric function must be considered, have so far not been fully explored in relation to the high-frequency resonance saturation behaviour of the SRRs [3,8-9]. This chapter investigates the differences that occur in the responses of SRRs with nominally identical dimensions - but made up alternatively of aluminium and gold. Observation of a substantial shift in response between the aluminium and gold SRRs is reported.

Furthermore, this shift is utilised to bypass the resonance saturation behaviour of gold (and, by implication, silver) SRRs - and demonstrate a polarization dependent LC resonance peak at visible wavelengths for the aluminium based SRRs.

The words ‘LC resonance’ are used in this chapter , because this ‘electrical engineering’ concept provides direct understanding of the behaviour and characteristics of the fundamental resonance of SRR structures that have various shapes and packing densities

[3, 17] over the entire frequency spectrum from radio waves to the infra-red regions of the optical spectrum. This terminology is used rather than, 'first plasmon resonance' for the fundamental resonance of the SRRs. The LC nature of the fundamental resonance also has the merit of recognizing the true geometrical shape dependence of the fundamental resonance frequency.

## 2.3 Fabrication and measurement

The SRR patterns were transferred on to either medium-doped silicon or fused silica substrates using electron beam lithography (EBL). A bi-layer of PMMA resist of ~ 100 nm thickness for each layer was spun over the substrates - and, in the case of silica, a thin aluminium charge dissipation layer was deposited on top of the resist. After development the patterns were either subjected to an electron beam deposition process of 2 nm titanium for adhesion and then 48 nm of gold for the gold SRRs, or 50 nm of aluminium was deposited directly for the aluminium samples. The patterns were written as square arrays over an area of about 300 µm x 300 µm. The reflectance measurements were always performed at normal incidence with the setup described in the previous chapter.

## 2.4 Modelling

Dr. Scott McMeekin of Glasgow Caledonian University modeled all the SRR structures described in this chapter. The modeling of the structures was performed using Fullwave, a commercial FDTD simulation package from RSoft. A unit cell was defined with dimensions equal to the spacing of the SRR array and the SRR structure was centered within the cell. The boundary conditions for the cell were set as periodic in the coordinates perpendicular to the propagation direction, effectively extending the array to infinity - and as a perfectly matched layer (PML) in the direction of propagation, to eliminate any reflections from the boundaries. The dimensions of the SRR structure and the array used in the simulation were obtained from SEM measurements of the experimental structures, in order to minimize errors due to fabrication tolerances. The grid size for the FDTD simulation was set at an eighth of the minimum feature size in each direction. The frequency dependent complex dielectric properties of the Al, Au, Si and $SiO_2$ constituent materials were based upon the material parameters defined within the Fullwave software. The Al and Au layers were modeled using a Lorentz-Drude model, the $SiO_2$ substrate was modeled using a Lorentz model and the Si substrate model was based on experimental material parameters measured across the wavelength range of interest [18].

## 2.5 Effect of different choices of metal used in SRRs

One approach for the potential application of SRRs in optical switching and tunability is to fabricate them on active substrates such as medium-doped silicon, the properties of which can be changed by external means [19-20]. Figure 2.1 shows various, nominally similar, SRRs made of gold and aluminium, fabricated on silicon substrates - and their corresponding reflectance spectra.

It can be seen from Figure 2.1 that the experimental results are in moderate agreement with the simulated spectra. The discrepancy between the two sets of results could be attributed to the imperfect SRR shapes fabricated and measured in experimental results as compared to the perfect SRR shapes simulated in modelling. At the same time the experimental results are based on an array structure, whereas the modelling is performed on only one SRR structure.

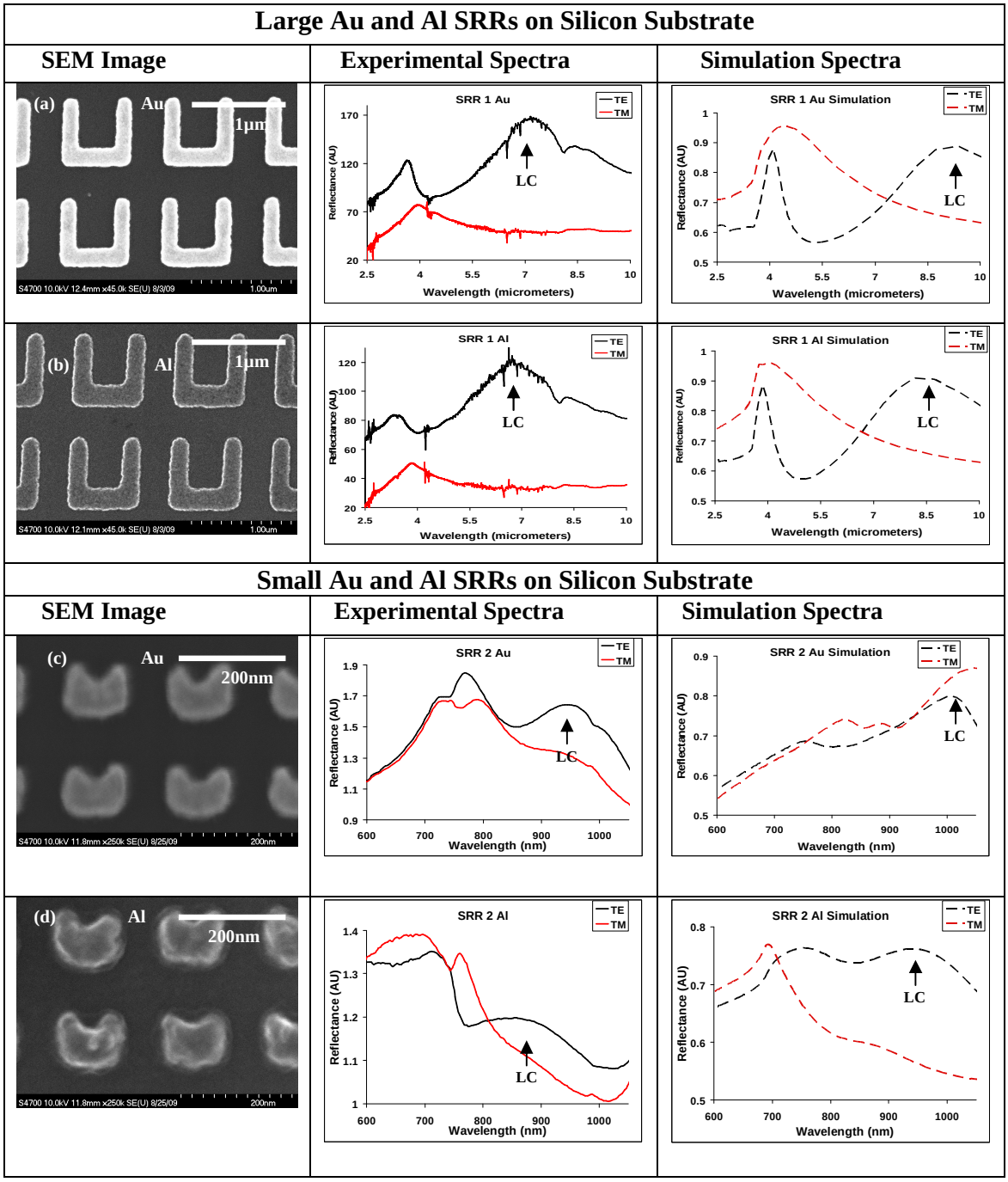


**Figure 2.1:** Table showing the reflectance spectra of the different SRR patterns fabricated on silicon. The first two rows are 'large' (~ 800 nm) SRRs with: (a) SRR 1 Au and (b) SRR 1 Al. The last two rows are 'small' (~150 nm) SRRs with: (c) SRR 2 Au and (d) SRR 2 Al, along with their corresponding experimental (solid curves) and

simulation (dashed) spectra. The black curves (solid and dashed) are for TE polarisation - and the red curves (solid and dashed) are for TM polarisation measurements.

In Figure 2.2 the position of magnetic resonance (LC peaks) of nominally identical Au and Al SRRs fabricated on silicon is compared.

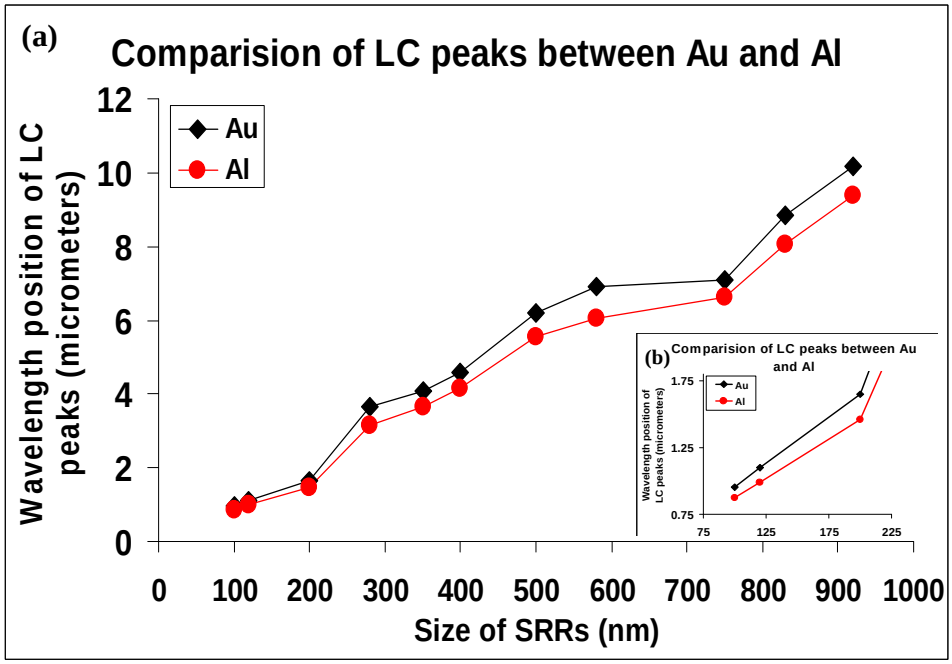


**Figure 2.2:** (a) LC peak positions of Al and Au SRRs fabricated on silicon. (b) Inset comparison of the position of LC peaks for Al and Au SRRs of size ~ 200 to 75 nm.

Figure 2.1 and Figure 2.2 shows that, for larger SRRs (with length dimensions in the range from ~ 1000 nm to 500 nm), the difference between the wavelengths of the Al and Au resonances is approximately 400 nm - but, as the size of the SRRs starts to reduce (below 300nm), the difference between the resonance positions also starts to shrink - and, for SRRs of size ~100 nm, the difference between the Al and Au resonance positions becomes less than 200 nm. This reduction in the difference can be attributed to the

saturation of the SRR resonances at higher frequencies, [8-9]. As described previously, at higher frequencies, the resonance of the SRRs no longer shifts to higher frequencies as the SRRs are reduced in size. At these higher frequencies (in the visible and near infrared regimes) the kinetic energy of the electrons in the metal limits the LC response [8-9].

In addition, at resonance wavelengths below the electronic band-gap of silicon (i.e. below 1.1 µm), illuminating the SRRs excites hole-electron pairs in the substrate - and thereby potentially reduces the magnitude of the resonances of both the LC and plasmonic peaks. This effect is believed to be the main reason for the diminished amplitudes of the resonances for the small sized SRRs on silicon, as compared with those for their larger counterparts.

Overall, apart from the broadening of the LC feature and the possible reduction in the LC resonance magnitude associated with aluminium, the differences between the spectra are not large. However the size of the total inductance (as proposed by Tretyakov [10]) that should be added while reinterpreting such structures at higher frequencies (and as also previously interpreted by Zhou et al [8]) is due to the additional kinetic inertia associated with the motion of the electrons, which depends on the choice of metal.

According to the Tretyakov model [10], if the length of the SRR is *l*, the width of its arm is *w* and the thickness (height) of the SRR is *h* and $\delta$ is the gap between the SRR arms (as shown in Figure 2.1) and assuming uniform current density over the cross section of the SRR, the LC resonant frequency of the SRR is given by:

$$\omega_{LC} = \frac{1}{\sqrt{(L + L_{add})(C + C_{add})}} \tag{2.1}$$

Where the additional capacitance and inductance are given by:

$$C_{add} = \frac{\varepsilon_0 \varepsilon_r wh}{l_{eff}} \; and \; L_{add} = \frac{l_{eff}}{\varepsilon_0 wh \omega_p^2} \tag{2.2}$$

Where $l_{eff}$ is the effective conductor length that Tretyakov [10] assumes to be $l_{eff} = (\pi/2)l$ and $\omega_p$ is the plasma frequency.

The additional inductance term, $L_{add}$, associated with the kinetic energy of the electrons depends strongly on the plasma resonance frequency and therefore on the choice of metal. This has been shown in previous work [17] where similar sized aluminium based SRRs showed LC resonance at higher frequencies than their equivalent gold counterparts. At frequencies below the plasma frequency, it is the strongly plasma-frequency dependent term for the kinetic inductance that plays a crucial role. Equation (2.2) indicates that this additional inductance is inversely proportional to the square of the plasma frequency of the metal. The plasma frequency of the metal is equal to 3750 THz for aluminium and

2175 THz for gold [21]. The higher plasma frequency of aluminium will result in a lower additional inductance ($L_{add}$) and therefore in a shorter resonance wavelength.

The reduction in the magnitude of the reflection resonance for aluminium SRRs can be attributed to the difference in the damping frequency of the metals. In the Drude model, the damping (collision) frequency is associated with absorption and losses. The damping frequency of aluminium is 19.4 THz and that of gold is 6.5 THz [21]. A metal having higher values of damping frequency tends to be more absorptive and lossy. Since aluminium has a higher damping frequency than gold, it is more absorptive and hence the magnitude of the response of an array of aluminium SRRs is lower than that of gold.

## 2.6 Effect of choice of different substrates

Apart from their physical size, the frequency of the LC resonance of an array of SRRs is also determined by the refractive index of the substrate supporting the SRR patterns [5, 22]. The SRRs fabricated on lower refractive index materials (e.g. silica) characteristically show their LC resonant response at higher frequencies than those fabricated on silicon. Figure 2.1 shows that the aluminium SRRs fabricated on silicon display an LC peak in the wavelength region around 930 nm. By keeping the dimensions and all other parameters of the smaller SRRs of Figure 2.1 similar, but changing the substrate to silica, it is possible to shift the LC response to even shorter wavelengths. So, by fabricating very small aluminium based SRRs on silica substrates, it is possible to obtain an LC resonant response at visible wavelengths. Figure 2.3 shows results for

different sized Au and Al SRRs fabricated on silica, displaying LC peaks in the visible part of the spectrum.

As shown in Figure 2.3 the aluminium based SRRs of dimensions (*l*) varies from ~150 nm to ~100 nm fabricated on silica, displays the LC resonance between 680 nm to as low as 530 nm wavelengths, well inside the visible spectrum region. Whereas the smallest dimension (*l*) of ~100 nm gold based SRRs fabricated on silica displays the LC peak at 720 nm, just on the edge of the visible spectrum. This clearly demonstrates the advantage of aluminium based SRRs in pushing the magnetic resonance (LC resonance) to higher frequency visible spectrum when compared with their gold based counterparts.

Again, as in previous case the experimental results are in moderate agreement with the simulated spectra. The reasons are attributed to the fabrication imperfection as in previous case.

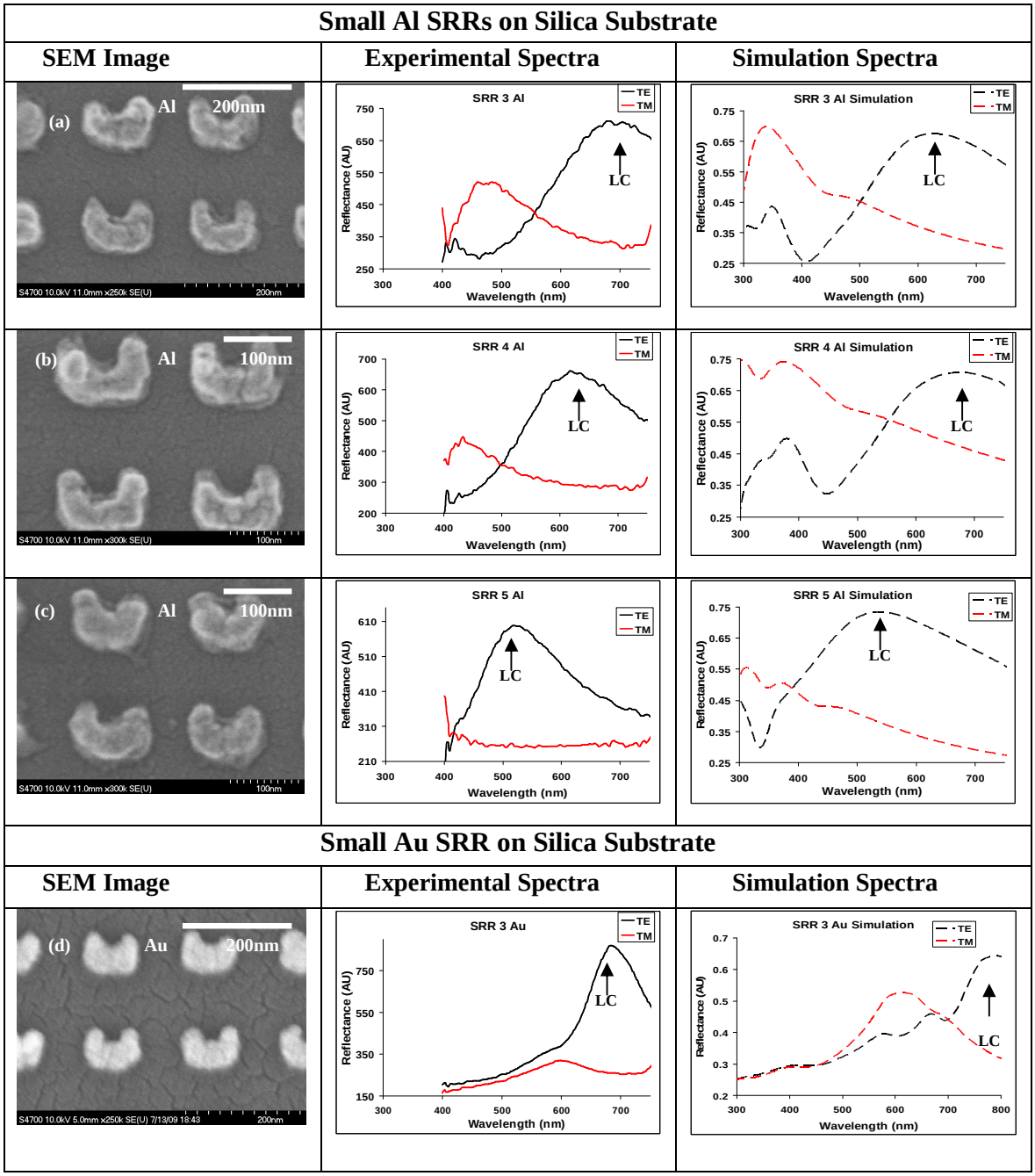


**Figure 2.3:** Table showing the reflectance spectra of the different SRR patterns fabricated on silica. The first three rows are small sized (~ 150 to 120 nm) aluminium SRRs with (a) SRR 3 Al (b) SRR 4 Al and (c) SRR 5 Al and the last row is small sized (~ 120 nm) gold SRR with (d) SRR 3 Au along with their corresponding experimental (solid

curves) and simulation (dashed curves) spectra. Black curves (solid and dashed) are TE and Red curves (solid and dashed) are TM measurements.

In Figure 2.4, TE field plots of SRR 4-Al at both the plasmonic and LC resonant peaks is shown.

**(a)**

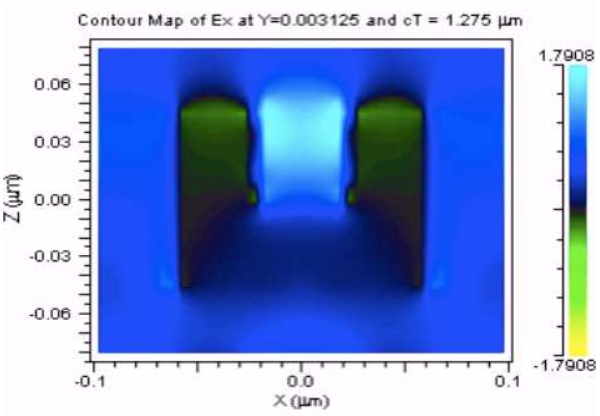


**Fig. 2.4 (a):** Field profile of SRR-4 Al at the plasmonic resonance peak (370 nm).

**(b)**

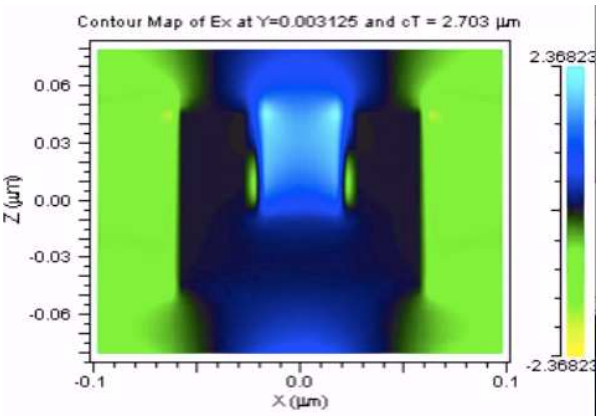


**Figure 2.4 (b):** Field profile of SRR-4 Al at the LC resonance peak (670 nm).

Figure 2.4 clearly shows the different distributions of the optical electric field for the two different resonances. In the case of the plasmon resonance, the phase and amplitude of the optical electric field has a uniform distribution around the SRR structure - and it is in phase with the field in the gap of the SRR. The LC resonance on the other hand exhibits a completely different situation, in which the optical electric field between the arms of the SRRs is in anti-phase with the light on either side of the SRR structure. From this difference in behaviour, it may be inferred that the LC resonance condition is a fundamentally different one from the plasmonic resonance condition. The description of the resonance behaviour shown here therefore differs from that of reference [6], but is consistent with that of Linden et al [3].

## 2.7 Conclusions

It has been shown that, at higher frequencies, both the dimensions and the individual metal properties play an important role in determining the resonant response of arrays of SRRs. In particular, it has been demonstrated that the use of aluminium, due to its bulk plasma frequency being higher than that of gold, enables a large shift of the magnetic response towards shorter wavelengths. Finally, this property of aluminium is utilised for the fabrication of Al-based SRRs on low refractive index substrates, i.e. silica, to demonstrate clear magnetic resonances of SRRs at visible frequencies as short as 530 nm.

## Acknowledgement

The author wishes to express his gratitude to Dr. Scott McMeekin of Glasgow Caledonian University for the carrying out the modelling of all the fabricated structures shown in this chapter and for discussions regarding the analysis of the results.

# References

1. V. G. Veselago , “The electrodynamics of substances with simultaneously negative values of ε and μ.” Sov Phys. 10, 509-514 (1968).

2. J.B. Pendry, A.J. Holden, D.J. Robbins, and W.J. Stewart, “Magnetism from conductors and enhanced Non-Linear Phenomena,” IEEE Trans. Microwave Theory Tech., 47, 2075-2084 (1999).

3. S. Linden, C. Enkrich, M. Wegener, J. Zhou, T. Koschny and C.M. Soukoulis, “Magnetic Response of Metamaterials at 100 THz,” Science, 306, 1353-1361 (2004).

4. V.M. Shalaev, “Optical negative index metamaterials,” Nature Photonics, 1, 41-48 (2007).

5. S. Linden, C. Enkrich, G. Dolling, M. W. Klein, J. Zhou, T. Koschny, C. M. Soukoulis, S. Burger, F. Schmidt and M. Wegener, “Photonic Metamaterials: Magnetism at Optical Frequencies,”IEEE journal of selected topics in quantum electronics, 12, 1097-1103 (20006).

6. C.Rockstuhl and F. Lederer, C. Etrich, T. Zentgraf and J. Kuhl, H. Giessen, “On the reinterpretation of resonances in split-ring resonators at normal incidence,” Optics Express 14, 8827-2236 (2006).

7. B. Kante, A. de Lustrac, and J. M. Lourtioz, “In-plane coupling and field enhancement in infrared metamaterial surfaces,” Phys. Rev. B, 80, 035108 1-6 (2009).

8. J. Zhou T. Koschny, M. Kafesaki, E.N. Economu, J.B. Pendry and C.M. Soukoulis, “Saturation of the magnetic response of split ring resonators at Optical frequencies,” Physics Review Letters, 95, 223902 1-4 (2005).

9. M.W. Klein, C. Enkrich, M. Wegener, C.M. Soukoulis and S. Linden, “Single split ring resonators at optical frequencies: limits of size scaling,” Opt. Letters. 31. 1259-1261 (2006).

10. S.Tretyakov, “On geometrical scaling of split-ring and double bar resonators at optical frequencies,” Metamaterials 1, 40-43 (2007).

11. F. Gadot, B. Belier, A. Aassime, J. Mangeney, A de Lustrac, J.-M Lourtioz, “Infrared response of a metamaterial made of gold wires and split ring resonators deposited on silicon,” Optical Quantum Electronics, 39, 273-284 (2007).

12. U.K. Chettiar, A.V. Kildishev, T.A. Klar and V.M. Shalaev, “Negative index metamaterial combining magnetic resonators with metal films,” Optics Express. 14, 7872-7877 (2006).

13. S. Zhang, W. Fan, K.J. Malloy and S. R. J. Brueck, “Demonstration of metal-dielectric negative index metamaterials with improved performance at optical frequencies,” J. Opt. Soc. Am. B 23, 434-438 (2006).

14. G. Dolling, C. Enkrich and M. Wegener, C.M. Soukoulis, S. Linden, “Low loss negative index metamaterial at telecommunication wavelengths,” Opt. Letters. 31, 1800-1802 (2006).

15. H-K. Yuan, U.K. Chettiar, W. Cai, A.V. Kildishev, A. Boltasseva, V.P. Drachev and V.M. Shalaev, “A negative permeability material at red light,” Optics Express 15, 1076-1083 (2007).

16. C. Enkrich, F. P.Willard, D. Gerthsen, J. Zhou, T. Koschny, C. M. Soukoulis, M. Wegener and S. Linden, "Focused-Ion-Beam Nanofabrication of Near-Infrared Magnetic Metamaterials," Advanced Materials 17, 2547-2549 (2005).

17. N.P. Johnson, A.Z. Khokhar, H. M. H. Chong, R. M. De La Rue and S. McMeekin, "Characterisation at infrared wavelengths of metamaterials formed by thin-film metallic split-ring resonator arrays on silicon," Electronics Letters 42, 1117-1119 (2006).

18. http://www.rsoftdesign.com/products.php?sub=Component+Design&itm=FullWAVE. 2nd December 2009.

19. W.J. Padilla and A.J. Taylor, C. Highstre and M. Lee, R. D. Averitt, "Dynamic Electric and Magnetic Metamaterial Response at Terahertz Frequencies," Phys Rev Lett. 96, 107401 1-4 (2006).

20. H-T Chen, W.J. Padilla, J. M. O. Zide, S. R. Bank, A.C. Gossard, A. J. Taylor and R. D. Averitt, "Ultrafast optical switching of terahertz metamaterials fabricated on ErAs/GaAs nanoisland superlattices," Opt. Letters. 32. 1620-1622 (2007).

21. I. El-Kady, M. M. Sigalas, R. Biswas, K. M. Ho, and C. M. Soukoulis, "Metallic Photonic crystals at optical wavelengths," Physical Rev.B 62, 15 299 (2000).

22. Z. Sheng and V.V, Varadan, "Tuning the effective properties of metamaterials by changing the substrate properties," J. Appl. Physics. 101, 014909 4-7 (2007).

# Chapter 3

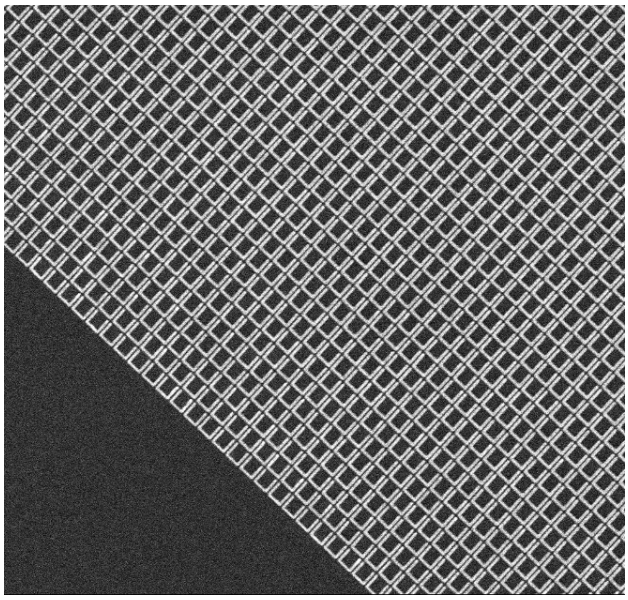

# Impact of titanium adhesion layers on the response of metallic split-ring resonators (SRRs)

In the previous chapter it has been shown that, at higher frequencies, both the dimensions and the individual metal properties play an important role in determining the resonant response of arrays of SRRs. As a result, a substantial shift between the responses of arrays of gold based and aluminium based SRRs were observed. Deposition of gold SRRs onto dielectric substrates (silicon and silica) typically involves the use of an additional adhesion layer. Titanium is the most common adhesion layer used to attach gold films on to dielectric substrates. This chapter investigates on the impact of the titanium adhesion layer on the overall response of gold based SRRs. The results quantify the extent to which the overall difference in the resonance frequencies between gold and aluminium based SRRs is due to the presence of the titanium adhesive layer. It is shown that even a 2 nm thick titanium layer can red-shift the SRR resonance by 20 nm. Finally, it is demonstrated that by an appropriate addition of titanium to the gold based SRRs, their overall resonant response can be tuned. However, the addition of titanium also results in a reduction of the resonance magnitude.

## 3.1 Introduction

At lower frequencies, up to several terahertz, the magnetic resonance (i.e. the LC resonance) of an SRR scales reciprocally with its characteristic dimensions. However, at higher frequencies (optical and mid-infrared regimes), metals do not behave like perfect conductors and start behaving according to the (complex) Drude model - and therefore this model determines the overall response of the SRR structures [1-2]. Titanium is one of the most common adhesion layer used to deposit gold based SRRs onto dielectric substrates [3-6]. However, in most of the previous work carried out on gold based nano SRRs the effect produced by the titanium adhesion layer of variable thickness has essentially been ignored [3-6]. It is required to realise and quantify the effect of the titanium adhesion layer on the overall response of gold based SRRs to find an optimised thickness for the adhesion layer. This will help in a more accurate prediction of resonance responses of gold based SRRs. It will also provide a better understanding of the shift produced between the responses of aluminium based SRRs and gold based SRRs with titanium adhesion layer. Optimisation of the titanium adhesion layer's thickness may also open up possibilities for tuning the SRR resonances as described in later parts of this chapter.

In this chapter, the fabricated, measured and simulated responses of SRRs with characteristic planar dimensions as small as 200 nm were considered. The structures were composed of either aluminium (Al) or gold (Au) layers, together with a variable amount of titanium (Ti) adhesion layer, while keeping constant the overall SRR thickness at 50 nm. A medium doped n-type silicon substrate with resistivity ~ 100 Ω.cm was used in

all cases. The fabrication was performed using direct-write electron beam lithography in a Vistec VB6 machine, at 100 kV. The multi-component metallic layers were deposited onto the silicon using electron-beam evaporation. The patterns were written over an area of around $300\ \mu m \times 300\ \mu m^2$.

The reflectance measurements were performed at normal incidence with a $\times 10$ microscope objective (NA = 0.25), using a white light source and monochromator with an InGaAs detector operating in the range from 0.8 to 1.6 µm - together with a lock-in amplifier. The measurements were taken for two orthogonal linear polarizations of the incident light (TE and TM polarization) - and were then normalized with respect to the reflectivity of a bare silicon substrate.

The responses of closely similar-sized Au- and Al-based SRRs are shown in Figure 3.1.

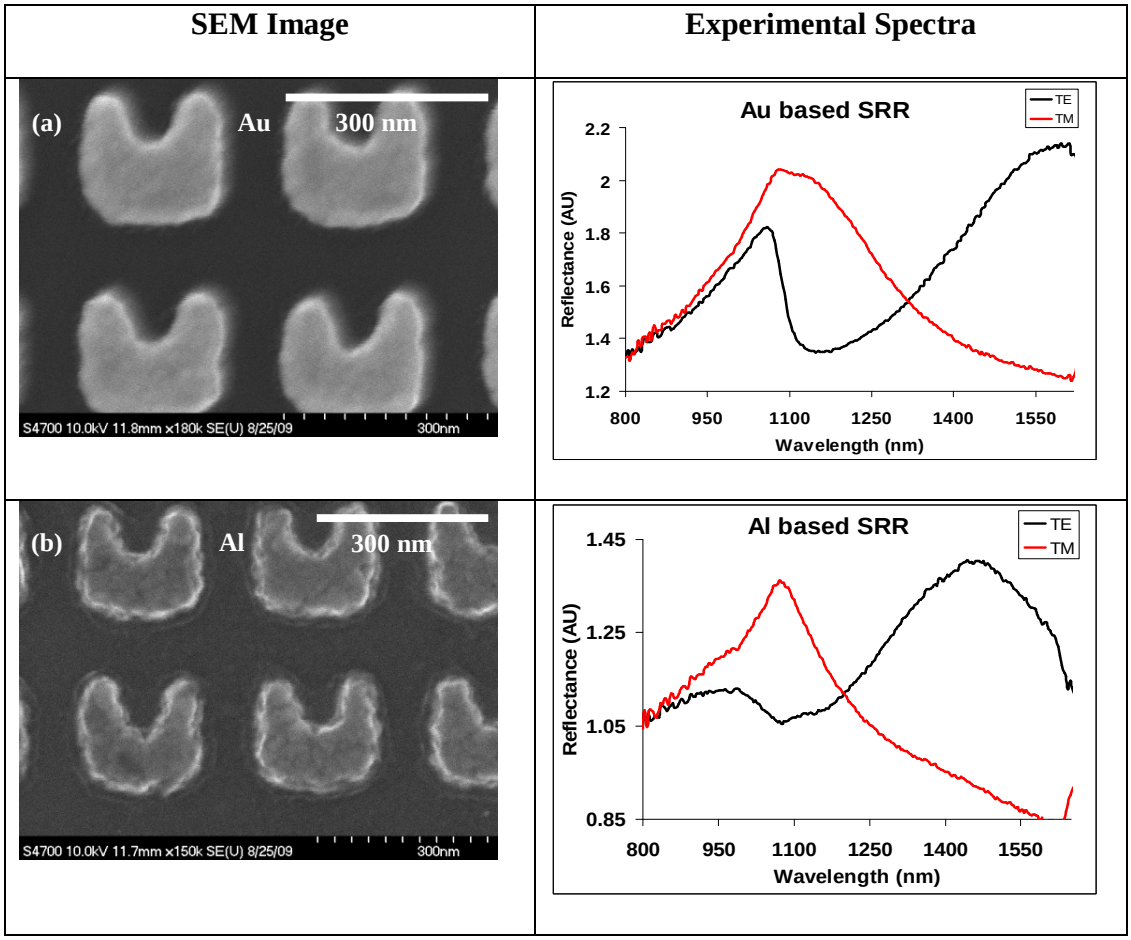


**Figure 3.1:** SEM micrographs of fabricated SRRs and their corresponding experimental reflectance spectra for TE/TM polarization: (a) 48-nm-thick gold SRRs with 2 nm of Titanium adhesion layer; (b) 50-nm-thick aluminium SRRs.

At infrared and optical frequencies the complex dielectric function $\varepsilon$ and complex refractive index $n_c$ is given as [7]

$$\varepsilon = \varepsilon_1 + i\varepsilon_2 = n_c^{\,2} = (n + i\kappa)^2 \qquad (3.1)$$

Where, $\varepsilon_1 \; and \; \varepsilon_2$ are the relative real and imaginary parts of the complex dielectric function.

According to the Drude Model, the real and imaginary part of the dielectric function are given as [7]

$$\varepsilon_1 = \varepsilon_\infty - \frac{\omega_p^2}{\omega^2 + \omega_\tau^2}, \qquad (3.2)$$

$$\varepsilon_2 = \frac{\omega_p^2 \omega_\tau}{\omega^3 + \omega\omega_\tau^2}. \qquad (3.3)$$

Where $\omega_p \; and \; \omega_\tau$ are plasma frequency and collision frequency respectively. The values of $\omega_p \; and \; \omega_\tau$ for gold are 2175 THz and 6.5 THz whereas those of aluminium are 3750 THz and 19.4 THz [7-8].

As shown in the previous chapter, and from Figure 3.1, the higher plasma frequency $(\omega_p)$ of aluminium based SRRs results in shorter resonance wavelength as compared to gold based SRRs. On the other hand, the higher collision frequency $(\omega_\tau)$ of aluminium, results in lower magnitude of resonance for aluminium based SRRs.

## 3.2 Modelling

Dr. Rafal Dylewicz modeled all the SRR structures described in this chapter. The resonant response of the SRRs was calculated using a fully three-dimensional (3-D) simulation of the fabricated device, with an initial SRR thickness of 250 nm. Due to the computational requirements, i.e. the very small mesh size for the original thickness of 50 nm, the increased SRR thickness of 250 nm was used, after convergence tests were performed. The numerical simulations were performed with a commercial finite-difference time-domain method (FDTD) software package from Lumerical. The transmission and reflection characteristics were calculated from a single unit cell for two different optical polarizations, over a wide range of wavelengths. A Drude model was used to describe the frequency-dependent material properties. An integer number of cells with a mesh-size of 2 nm were applied within the metallic layers, while non-uniform and coarser meshing was used in the surrounding regions. The plasma frequencies and collision frequencies were initially adjusted to match those of pure aluminium and gold structures. The effective values in nanostructures can differ from their bulk values because the electrons do not experience the full effect of the bulk metal, as the fraction of the electric field outside the structure is larger for a nanostructure and results in an additional inductance [9]. The material properties of a particular film were estimated via linear interpolation from the respective plasma frequencies and collision frequencies for gold and titanium, as a function of the relative Au/Ti content in the total thickness. This phenomenological approach was taken because the software was found not to be capable of accurately modeling the behaviour of very thin layers (~ 2 nm).

## 3.3 Effect of Titanium adhesion layer

In order to examine how much the titanium adhesion layer contributes to the overall response of the gold SRRs, two different sets of experiments were performed. In the first set of experiments, the overall thickness of the Au/Ti SRR was kept constant at 50 nm, while the thickness of the titanium adhesion layer was increased at the expense of Au. The effect of increasing titanium thickness in such mixed Au/Ti SRRs is shown in Figure 3.2. By increasing the fractional amount of titanium in the composition, both plasmonic and magnetic peaks move towards longer wavelengths - and diminish in amplitude.

It can be seen from Figure 3.2 that the experimental results are in moderate agreement with the simulated spectra. The discrepancy between the two sets of results could be attributed to the imperfect SRR shapes fabricated and measured in experimental results as compared to the perfect SRR shapes simulated in modelling. At the same time the experimental results are based on an array structure, whereas the modelling is performed on only one SRR structure.

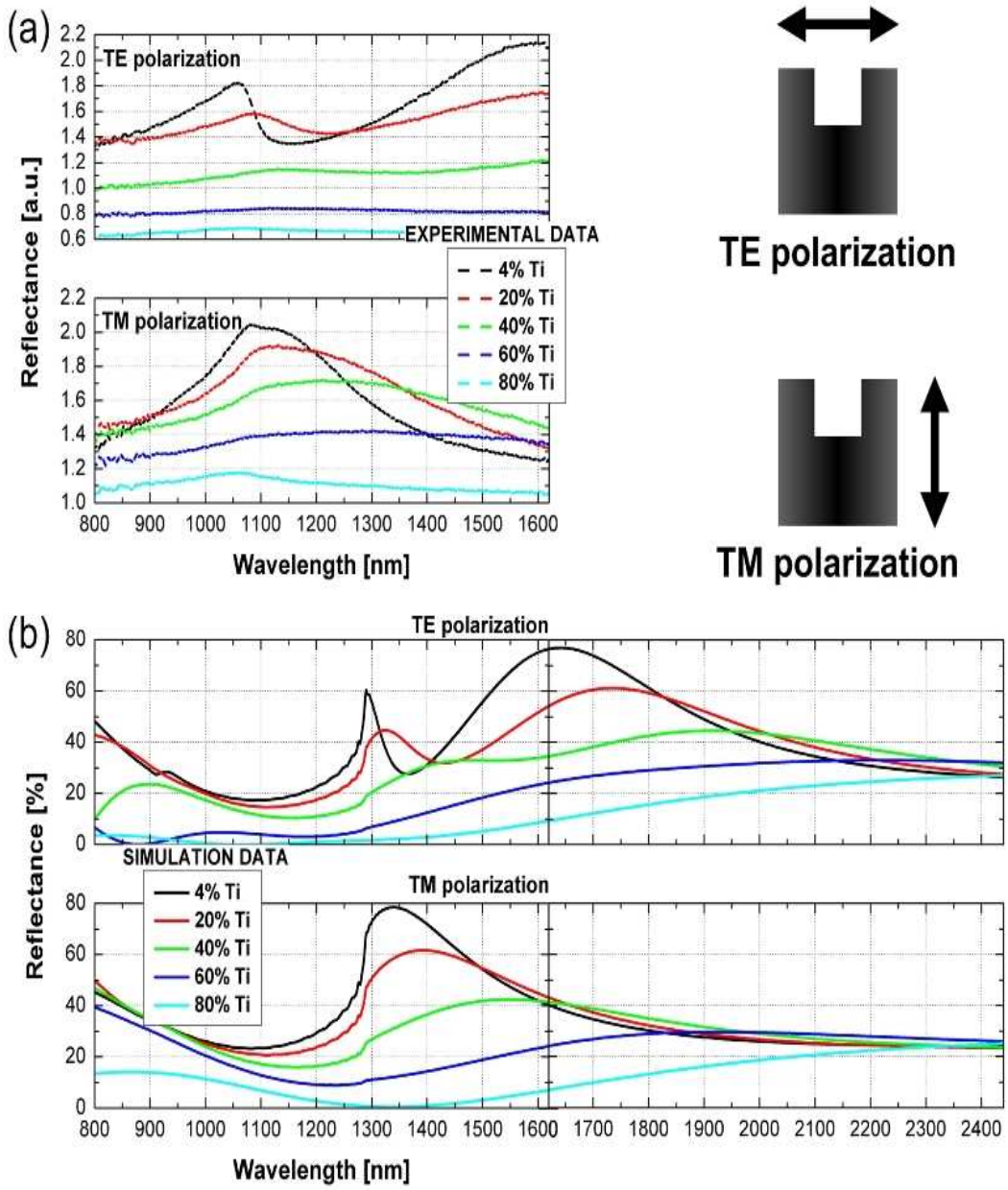


**Figure 3.2:** Reflection spectra of dual-layer SRRs with increased titanium quantity, where the overall Au/Ti thickness is kept constant: (a) experimental spectra at two different polarizations; (b) calculated spectra for the extended wavelength range.

The results obtained by increasing the amount of titanium as shown in Figure 3.2 can be explained as following. From Ordal *et al.* [7] the collision frequency $(\omega_\tau)$ and plasma frequency $(\omega_p)$ are associated with the complex dielectric function as,

$$\omega_\tau = \frac{\omega\varepsilon_2}{1-\varepsilon_1} \qquad (3.4)$$

$$\omega_p^2 = (1-\varepsilon_1)(\omega^2 + \omega_\tau^2) \qquad (3.5)$$

For $\omega = 6451.61\,\text{cm}^{-1}$ that is equivalent to wavelength of 1.55 µm

We get the corresponding values of $-\varepsilon_1 = 6.56$ and $\varepsilon_2 = 33.3$ for titanium from [7].

Putting the values of $\omega, \varepsilon_1 and \varepsilon_2$ into equations (3.4) and (3.5) we get

Collision frequency of Titanium $\omega_\tau = 135.68$ THz

Plasma frequency of Titanium $\omega_p = 382.56$ THz

Thus, the value calculated for the plasma frequency for titanium is 382.56 THz, which is almost one order of magnitude lower than for the other metals. Additionally, titanium is characterized by a very high damping frequency of 135.68 THz, which is associated with absorption and losses. As titanium is added to the system, the response is red-shifted and becomes progressively noisy and is accompanied by a reduction in the reflectance magnitude.

In the second set of experiments, the thickness of the titanium adhesion layer was gradually increased, while the thickness of the gold layer was kept constant at 48 nm. In this case, the total thickness of the SRRs also increased progressively. In Figure 3.3 a similar trend is observed, i.e. by increasing the amount of titanium in the system, the overall resonant response degrades. However, by maintaining the gold thickness at a constant value, the reflectance response of the SRRs becomes larger in amplitude - and the flattening of the curves for high titanium content layers is no longer apparent. The increased total thickness of the SRRs increases the effective plasma frequency and gives a blue-shift to the peak positions. In this experiment, a trade-off occurs between the increased titanium thickness - which pushes the response towards longer wavelengths while progressively suppressing the peaks - and the increased total thickness, which causes a blue-shift in the resonance peaks. It can be confirmed from the results shown in Figures 3.2 and Figure 3.3 that increasing the titanium fraction has reduced the observable response nearly to zero, once it forms more than 40 % of the overall thickness. The primary conclusion from these results is that the greater absorption in the titanium dominates the overall behaviour, once it is present in sufficiently large amounts - even when the amount of gold is undiminished.

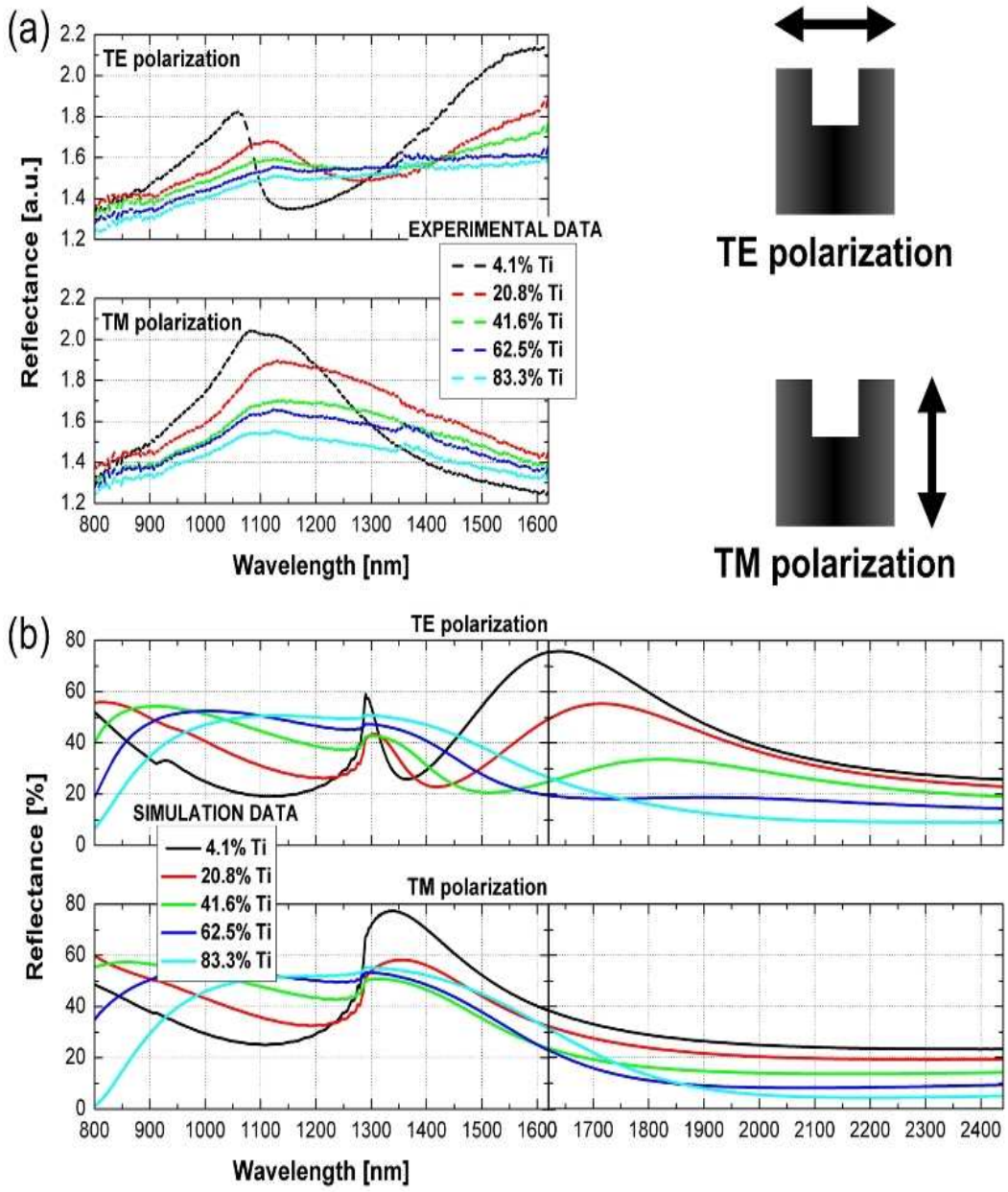


**Figure 3.3:** Reflection spectra of dual-layer SRRs with increased titanium fraction and total system thickness, while the Gold thickness is kept constant: (a) experimental spectra at two different polarizations; (b) calculated spectra for the extended wavelength range.

The effect of the titanium-induced red-shift of both the plasmonic and magnetic resonances of the Au/Ti bi-layer SRRs is shown in Figure 2. 4. From Figure 3.4 it can be seen that the presence of a 2-nm-thick Ti layer (4% Ti) can shift the SRR response by 20 nm.

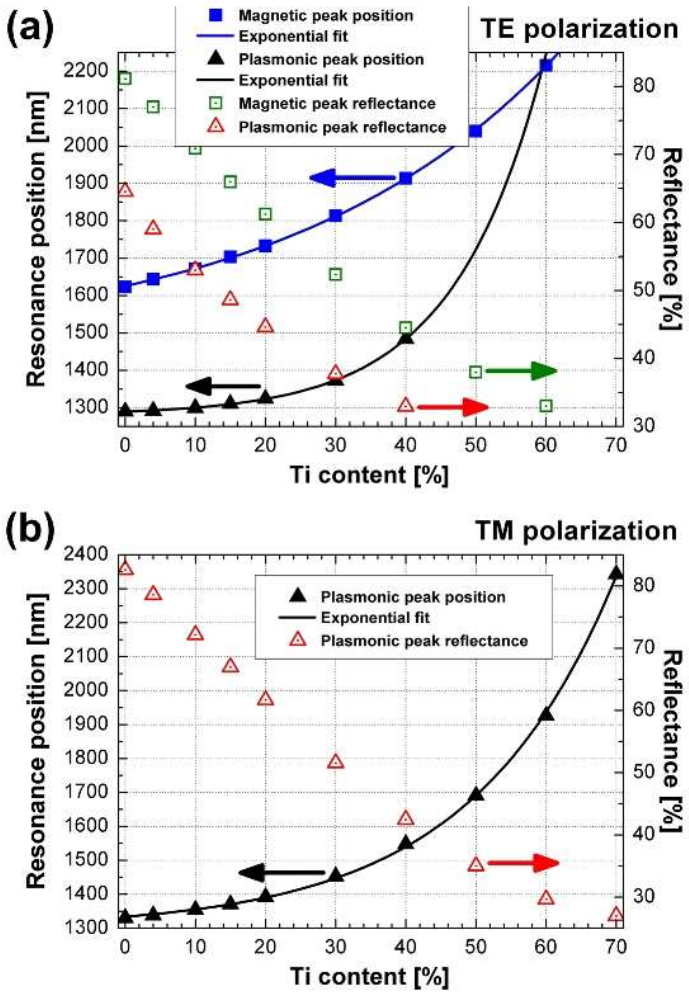


**Figure 3.4:** Calculated titanium-induced change in resonance position and amplitude for dual-layer SRR as a function of Titanium thickness. The overall thickness of Au/Ti SRR is kept constant: results for (a) TE and (b) TM polarization.

## 3.4 Calculation of Skin depth

It has been shown previously, that the penetration of field inside metals, at higher frequency range (optical and mid-infrared regimes), is restricted by their skin depth [10-12]. To calculate the skin depths of both gold and titanium, the respective values of their conductance is required.

The relationship between the relative real ( $\varepsilon_1$ ) and imaginary parts ( $\varepsilon_2$ ) of the electric permittivity is given by [13]

$$\varepsilon_2 \approx \frac{\sigma}{\omega \varepsilon_1 \varepsilon_0} \tag{3.6}$$

Where, $\sigma$ is the conductance, and $\varepsilon_o$ is the permittivity of free space.

At wavelength of 1.55 µm the value of $\sigma$ for gold is calculated. From Ordal *et al*. [7] the value of $\varepsilon_1 \; and \; \varepsilon_2$ for gold at 1.55 µm wavelength is found to be 104 and 3.68 respectively. By substituting these values in equation (3.6)

$$3.68 \approx \frac{\sigma_{Au}}{\left(\frac{2\pi \times 3 \times 10^8}{1.55 \times 10^{-6}}\right) \times 104 \times \varepsilon_0} \tag{3.7}$$

$$or \;\; \sigma_{Au} \approx 4.12 \times 10^6 \; S/m$$

Similarly, at wavelength of 1.55 µm the value of $\sigma$ for titanium is calculated. From Ordal *et al.* [7] the values of $\varepsilon_1$ *and* $\varepsilon_2$ for titanium at 1.55 µm wavelength is found to be 6.56 and 33.3 respectively. By substituting these in equation (3.6)

$$\sigma_{Ti} \approx 2.35 \times 10^6 S/m$$

The skin depth ($\delta$) of a metal is given as [13]

$$\delta = \left( \frac{2}{\omega \mu_r \mu_0 \sigma} \right)^{\frac{1}{2}} \qquad (3.8)$$

Where, $\mu_r$ is the relative permeability of the material and is assumed always as 1 [14] and $\mu_0$ is the permeability of free space.

The skin depth ($\delta_{Au}$) of gold at wavelength 1.55 µm is calculated by substituting the values of ($\sigma_{Au}$) into equation (3.8)

$$\delta_{Au} = \left( \frac{2}{1.216 \times 10^{15} \times \mu_0 \times 4.12 \times 10^6} \right)^{\frac{1}{2}} \qquad (3.9)$$

or $\delta_{Au} = 17.82\ nm$

Similarly, the skin depth ($\delta_{Ti}$) of titanium at wavelength 1.55 µm is calculated by substituting the values of ($\sigma_{Ti}$) into equation (3.8)

$$\delta_{Ti} = \left( \frac{2}{1.216 \times 10^{15} \times \mu_0 \times 2.35\ X\ 10^{6}} \right) \qquad (3.10)$$

or $\delta_{Ti} = 23.59\ nm$

From the above calculations, the skin depths of titanium and gold have been estimated to be nominally 18 nm and 24 nm respectively at ~ 1.55 μm. For these measurements the effective gold thickness is limited by its skin depth. However, as the titanium content increases, it is able to contribute to the conduction by as much as 1.3 times the skin depth. Qualitative information on the expected dissimilarity in skin depths and field penetration inside different metals is presented in Figure 3.5. Electric field profiles were numerically calculated using the same FDTD software (Lumerical), where SRRs with different metal properties were investigated. Simulated electric field distributions (in logarithmic scale) within nano-sized SRR and its air surroundings are presented for a pure Au layer and mixed Au/Ti layers, which compromise growing Ti addition, up to 70% of titanium content. These results were obtained for TM polarized light at the certain wavelengths of plasmonic resonance, for a given Ti inclusion. From the cross-sections shown in Figure 3.5, it is seen that maximum intensity of electric field is observed outside the metal layer, due to the incident and reflected plane wave, while moderate and low intensity appears on the edges and within the metal itself, respectively. An increase in penetration depth inside SRR (Figs. 3.5b, 3.5c and 3.5d), as compared to pure Au case, is strongly related to the raised Ti content. Such a tendency is in good agreement with theoretical skin depth values for Au and Ti, calculated with use of equation (3.8), and additionally explain the

titanium-induced behaviour of plasmonic and magnetic resonances observed in Figure 3 4.

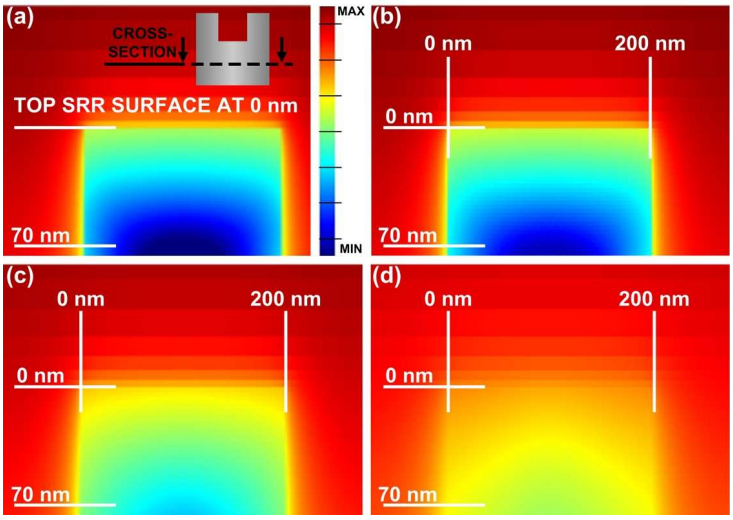


**Figure 3.5:** Skin depth effect observed in calculated electric field profiles (log scale) for nano-sized SRR at the plasmonic resonance condition: (a) pure Au layer; (b) layer with 4% of Ti thickness; (c) layer with 40% of Ti thickness; (d) layer with 70% of Ti thickness.

A strongly composition-dependent behaviour, the movement of the resonance towards longer wavelengths is clearly observed, as well as strongly diminishing amplitude of these effects, for both light polarizations. For titanium thickness > 40% of the total SRR thickness, the reflectance of both the plasmonic and magnetic resonance peaks is reduced to about half of its initial/maximum value. Although the amplitude is reduced, addition of titanium (up to 40%) provides additional tuning possibilities for both the electric and magnetic resonance peaks of SRRs, as shown in Figure 3.4.

To understand the impact of the titanium adhesion layer on the observed difference between the responses of 50 nm thick aluminium-based SRRs and of mixed Au/Ti-based SRRs (Figure 3.1), an additional experiment was performed. A titanium adhesion layer 2 nm thick was added into the 48 nm-thick aluminium SRRs and the response was compared to that of pure aluminium-based SRR (50 nm) of Fig. 3.1b. The results are shown in Figure 3.5, where a red-shift of about 20 nm is observed for both peaks, when compared to the 50 nm-thick aluminium SRRs. This result further corroborates the calculated results described in Figure 3.4.

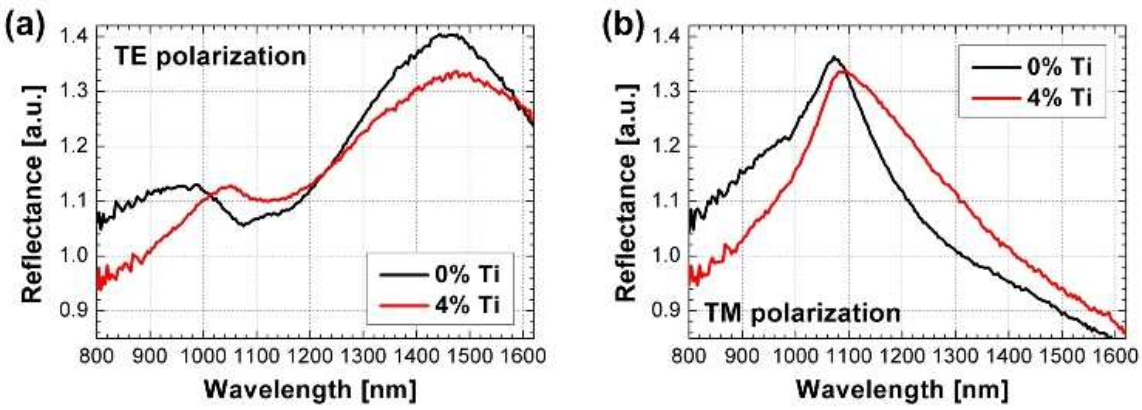


**Figure 3.6:** Comparison between the experimental reflectance spectra of 50 nm-thick aluminium with that of 2 nm titanium + 48 nm aluminium SRRs: (a) results for TE polarization; (b) results for TM polarization.

Hence, the difference in the responses of the gold and aluminium based SRRs is mainly caused by their material properties, i.e. because of the lower value of gold plasma frequency from that of aluminium. Thus, at optical frequencies, apart from the size of the

SRRs, the plasma frequency of the particular metal used determines the position of the resonance - with the collision frequency determining the amplitude of reflectance.

## 3.5 Conclusions

In conclusion, the influence of titanium adhesion layers on the responses of gold and aluminium based SRRs has been quantified. The presence of a titanium adhesion layer of thickness 2 nm can produce a red shift of around 20 nm. Addition of titanium can be utilised for tuning the response of gold based SRRs, but it also reduces the overall magnitude of resonance, due to the high absorptive nature of titanium. Therefore, it is recommended that the thickness of the titanium adhesion layer should be kept minimum (~2 nm) to get stronger resonances at shorter wavelengths. Also, the difference in resonance positions between 50 nm thick aluminium based SRRs and SRRs with 2 nm titanium and 48 nm of gold is primarily due to the difference between the material properties of aluminium and gold. Finally, the thickness of the titanium adhesion layer should be an important consideration whilst performing the numerical simulation as well as measurement of gold based SRRs.

## Acknowledgement

The author wishes to express his gratitude to Dr. Rafal Dylewicz for the carrying out the modelling of all the fabricated structures shown in this chapter and for discussions regarding the analysis of the results.

# References

1. J. Zhou, T. Koschny, M. Kafesaki, E. N. Economou, J. B. Pendry, and C. M. Soukoulis, “Saturation of the magnetic response of split ring resonators at Optical frequencies ,” Physical Review Letters 95, 223902 1-4 (2005).

2. S. Tretyakov, “On geometrical scaling of split-ring and double-bar resonators at optical frequencies,” Metamaterials 1, 40-43 (2007).

3. B. Kante, A. de Lustrac, and J. M. Lourtioz, “In-plane coupling and field enhancement in infrared metamaterial surfaces,” Phys. Rev. B, 80, 035108 1-6 (2009).

4. F. Gadot, B. Belier, A. Aassime, J. Mangeney, A de Lustrac, J.-M Lourtioz, “Infrared response of a metamaterial made of gold wires and split ring resonators deposited on silicon,” Optical Quantum Electronics, 39, 273-284 (2007).

5. B. Lahiri, A.Z. Khokhar, R.M. De La Rue, S. G. McMeekin, and N.P. Johnson, “Asymmetric split ring resonators for optical sensing of organic materials,” Optics Express. 17, 2 1107- 1115 (2009).

6. B. Kante, J.-M. Lourtioz, and A de Lustrac, “Infrared metafilms on a dielectric substrate,” Phys. Rev. B, 80, 205120 1-5 (2009).

7. M. A. Ordal, L. L. Long, R. J. Bell, S. E. Bell, R. R. Bell, R. W. Alexander Jr., and C. A. Ward, “Optical properties of the metals Al, Co, Cu, Au, Fe, Pb, Ni, Pd, Pt, Ag, Ti, and W in the infrared and far infrared” Applied Optics 22 (7), 1099-1119 (1983).

8. I. El-Kady, M. M. Sigalas, R. Biswas, K. M. Ho, and C. M. Soukoulis, “Metallic Photonic crystals at optical wavelengths,” Physical Rev.B, 62, 15 299-302 (2000).

9. S. Linden, C. Enkrich, M. Wegener, J. Zhou, T. Koschny and C.M. Soukoulis, "Magnetic Response of Metamaterials at 100 THz," Science, 306, 1353-1361 (2004).

10. E.V. Ponizovskaya and A.M. Bratkovsky, "Metallic negative index nanostructures at optical frequencies: losses and effect of gain medium," Appl. Phys. A, 87, 161-165 (2007).

11. W. L. Barnes, A. Dereux and T. W. Ebbesen, "Surface plasmon subwavelength optics," Nature, 424, 824-830 (2003).

12. V. D. Kumar, K. Asakawa, "Investigation of a slot nanoantenna in optical frequency range," Photonics and Nanostructures – Fundamentals and Applications, 7, 161–168 (2009).

13. A. David Olver, Microwave and Optical Transmission (John Wiley and sons, 1992) Chapter 8.

14. John Gowar, *Optical Communication Systems* (Prentice Hall, 2nd Edition 1996) Chapter 3.

# Chapter 4

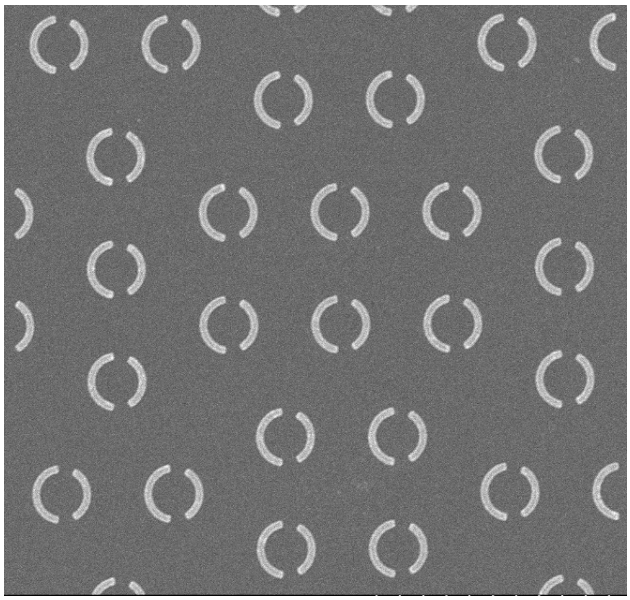

# Asymmetric split ring resonators (A-SRRs) and their properties

In this chapter the properties of “C-shaped” Asymmetric Split Ring Resonators (A-SRRs) are studied. By producing asymmetry in the structures, the two arms of the ring produce distinct plasmonic resonances related to their lengths – but are also affected by the presence of the other arm. This combination leads to a steepening of the slope of the reflection spectrum between the resonances that increases the sensitivity of the resonant behavior to the addition of different molecular species. This chapter describes the experimental results, supported by simulation, on the resonances of a series of circular split ring resonators with different gap and section lengths – at wavelengths in the mid-infra red regions of the spectrum. The asymmetry in the structure gives rise to higher quality factor resonances in optical metamaterials and this property has been utilised, in work described in the next chapter, for highly sensitive detection of organic compounds. Part of this chapter has been published in Optics Express Vol. 17, No. 2, 1107-1115 (2009).

## 4.1 Introduction

In the previous chapters, it is seen that metamaterials based on nano-scale metallic split ring resonators (SRRs) can be used to produce resonant responses in the visible and mid-infrared wavelength range. However, the quality factor of resonance associated with metamaterials is usually low due to the strong coupling of the SRRs with free space and that result in radiation losses [1]. This lossy nature of SRRs and its broad resonant response makes it difficult for practical and efficient implimentation of metamaterials in applications such as optical sensors. A high quality factor is desirable if the structures are used as sensors, because a shift in a sharp peak is easier to detect than a shift in a gentle slope. As seen in previous chapters, at optical frequencies metals stop behaving as nearly perfect conductors and start to become absorptive and hence lossy, in accordance with the Drude model. It has been shown in a few theoretical studies that it is possible to obtain higher quality factor resonance in metamaterials by introducing certain asymmetries into the SRR geometry [2-4]. Zheludev *et al.* [1] have experimentally demonstrated higher quality factor for metamaterials at microwave frequencies by using asymmetric split ring resonators.

Split Ring Resonators (SRRs) have been shown to produce a highly resonant electric field strength and modal intensity concentration near the ends of their arms [2-6]. The asymmetries between the two arms of the double SRR structures produce distinct plasmon resonances that are modified by the presence of the other arm, leading to a steep gradient of the reflection versus frequency curve between the resonances [1-3]. A shift in

a sharp feature is more easily identified than a rounded feature and therefore increases the sensitivity compared with similar but symmetric SRRs (S-SRRs).

The functioning of Asymmetric Split Ring Resonator (A-SRRs) with a circular basic geometry, operating at the mid-infrared frequencies is described in this chapter. The A-SRRs described here, possesses a higher quality factor for its plasmon resonance (a factor of two or more) than the plasmon resonance of its symmetric double or single split counterparts.

The A-SRRs described here, have a diameter of 1.2 µm, with a strip width of 100 nm, and are fabricated in thin gold films on fused silica substrates. The characteristic resonances of such structures are in the mid-infrared (typically at wavelengths in the 3 - 6 µm range). The main reason for choosing circular geometry for the A-SRRs over square geometries (U-shaped structures) is due to the relative ease of fabrication by which asymmetry could be introduced into circular structures. The main objective to fabricate such A-SRRs was for high sensitivity optical detection of organic and bio-chemical substances as described in the subsequent two chapters. Because of this, gold as a metal is chosen to form the A-SRRs due to its good resistance to oxidative corrosion when coming in contact with organic compounds. For the same reasons, fused silica is chosen for its inertness to most organic compounds.

## 4.2 Fabrication and measurement

The patterns are generated on fused silica substrates using electron-beam lithography (EBL) processes, with the addition of an aluminum charge dissipation layer deposited over the bi-layer of PMMA resist. After development, the pattern is subjected to electron-beam deposition of 2 nm of titanium for adhesion, then 48 nm of gold, followed by lift-off. The patterns are written over an area of ~300 x 300 $\mu m^2$. The reflection spectra of the fabricated structures have been measured at normal incidence with a Nicolet Continuum FTIR apparatus equipped with an Optical Microscope - using a 10 x magnification objective lens with an NA of 0.25. The FTIR beam was polarized using a Continuum ZnSe IR polarizer. An iris was used to restrict the incident light to a spot size area of nominally 200 µm x 200 $\mu m^2$. The reflectance measurements were taken with the incident light in one of two orthogonal polarizations - and were normalized, after each measurement, to the reflectivity of a gold mirror. Figure 4.1 shows a Scanning Electron Microscope (SEM) image of such a fabricated array of A-SRR patterns.

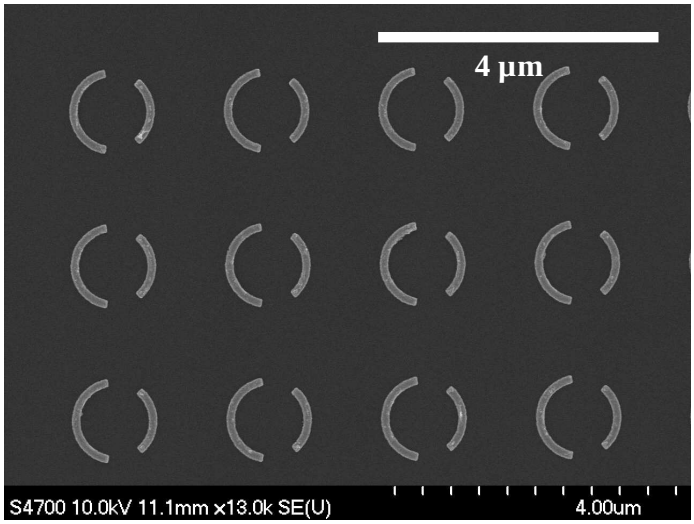


**Figure 4.1:** SEM micrograph of A-SRRs with diameter 1.2 µm and 100 nm strip width.

## 4.3 Modelling

Dr. Scott McMeekin of Glasgow Caledonian University modeled all the SRR structures described in this chapter. Modelling of the A-SRR structures was performed using the Fullwave FDTD simulation package from RSoft. A unit cell equal in dimensions to the period of the array of SRR structures, with periodic boundary conditions, was used to analyze the A-SRRs. The Drude model was used to describe the complex dielectric constant of the Au metal layer. The titanium adhesion layer was omitted from the simulation due to the increased computational time required to accommodate the specified grid size. The resonant response of the A-SRR structures as a function of wavelength was modelled, together with the spatial electric field distribution at the various resonant wavelengths.

## 4.4 Asymmetric split ring resonators (A-SRRs)

The unit cell of a single A-SRR, as shown in Figure 4.2, consists of two distinct and opposite single arcs separated by two identical narrow gaps. These two arcs (left-hand and right-hand) act as two separate resonators, with their individual resonant response depending on their respective lengths, as well as the angular gap between them. In this analysis the angular gap ($\theta$) is varied for the A-SRRs from ~ 15 to 55 degrees, in steps of 10 degrees, by keeping the length of the left-hand arc constant and shortening the length of the right-hand arc. All the other parameters are kept identical.

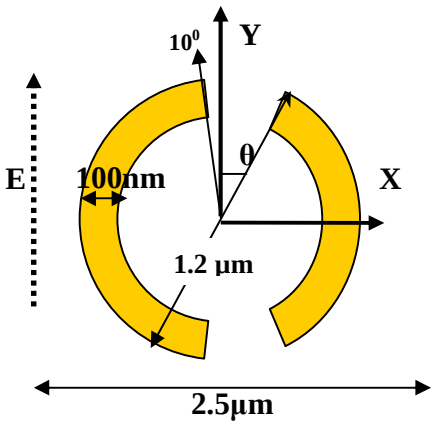


**Figure 4.2:** A single unit cell with optimized dimensions, showing the orientation of the E-field parallel to the Y axis. Measurements have been carried out at normal incidence.

Figure 4.3 depicts the resonant responses of arrays of symmetric single gap and double gap symmetric SRRs (S-SRRs) and asymmetric SRRs (A-SRRs) patterns obtained by measuring their corresponding reflectance spectra.

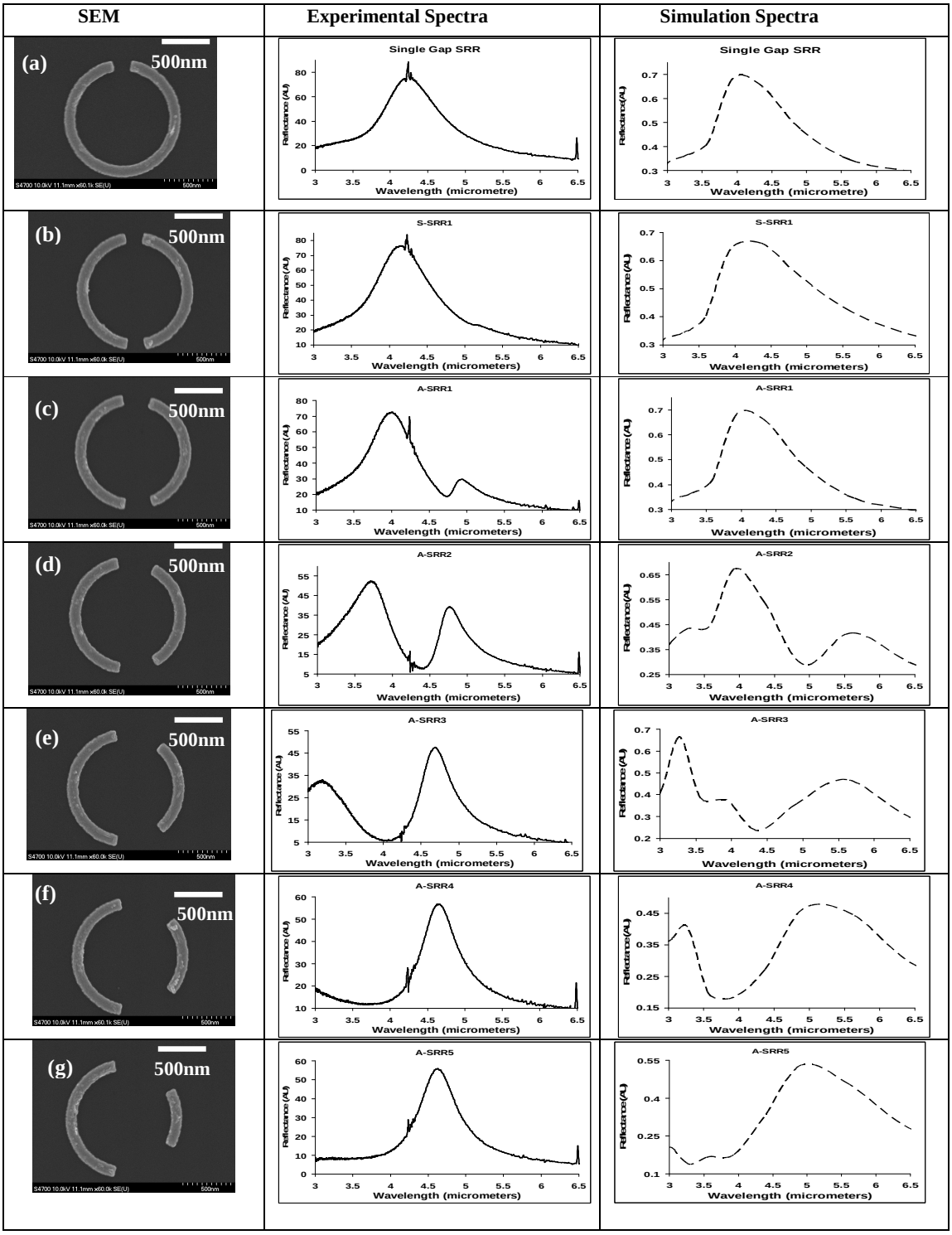


**Figure 4.3:** Table showing the reflectance spectra of the different SRR patterns. The first column shows SEM images of the (a) Single Gap SRR ($\theta \sim 10^0$) (b) S-SRR1 ($\theta \sim 10^0$)

(c) A-SRR1 ($\theta$~$15^0$) (d) A-SRR2 ($\theta$~$25^0$) (e) A-SRR3 ($\theta$~$35^0$) (f) A-SRR4 ($\theta$~$45^0$) (g) A-SRR5 ($\theta$~$55^0$) patterns. The second column of figures, with solid curves, shows the consequent experimental spectra – and the third column of figures, with dashed curves, show corresponding simulations. The spike present at a wavelength of 4.2 µm in all the experimental spectra indicates the presence of atmospheric carbon dioxide.

As seen from Figure 4.3 the experimental results are in good agreement with the simulated spectra. The discrepancy between the two sets of results could be attributed to the imperfection obtained during fabrication. In each case the measurements were made with light at normal incidence (i.e. the Z-direction) with the E-field maintained parallel to the Y direction. In the case of S-SRR1, the sizes of the left-hand and right-hand arcs are nominally identical (symmetric) - and their respective responses are superimposed, giving the overall resonance observed at 4.11 µm wavelength. This result has been confirmed by comparison with single arcs that have identical geometry i.e. the Single Gap SRR shown in Figure 4.3(a). From A-SRR1 onwards, the right-hand arc is shortened progressively by varying $\theta$. As the angular gaps between the arcs are varied, the two separate resonances of the left-hand and right-hand arcs are modified by the presence of the other arc. In the case of A-SRR1, the asymmetry in length between the left and right-hand arc is still small - and a steep edge emerges at 4.7 µm, separating the resonance, at 3.9 µm, of the shorter (right-hand) arc from the resonance at 4.9 µm for the longer (left-hand) arc. (Between the two resonances, the reflection dip can be identified as a trapped mode [1], - discussed later). In the cases of A-SRR2 and A-SRR3, as the asymmetry between the lengths of the left-hand and right-hand arcs is varied further, the individual resonances of the two arcs become more distinct - but, due to the proximity of the two arcs, the resonances observed

are shifted with respect to those exhibited by single arcs alone. This result has been confirmed by simulations of separate arcs, as shown in Figure 4.4 in which the individual peaks are closer together.

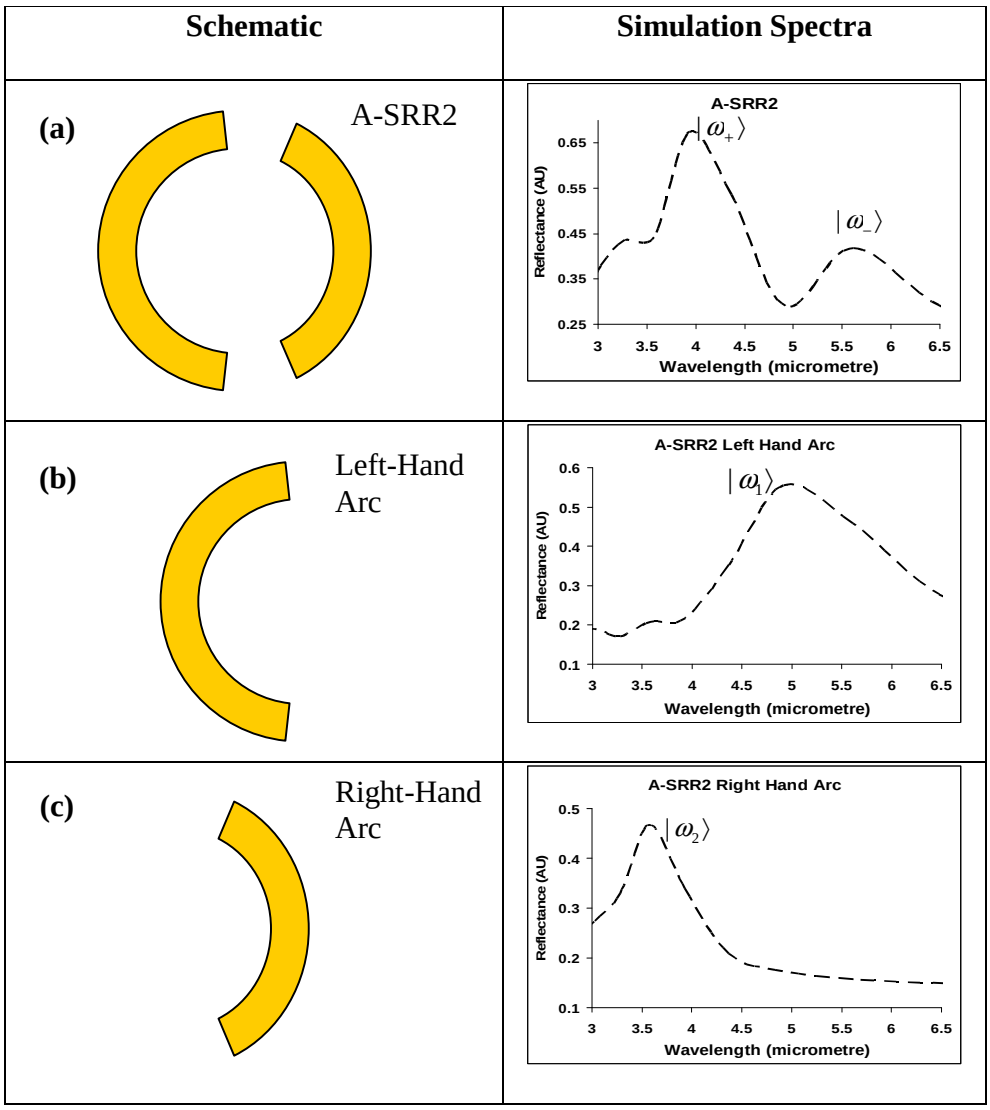


**Figure 4.4:** Schematic and simulation spectra of (a) A-SRR2 (b) Only the Left-Hand Arc of A-SRR2 and (c) Only the Right-Hand Arc of A-SRR2. The resonance peaks are denoted with plasmonic eigenmodes that are discussed below. The resonances exhibited by single, individual arcs are distinct but are shifted when both are positioned close to each other in an A-SRRs.

The results obtained here is very similar to the resonance hybridization model of double SRR (DSRR) structures presented by Giessen *et.al.* in references [7-8]. A similar resonance hybridization model is applied here with the Left-Hand Arc (longer arc) being excited by frequency $\omega_1$ (equivalent to wavelength 4.9 µm from Figure 4.4 b) that corresponds to the plasmonic eigenmode of $|\omega_1\rangle$. Similarly the Right-Hand Arc (shorter arc) is excited by frequency $\omega_2$ (equivalent to wavelength 3.49 µm from Figure 4.4 c) that corresponds to the eigenmode of $|\omega_2\rangle$. When both these arcs are positioned close to each other, their respective plasmonic eigenmodes interact with one another and create new coupled plasmonic eigenmodes due to resonance hybridization [7-9]. The new coupled plasmonic resonance modes are either at higher energies (shorter wavelengths) corresponding to the symmetric plasmonic mode of $|\omega_+\rangle$ (equivalent to wavelength 3.9 µm from Figure 4.4 a) or at lower energies (longer wavelengths) corresponding to the asymmetric plasmonic mode of $|\omega_-\rangle$ (equivalent to wavelength 5.6 µm from Figure 4.4 a) [7-8].

A plasmon resonance hybridization diagram, very similar to that of reference [7] is shown in Figure 4.5.

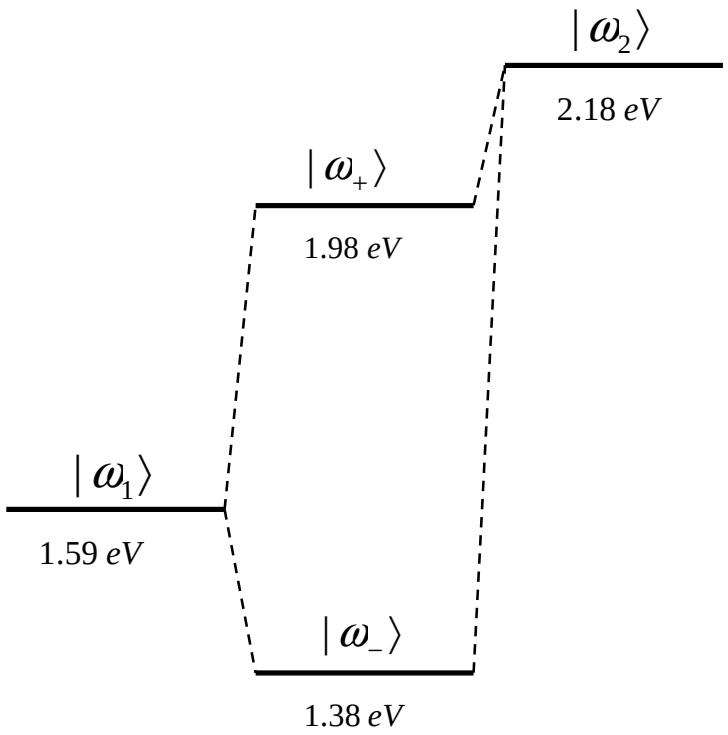


**Figure 4.5:** Resonance Hybridisation diagram corresponding to the plasmonic eigenmodes obtained from the simulation result of Figure 4.4.

As can be seen from both Figure 4.4 and 4.5 the corresponding symmetric and asymmetric resonances ( $|\omega_+\rangle$ and $|\omega_-\rangle$ ) are red-shifted (reduce in energy) compared to their individual single arc counterparts ($|\omega_2\rangle$ and $|\omega_1\rangle$). The red-shift is due to the interaction between the left-hand and right-hand arcs. When the A-SRR2 structure is excited by normal incidence, it induces simultaneous circulating electric currents inside both arcs, clockwise and anticlockwise with respect to each other. This results in the capacitive interaction between the arcs and the additional capacitance produces the resulting red-shift [7-8]. The schematic for the current direction inside A-SRR2 is shown in Figure 4.6.

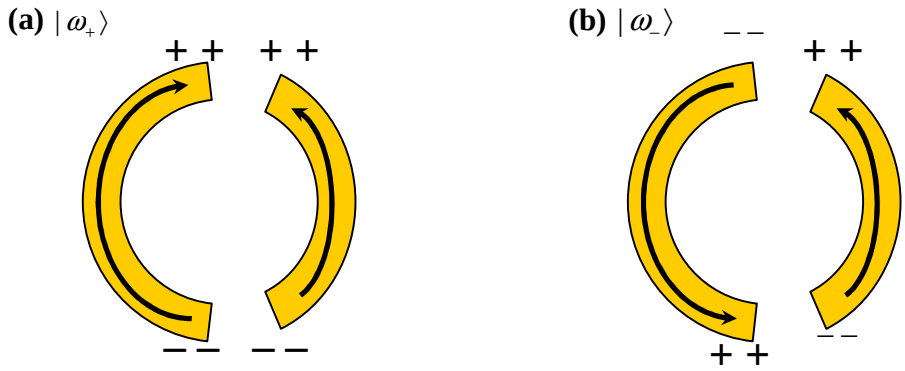


**Figure 4.6:** Sketch of electron current in the arcs of A-SRR2 with (a) being the symmetric mode of shorter wavelength resonance (higher energy) of $|\omega_{+}\rangle$ and (b) asymmetric mode of longer wavelength resonance (lower energy) of $|\omega_{-}\rangle$. The field plots of Figure 4.9 (a) and 4.9 (c) shown later in this chapter shows somewhat similar arrangement of optical electric fields.

From Figure 4.4 it can be seen that the linewidth of the asymmetric resonance $|\omega_{-}\rangle$ is smaller (narrower) than $|\omega_{1}\rangle$, but the linewidth of the symmetric resonance $|\omega_{+}\rangle$ is broader than $|\omega_{2}\rangle$. At the same time, the amplitude of resonance for the asymmetric resonance $|\omega_{-}\rangle$ is lower than $|\omega_{1}\rangle$, but the amplitude of resonance for the symmetric mode $|\omega_{+}\rangle$ is higher than $|\omega_{2}\rangle$. For the asymmetric mode, charges at the end of the arcs attract each other resulting in the reduction of charge oscillation. Therefore, the oscillation strength decreases resulting in the reduction of radiative losses. This makes the asymmetric resonance $|\omega_{-}\rangle$ having a narrow linewidth (low loss) and reduced amplitude of resonance (low oscillation).

For the symmetric mode of resonance $|\omega_{+}\rangle$, the charges at the end of the arcs repel each other, resulting in increase of charge oscillations. This increases the oscillation strength and adds to the radiative losses. This makes the amplitude of resonance for symmetric modes higher (more oscillation) and their linewidth broader (more loss) [7-8].

## 4.5 Trapped mode

A-SRR2 is marked by the steep edges that emerge in the reflection spectrum between the individual resonances of the left and right-hand arcs, with an increase in the quality factor from 4.7 for the symmetric case S-SRRs in Figure 4.3 (b) to 9.4 for the longer wavelength reflectance peak of A-SRR2 in Figure 4.3 (d). In the corresponding SRRs and other SRRs with dimensions that lead to resonances in the microwave spectral region [1], at normal incidence the electric field of the linearly polarized plane-wave excitation can excite a circulating current that has the same direction in each arc – and therefore coupling into and out of such structures is inherently weak – and is zero, in principle, for the exactly symmetric case. In the case of asymmetry between the lengths of the two arcs, the scattered electromagnetic radiation produced by the circulating current configuration is weak but finite, reducing the coupling of the resonant mode to free space and reducing the radiation losses. This behavior leads to the so–called trapped mode identified by Zheludev *et al.* [1]. When analyzing simulations of the transmission and reflection spectra, a substantial increase in the resonant absorption is observed at the minimum of the reflection dip corresponding to the trapped mode - and is consistent with energy being stored (and dissipated) in the coupled arcs. It is also noted that trapped mode can be excited into the single gap SRR as well as S-SRRs by using circularly polarised light,

which has not been used in this experiment. The corresponding experimental reflectance and transmission spectra for A-SRR2 are shown in Figure 4.7.

For A-SRR3, there is a further shift in the resonance of the right-hand arc to shorter wavelengths, due to further reduction in its length. In the case of A-SRR4, the gap is further increased by additional shortening of the right-hand arc - so the impact of the loading of the non-resonant arc section on the resonance becomes small. Similar behavior is seen in the case of A-SRR5, where the angular gap is even further increased - resulting in the disappearance of the resonance produced by the shorter (right-hand) arc from the measured spectral range, as it increasingly moves towards shorter wavelengths. It can also be seen that, since the length of the left-hand arc is always kept constant, the resonance position of the longer (left hand) arc does not vary appreciably (moving only from 4.9 µm to 4.6 µm). However, as the right-hand arc is shortened, it is found that the position of its resonance progressively moves towards shorter wavelengths (from 3.9 µm to 2.5 µm), changing the spectra of the coupled resonance. It can therefore be inferred that variation of the angular gap between the two arcs not only increases the quality factor of the resonance peaks in the overall response, but also that it tunes the position of the resonances. The spike present at a wavelength of 4.2 µm in all the experimental spectra indicates the presence of atmospheric carbon dioxide.

The experimental spectra of the S-SRR1 and the A-SRR2 are again shown in Figure 4.7 for direct comparison of their quality factor. The Quality factor (Q-Factor) of the resonance of Single Gap SRR and S-SRR1 of Figure 4.3 is calculated to be ~ 5, whereas the Q-Factor of the left-hand arc (longer wavelength resonance) of A-SRR2 is found to

be about ~ 10. It can therefore be seen that, by adding asymmetry to the structure of split ring resonators, it is possible to increase their overall quality factor of resonance. This sharper resonance can be exploited when shifting the position of the resonance by, for example, depositing external material on the surface to act as a sensor.

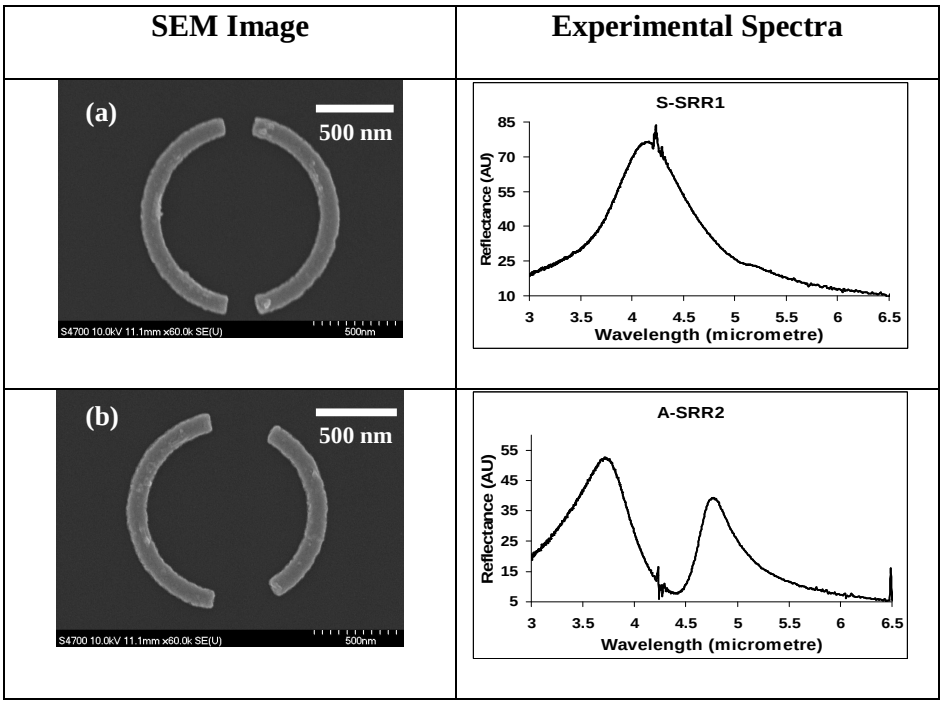


**Figure 4.7:** Experimental spectra of (a) symmetric S-SRR1 and (b) asymmetric A-SRR2. By adding asymmetry to the overall geometry of the SRRs, the quality factor of their resonant response can be increased.

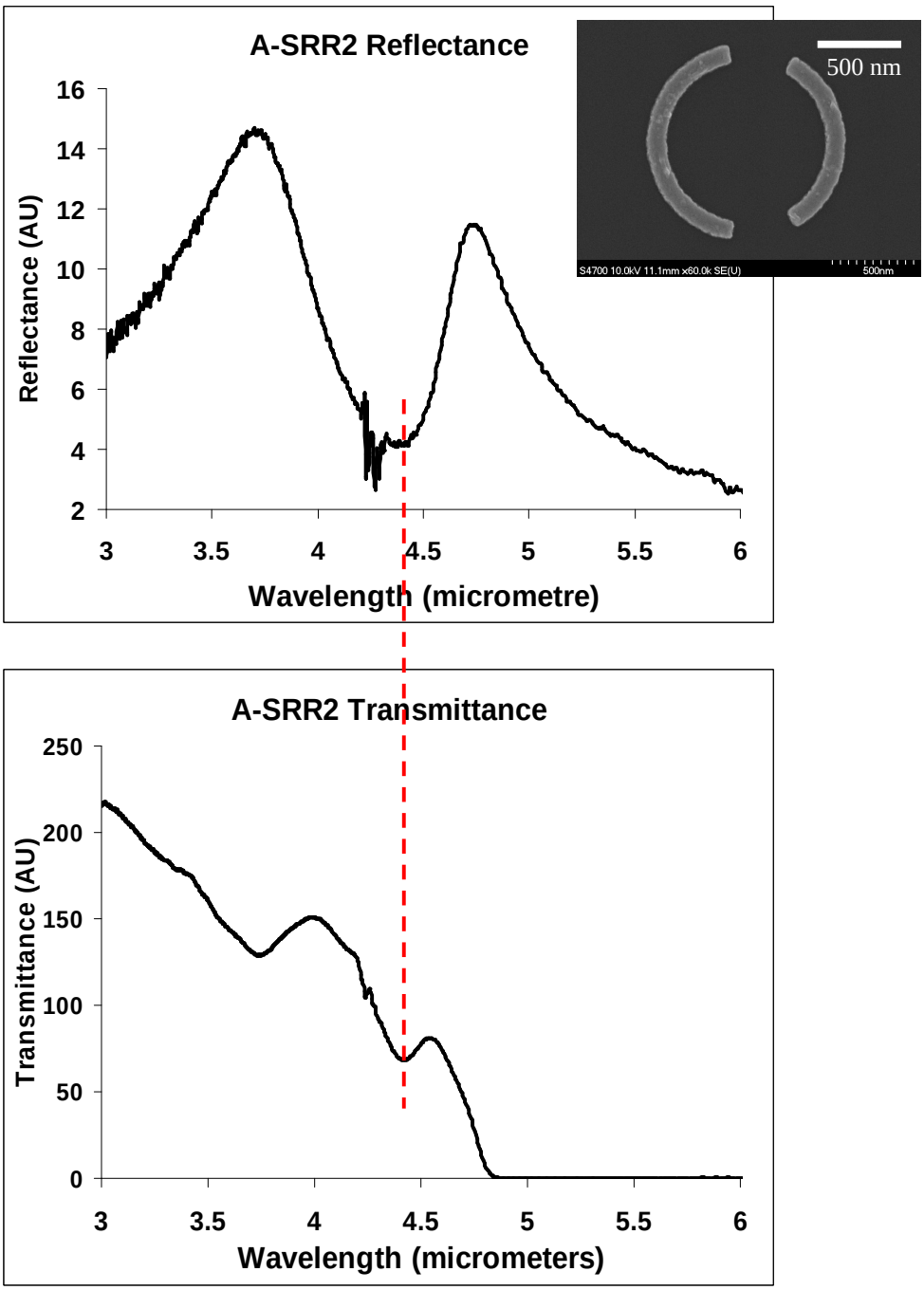


**Figure 4.8:** SEM image of A-SRR2 (inset) and its corresponding Experimental Reflectance and Transmittance Spectra. The trapped mode is located at 4.39 µm wavelength. The red dotted line is an aid to the eye.

From Figure 4.8, it can be seen that the trapped mode of A-SRR 2 located at 4.39 µm is associated with low reflectance and transmittance but a higher absorbance. From 4.8 µm onwards, the silica substrate becomes highly *absorbing* and hence there is zero transmission at wavelengths after it. Both the reflectance and transmittance measurements were normalized with respect to the same gold mirror to achieve similarity, but due to the poor transmission of gold mirror at these wavelengths, the magnitude of transmittance for A-SRR2 became large. However, it is understood that the position of the trapped mode (in both reflection and transmission) is more important than the respective magnitude of the individual spectra.

Figure 4.9 shows the experimental spectrum for A-SRR2 in terms of frequency response. This result is very much similar to that reported in [1], where a trapped mode resonant behavior was observed for structures with similar geometry at microwave frequencies – and also to the results for structures approximately a hundred times larger that have resonances in the low THz frequency region, as described in reference [3]. The Q-factor of the reflection dip of the trapped mode resonance is reduced from a figure of 20 in the microwave region, as reported in reference [1], down to an estimated value of 11.5, at the mid-infrared frequencies of the present work.

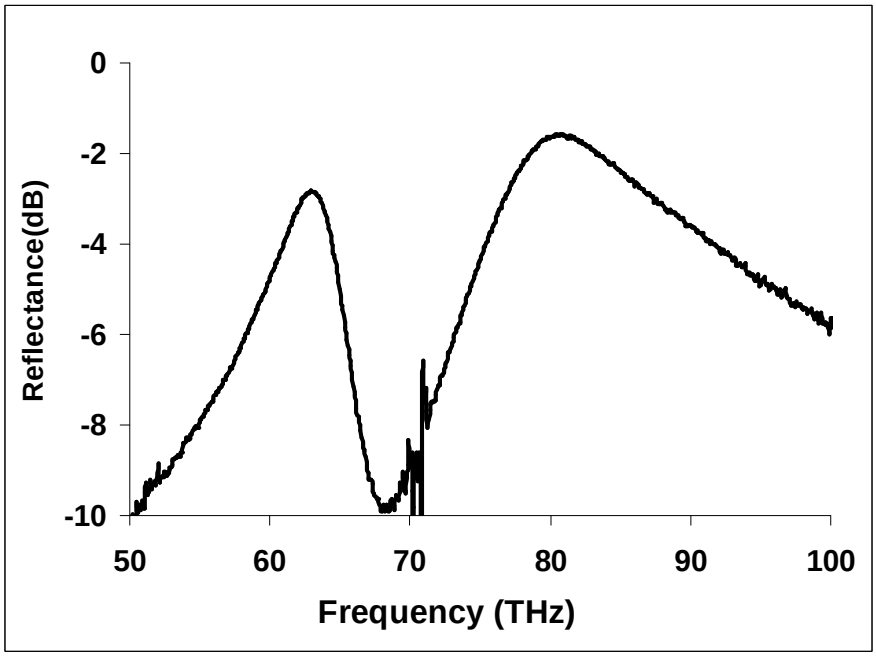


**Figure 4.9:** The experimental reflection spectrum of A-SRR2 plotted as a function of frequency. The trough obtained at 68 THz is similar to the trapped mode observed in the microwave frequency range in reference [1].

The field plot of the electric field strength at Y axis for the resonance peaks as well as the trapped mode of A-SRR2 is shown in Figure 4.10 (a)-(c).

(a) Electric filed strength at wavelength 3.9μm resonance peak

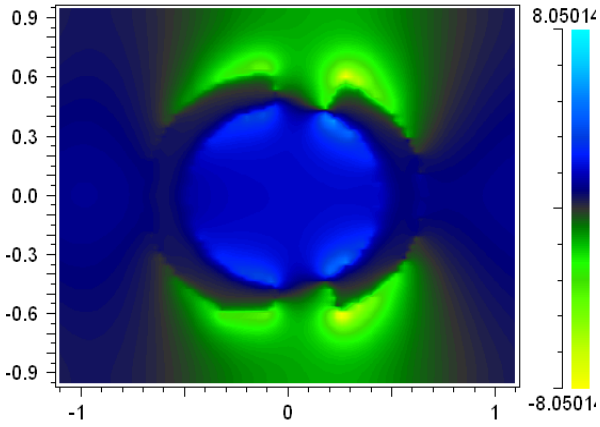


(b) Electric filed strength at wavelength 4.6 μm resonance dip (trapped mode)

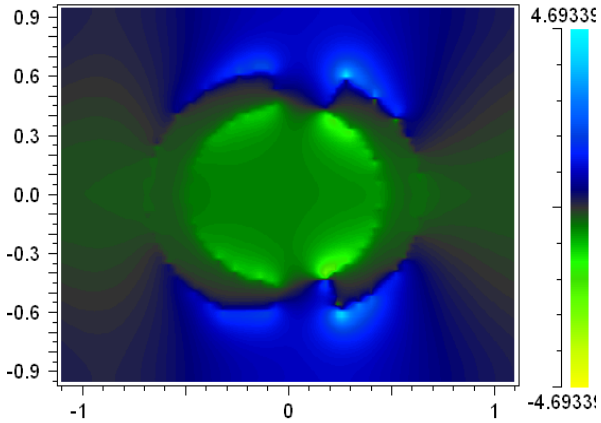


(c) Electric filed strength at wavelength 5.6 μm resonance peak

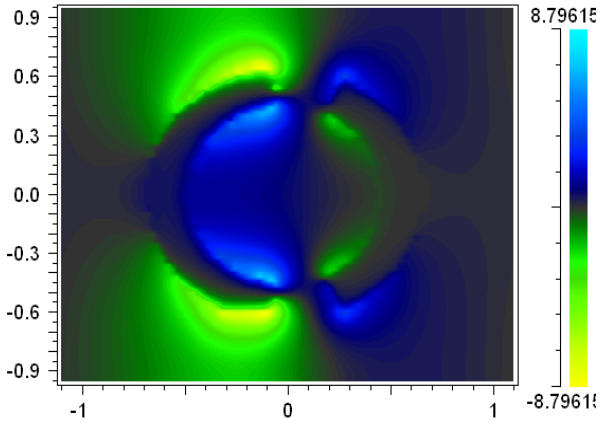


**Figure 4.10:** Electric field strength in the Y direction at different wavelengths corresponding to the peaks and troughs in the simulation of Figure 4.3(d).

The field plots in Figure 4.9 show the concentration of the electric field distribution towards the ends of the arcs at a wavelength of 3.9 µm for the smaller arc - and at a wavelength of 5.6 µm for the larger arc. These wavelengths correspond to the respective reflection peaks. The central plot, at a wavelength of 4.6 µm, corresponds to the reflectance dip of the trapped mode [1], for which the reflectance is sharply reduced and the field distribution in the two arcs is similar. Here there is no strong concentration of the field (corresponding to yellow) but an even spread around the two arcs. It is also recognized that pale blue corresponds to equally high field as yellow, but with opposite sign of the field. The field plot of Figure 4.9 (a) is that of the symmetric resonance mode $|\omega_{+}\rangle$ of shorter wavelength (higher energy) and it shows fields at the end of arcs with similar sign. Whereas, the field plot of Figure 4.9 (b), which is of the asymmetric resonance mode $|\omega_{-}\rangle$ of longer wavelength (lower energy) shows the fields at the end of arcs with reverse signs. This further corroborates the reasoning made in Figure 4.6. and the subsequent explanation.

Therefore, based on the field plots of Figure 4.10, it could be stated that the end of the arms of the A-SRRs as well as near the centre of the A-SRR at trapped mode forms the hot-spots of the A-SRR where the optical electric field is concentrated. Field enhancement factors associated with the edges of nanorings have been previously reported for the near infrared and visible region of the spectrum [5]. In has been shown by Papasimakis *et al.* [10] that A-SRRs could be considered as coherent metamaterials and their characteristic trapped mode disappears by increasing the disorder in the array. It is explained that by increasing the disorder into the A-SRR array, results in intense

scattering and thus reduction in strength of the circulating currents of the arcs. This increases the losses resulting in reduction and finally disappearance of A-SRR characteristic. The impact of periodicity and disorder on the overall resonance characteristic of A-SRRs has not been considered in this chapter but is subject to future works as described in Chapter 7 of this thesis.

## 4.6 Conclusions

In this chapter, similar behavior has been demonstrated in asymmetric circular split ring resonators at size scales that are respectively two and four orders of magnitude smaller than those used in previous studies. While, the Q-factor of A-SRR is reduced from 20 in the microwave range to 11 in the present work, but is a factor of two more than the currently used symmetric split ring resonator in these wavelength ranges. This property of A-SRRs is utlised in the next chapter for high sensitivity detection of very thin films of organic materials.

### Acknowledgement

The author wishes to express his gratitude to Dr. Scott McMeekin of Glasgow Caledonian University for the carrying out the modelling of all the fabricated structures shown in this chapter and for discussions regarding the analysis of the results.

# References

1. V. A. Fedetov, M. Rose, S. L. Prosvirnin, N. Papasimakis and N. I. Zheludev, “Sharp Trapped-Mode Resonances in Planar Metamaterials with a Broken Structural Symmetry,” Phys. Rev. Lett. 99, 147401 1-4 (2007).

2. C. Debus and P. H. Bolivar, “Frequency selective surfaces for high sensitivity terahertz sensing,” Appl. Phys. Lett. 91, 184102 1-3 (2007).

3. C. Debus and P. H. Bolivar, “Terahertz biosensors based on double split ring arrays,” Proc. SPIE. 6987, 6987(OU), 3-8 (2008).

4. S. Prosvirnin and S. Zouhdi, *Advances in Electro-magnetics of Complex Media and Metamaterials* (Kluwer Academic Publishers Netherlands) 281-290 (2003).

5. E.M. Larsson, J. Alegret, M. Kall and D. S. Sutherland, “Sensing Characteristics of NIR Localized Surface Plasmon Resonance in Gold Nanorings for Application as Ultrasensetive Biosensors,” Nano Lett. 7, 1256 (2007).

6. E. Cubukcu, S. Zhang, Y-S. Park, G. Bartal and X. Zhang, “Split ring resonator sensors for infrared detection of single molecular monolayers,” Appl. Phys. Lett. 95, 043113 1-3 (2009).

7. H. Guo, N. Liu, L. Fu, T. P. Meyrath, T. Zentgraf, H. Schweizer and H. Giessen, “Resonance hybridization in double split-ring resonator metamaterials,” Opt. Exprss. 15, 19, 12095-12101 (2007).

8. N. Liu, H. Guo, L. Fu, H. Schweizer, S. Kaiser and H. Giessen, “Electromagnetic resonances in single and double split-ring resonator metamaterials in the near infrared spectral region,” Phys. Stat. Sol. (b) 244, 4, 1251–1255 (2007).

9. E. Prodan, C. Radloff, N. J. Halas, P. Nordlander, “A Hybridization Model for the Plasmon Response of Complex Nanostructures,” Science, 302, 419-422 (2003).

10. N. Papasimakis, V. A. Fedotov, Y. H. Fu, D. P. Tsai and N. I. Zheludev, “Coherent and incoherent metamaterials and order-disorder transitions,” Phys. Rev.B, 80, 041102 1-4 (2009).

# Chapter 5

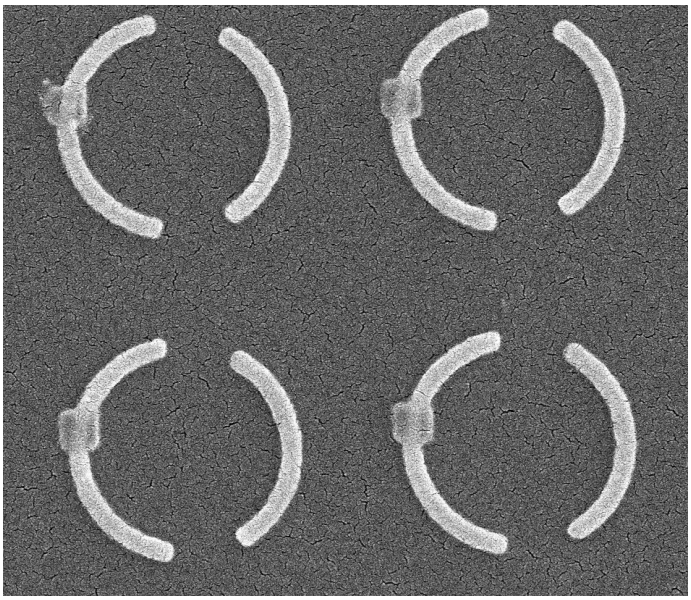

# Optical sensing of thin film organic materials using asymmetric split ring resonators (A-SRRs)

In continuation from the previous chapter about Asymmetric split ring resonators (A-SRRs), in this chapter the properties of A-SRRs are utilised to detect the presence of very thin layers of poly-methyl-methacrylate (PMMA), a commonly used positive electron-beam resist. Many organic substances display spectral resonances in the mid-infrared range. In this chapter the resonance of A-SRRs are tuned to match the molecular resonances of PMMA to obtain its characteristic signature for the process of detection. Finally, localised blocks of PMMA at specific hot-spots of the A-SRRs are deposited to demonstrate enhanced optical sensing capabilities.

## 5.1 Introduction

Optical Sensing and identification of thin film organic substances are at present subjects of active research due to their huge potential in commercial applications [1-7]. It is possible to identify an organic substance by detecting the phonon resonance or resonant absorption of the molecular compound from its complex dielectric properties, using various optical methods [1-7]. Sensitive and accurate detection of minute amounts of organic compounds are required for a number of purposes - such as forensic and security analysis and immunosensing [7]. High sensitivity optical resonators such as Asymmetric Split Ring Resonators (A-SRRs) resonating in the infrared region can modify their responses with respect to a change in the overall dielectric environment [1, 8]. The modification of the resonant response of A-SRRs is a function of the dielectric characteristics and hence could be utilised in their accurate detection.

By using A-SRRs that resonate in the infrared region of the electromagnetic spectrum, a number of advantages are obtained. Firstly, the asymmetry in the A-SRR type split-ring resonators produces steeper responses than obtainable in their symmetric counterparts - and hence they are more sensitive to a thin film or partial thin film deposition on their surface [8]. Secondly, by matching the responses of A-SRRs with the targeted molecular resonance of an organic compound, a characteristic signature of that molecule is obtained [8]. Thirdly, A-SRRs exhibit a resonant mode, the so called trapped mode, where the optical electric field is distributed inside the A-SRRs. By localizing the organic material at these specific spots, further enhancement in signal could be obtained [8]. The resonant frequency of A-SRRs scales inversely with size [1-3, 8]. As described in reference [1],

these arrays of A-SRRs with circular geometries act as passive frequency selective surfaces (FSS) at infrared frequencies. The A-SRRs are fabricated on thin gold films on fused silica substrates. The diameter of the A-SRRs was varied from 1.35µm to 1.55 µm to match the molecular resonance of the organic compound, whilst the strip width was kept constant at 100 nm in each case. The experimental results for optical detection of very thin film of PMMA is described below

## 5.2 Detection of thin layers of PMMA

Many organic compounds contain molecular bonds that exhibit spectral resonances in the mid-infrared range (typically in the 3-5 µm wavelength range) [9]. This property has provided the main motivation, for tuning the resonant response of the A-SRRs to mid infrared wavelengths. In order to test the sensitivity of the A-SRRs, the fabricated structures were coated with thin films of poly-methyl-methacrylate (PMMA), a commonly used positive electron-beam resist. The choice of PMMA was because of the accurate control of the thickness obtainable via control of the spin speed used when coating the sample. The refractive index of PMMA at mid infrared wavelengths was found to be 1.49 [10]. A strong resonant feature at a wavelength of around 5.7 µm due to absorption by the carbonyl bond of PMMA [10-11] was observed. The use of PMMA as probe material for modifying the plasmonic behavior has been described in reference [6]. Similar observation of enhanced infra-red detection of another organic molecule (ODT) is described in reference [4]. In experiments described here, different concentrations of PMMA with molecular weights in the $80\text{-}100\times10^3$ range and around $350\times10^3$, dissolved in o-xylene, were spun onto the A-SRR array at different speeds to give uniform

thicknesses over the frequency-selective surface (FSS) pattern. The PMMA thickness was varied from 215 nm down to 30 nm, in order to test how effectively the A-SRRs were able to detect its presence. Figure 5.1 shows the shift (experimental and simulation) in the overall resonant response of the A-SRRs obtained by loading the FSS pattern with 110 nm of PMMA. In the case of the Symmetric split ring resonator (S-SRR1) array, the overall shift due to the loading by the PMMA was less (typically around 0.34 µm in the case of a 110 nm thick PMMA layer). In the case of the asymmetric split ring resonator (A-SRR2), where the two individual resonance peaks become clearly distinct, the shift observed in the position of the resonance was larger (typically around 0.51 µm for a 110 nm thick PMMA layer).

Simulations using a 110 nm dielectric layer of refractive index of ~1.49 show a more significant broadening of the peaks compared to the experimental results. The models of the refractive index dose not include the molecular absorption resonance or any wavelength dependence of the PMMA.

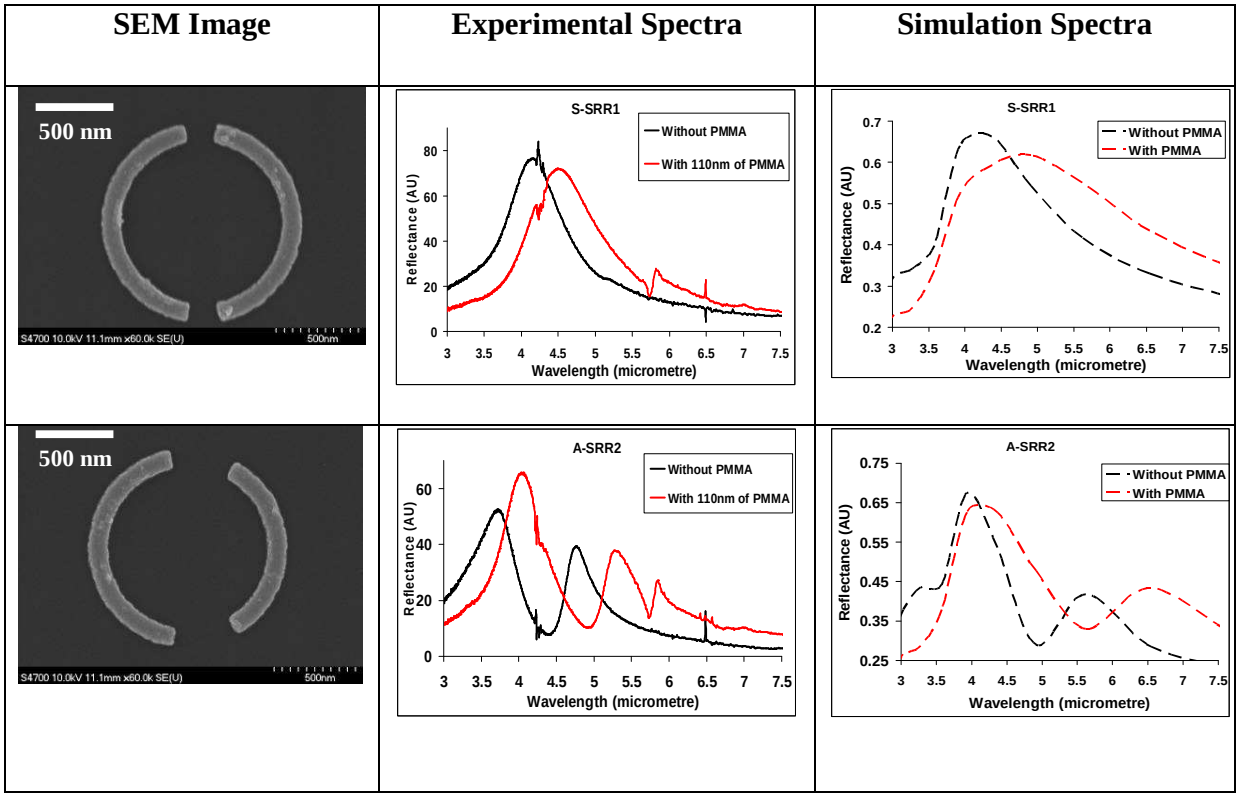


**Figure 5.1:** Table depicting the shift in the position of the resonance produced by loading the S-SRR1 and A-SRR2 array with a 110 nm thick layer of PMMA. The first row with solid lines depicts the experimental results. The second row, with dashed lines in the figures, depicts the corresponding simulations. The black curves show the original resonance without PMMA and the red curves show the resonance with 110nm of PMMA deposited on top. The spike present at a wavelength of 4.2 µm in all the experimental spectra indicates the presence of atmospheric carbon dioxide.

In Figure 5.2 the overall shift in the position of the resonances as a function of the thickness of the PMMA layer is shown. Figure 5.2 show that A-SRR2 can register the presence of very thin layers of PMMA - as low as ~30 nm, which produces a shift in the resonance of 120 nm.

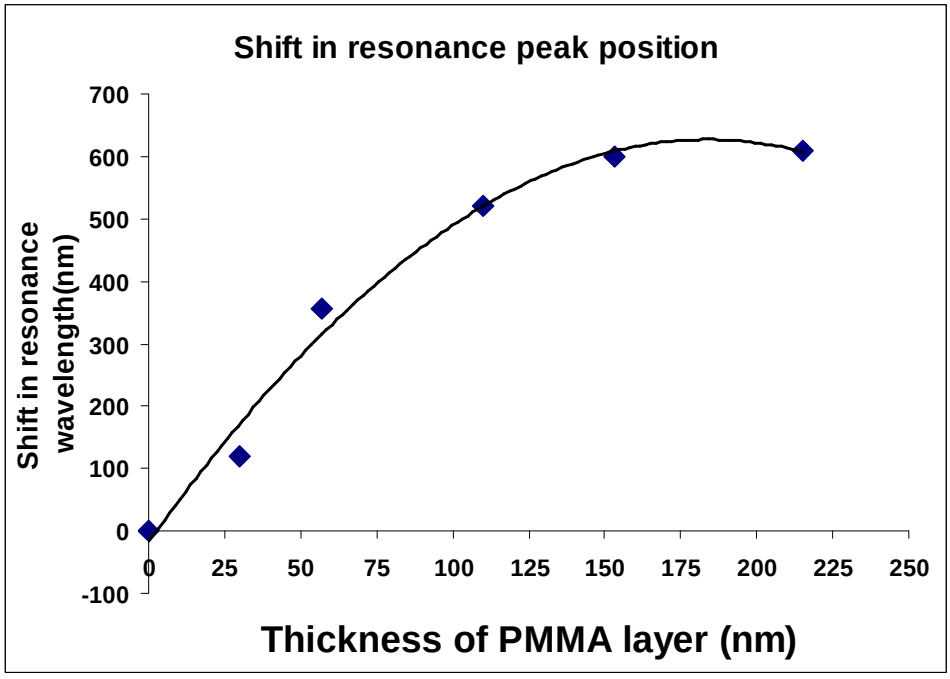


**Figure 5.2:** Showing the shift in the position of the A-SRR2 longer wavelength resonance as a function of the thickness of the PMMA layer (the solid line is a guide to the eye).

As the thickness of the PMMA increases, the shift in the peak position saturates, which can be attributed to the penetration of the propagating plasmonic mode beyond the PMMA layer becoming negligible. The sensitivity (*s*) of the A-SRRs towards PMMA is given as [12]

$$s = \frac{\Delta\lambda}{\Delta n}\, nm / RIU$$

Where $\Delta\lambda$ is the shift in resonance wavelength and $\Delta n$ is the change in the overall refractive index. The unit of the sensitivity (s) is given as nanometers (nm) per Refractive Index Unit (RIU).

From Figure 5.2 it can be seen that a 215 nm thick PMMA layer shifts the resonance wavelength by 605 nm. A 215 nm thick PMMA layer covers all of the 50 nm thick A-SRR and much above it. Assuming that it replaces all the air above the A-SRR (i.e. the 215 nm thick PMMA layer acts effectively as of infinite thickness above the A-SRRs), the change in refractive index is obtained as 1.49-1.

Therefore, the sensitivity of the A-SRR for 215 nm thick PMMA becomes

$$s = \frac{605}{1.49 - 1} = 1234.69\ nm / RIU$$

Thus, the sensitivity of an A-SRRs for ~200 nm thick PMMA layer is 1234.69 nm/RIU which is a factor of 2.5 times more sensitive from its nearest equivalent photonic crystal resonator utilizing similar techniques with ethanol as described in reference [12].

In order to detect the presence of small amounts of specific biological material - e.g. a particular DNA fragment [1-2], complementary receptors would need to be attached to the A-SRRs and, ideally, located near the ends where the electric field strength is greatest, or possible centre to access the trapped mode of the A-SRR. This has been discussed in the next chapter. By interpolation of the data in Figure 5.2, it can be seen that a 5 nm uniform layer of PMMA would still produce a readily observable shift in the resonance peak position of around 25 nm – and, if the layer were localised at the end of arms or near the centre of the A-SRRs, the sensitivity should be significantly further increased.

## 5.3 Matching the PMMA molecular resonance with the A-SRR resonance

Poly-methyl-methacrylate (PMMA) exhibits a very strong spectral resonance at about 5.7 µm wavelength in the mid-infrared. This is due to the C=O stretching band of unconjugated ester i.e. the free carbonyl bond [10-11] - and it is the strongest feature observable whilst taking FTIR spectra of thin film PMMA deposited over fused silica substrates. Figure 5.3 shows the FTIR spectrum for a 110 nm PMMA film deposited over silica substrate.

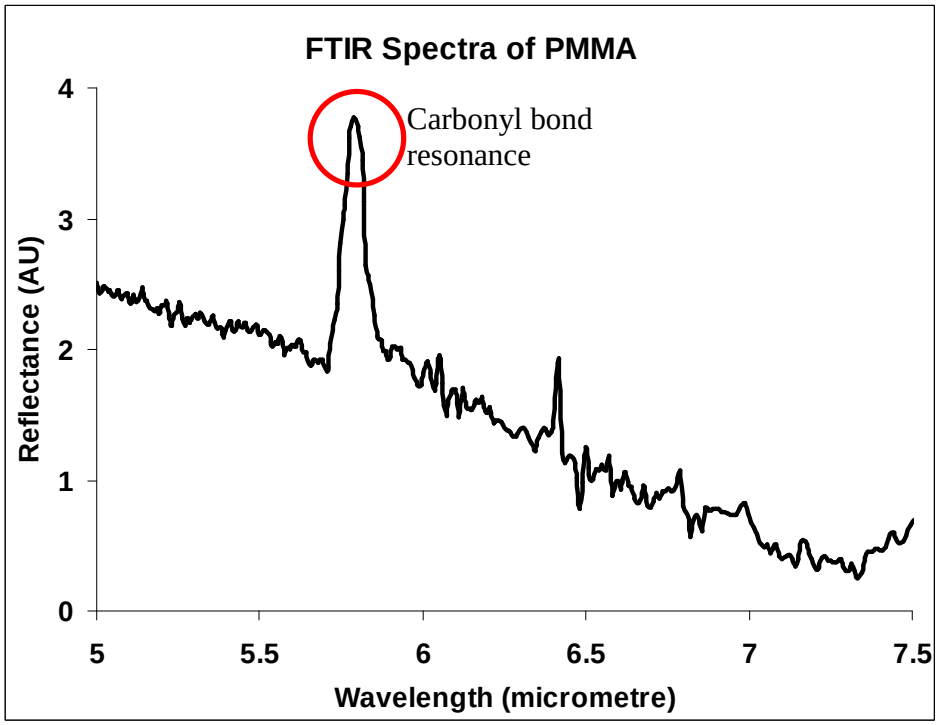


**Figure 5.3:** FTIR spectrum of 110 nm thin PMMA layer deposited over silica substrate. The spectral resonance present at 5.7 µm is due to the presence of carbonyl bond.

In this section and onwards, the thickness of the PMMA layer is kept constant at 110 nm in all cases. By changing the length of A-SRRs it is possible to match the various resonances of its arcs to the molecular resonance of the carbonyl bond of PMMA. This results in the formation of sharpened spectral features and enhancement in sensitivity. By changing the overall size of ASRR-2 from the previous value of 1.2 µm to the larger diameter of 1.35 µm - and later to 1.55 µm diameter - it was possible to match the longer wavelength resonance of the arcs with the strong molecular resonance due to the carbonyl group of PMMA. For A-SRRs with a diameter of 1.35 µm, the shoulder of the resonance of the longer arc (right-hand arc) matches that of the molecular vibration resonance of the carbonyl bond and enhances the signal. When the diameter of the A-SRRs is changed to 1.55 µm, the resonance peak of the A-SRRs matches the carbonyl bond resonance of PMMA, which results in further sharpening of the molecular resonance and enhancement in the signal. Figure 5.4 (a) and (b) depicts such behaviour.

From Figure 5.4 it can be seen that when the different resonance modes of the A-SRR matches with the PMMA carbonyl bond molecular resonance i.e. in case of A-SRR of diameter 1.55 µm - a very steep response to PMMA sensitivity is obtained that enhances the carbonyl bond resonance significantly, when compared with bare PMMA deposited over silica substrates of Figure 5.3. Further enhancement could be obtained by, localising the PMMA at specific A-SRR hot-spots like near the arms or the centre where the optical electric field is concentrated as shown in the field plots of Figure 4.10 of the previous chapter.

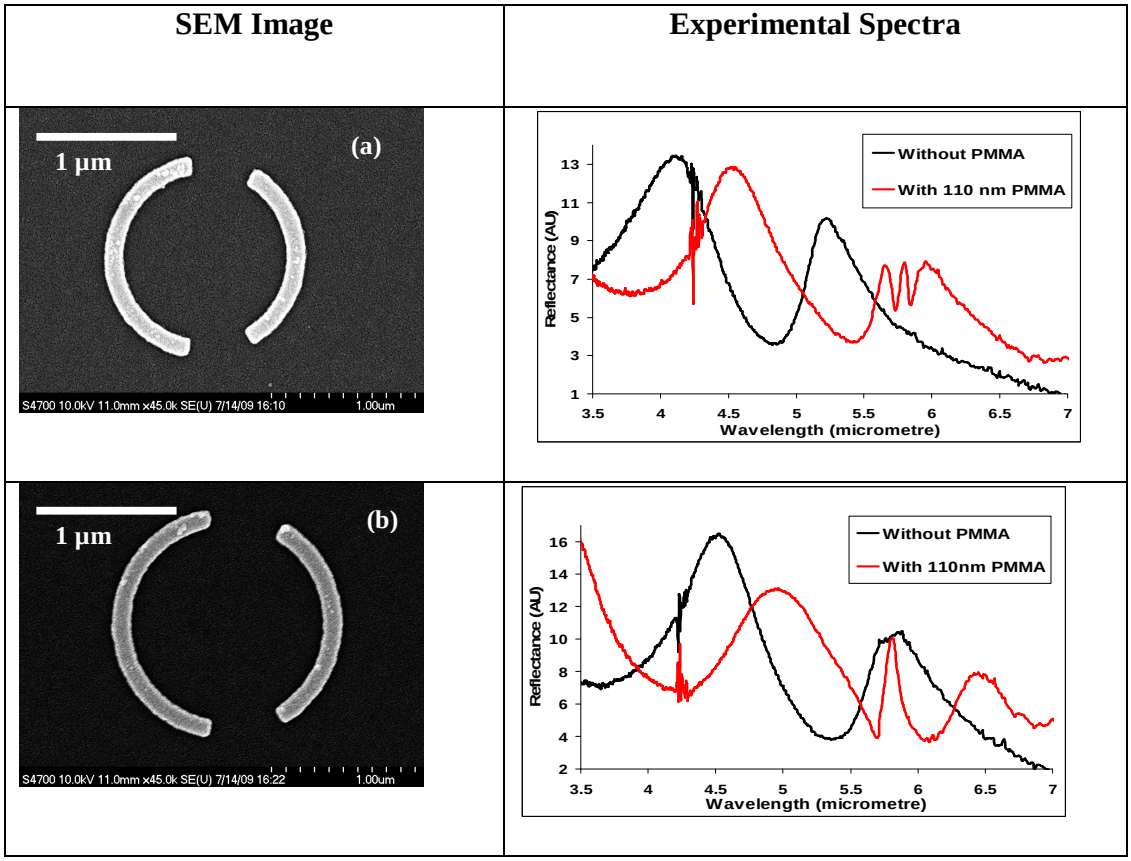


**Figure 5.4:** Increase in the sensitivity of PMMA obtained by matching the resonances of A-SRRs with its carbonyl bond resonance - with (a) A-SRR of diameter 1.35 µm and (b) A-SRR of diameter 1.55 µm. The black curve shows the original resonance without the PMMA - and the red curve shows the shifted resonance with 110 nm of PMMA deposited on top.

## 5.4 Fabrication for localisation of PMMA at A-SRR hot-spots

The fabricated patterns were generated on fused silica substrates using electron-beam lithography (EBL), with a charge dissipation layer of aluminium deposited on top of the electron-beam resist layer, each time that it is subject to electron beam (e-beam) writing. At first the markers are defined using e-beam exposure and developed and then subjected to an electron-beam deposition of 50 nm nichrome and 150 nm gold, followed by lift-off. After the markers are defined in this way, the substrate is again coated with resist and again subjected to another set of e-beam exposure for aligning and defining the A-SRR structures between the markers. After development, a further electron beam deposition of 2 nm of titanium and 48 nm of gold, followed by another lift-off process is required. After the A-SRRs are clearly defined within the markers, a very thin layer of PMMA of thickness around 110 nm is deposited over them using selective spinning - and is then again subjected to selective e-beam exposure, followed by development to localise the PMMA at specific positions on the A-SRR arrays using alignment techniques. At the end of the process, square blocks of PMMA with an area of ~200 nm X 200 nm - and thickness 110 nm - remain at specific positions of the A-SRR array. Figure 5.5 describes the whole process of fabrication in detail. All the A-SRRs discussed in this section and onwards have a diameter of 1.55 µm.

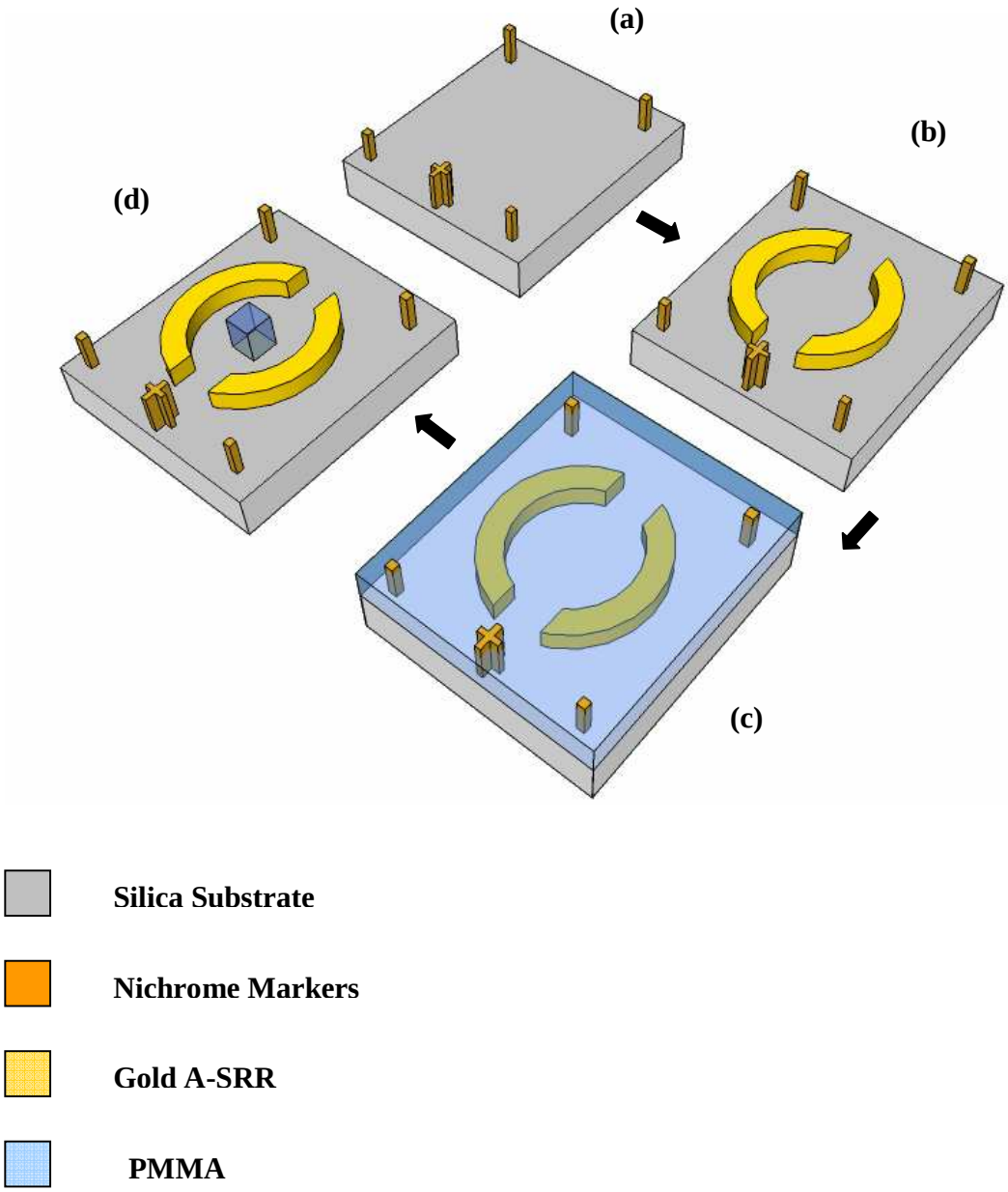


**Figure 5.5:** Fabrication and Localization of PMMA at specific spots of A-SRRs (a) Creation of Markers by EBL; (b) Alignment of A-SRRs inside the markers; (c) Spinning of PMMA of selective thickness over the A-SRRs; (d) Localisation of PMMA at specific points of the A-SRRs.

## 5.5 Localisation of PMMA at A-SRR Hot Spots

By localising the PMMA to specific hot spots (near the ends of arms or at the centre) of the A-SRRs (diameter 1.55 µm) it is possible to further enhance the signals. Attempts to localise square blocks of PMMA at different positions of supposed hot-spots for electromagnetic activity in A-SRRs are shown in Figures 5.6 to 5.8.

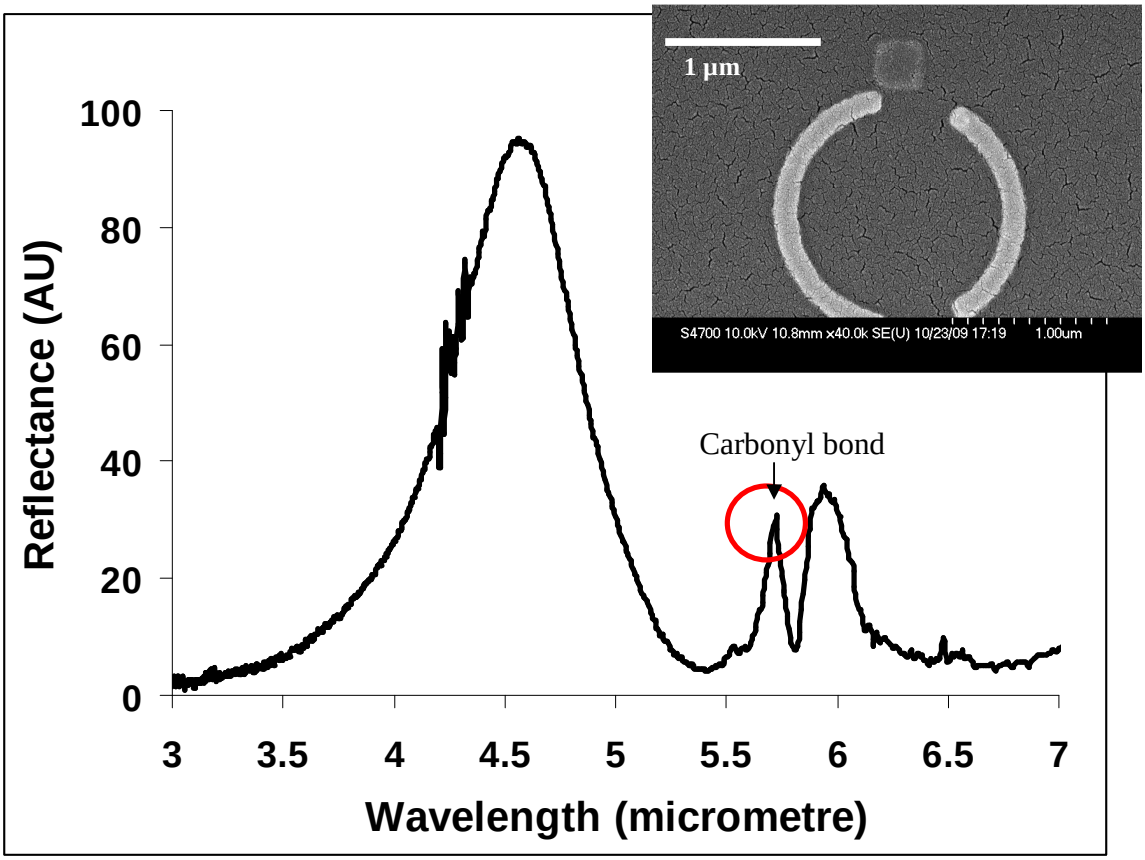


**Figure 5.6:** SEM image of rectangular block of PMMA of thickness 110 nm localised near the arm of A-SRRs (inset) along with its corresponding experimental reflectance spectra. The longer wavelength resonance mode of the A-SRR is somewhat matched with the carbonyl bond resonance of PMMA that result in producing a very steep resonance for the carbonyl bond.

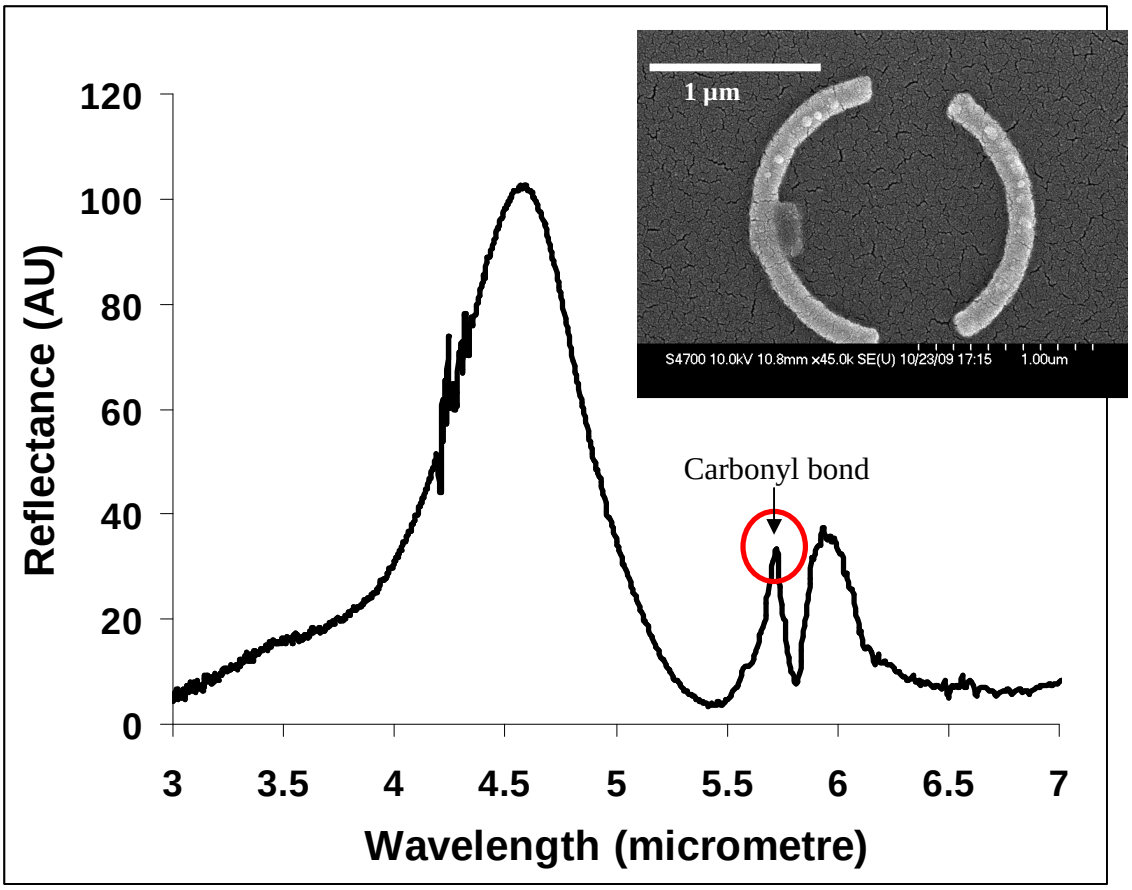


**Figure 5.7:** SEM image of square block of PMMA of thickness 110 nm localised at the centre of the right-hand arc of A-SRRs (inset) along with its corresponding experimental reflectance spectra. The longer wavelength resonance mode of the A-SRR is again somewhat matched with the carbonyl bond resonance of PMMA which result in steepening of the carbonyl bond resonance.

From Figures 5.6 and 5.7 it can be seen that by putting PMMA selectively at certain spots of A-SRR, instead of loading the whole FSS structure, the carbonyl bond molecular resonance of the PMMA becomes more enhanced (increase in amplitude) and more steeper (increase in quality factor). In order to bring out the other weaker molecular resonances of PMMA, it is necessary to localise the PMMA at the centre of the A-SRR

where the optical electric field concentration is not at a maximum but where multiple oscillations of the field during the trapped mode excites all the weaker resonances. It is shown in Figure 5.8.

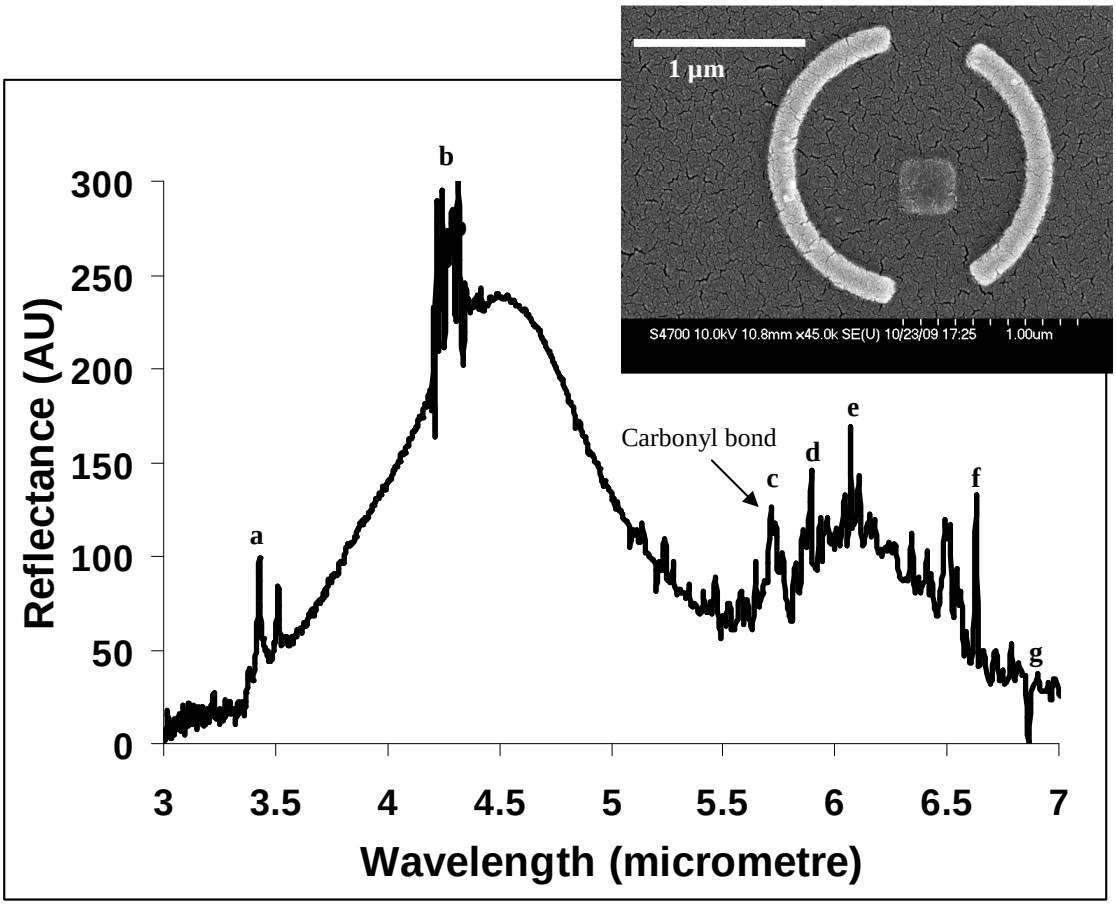


**Figure 5.8:** SEM image of square block of PMMA of thickness 110 nm localised near the centre of the A-SRRs (inset) along with its corresponding experimental reflectance spectra. Localising the PMMA block near the centre of the A-SRR produces an increase in its effective coupling with the trapped resonance mode of the A-SRRs, resulting in emergence of previously unnoticed weaker resonances. The various peaks obtained here (a-g) are identified and assigned in Table 5.1.

The difference between placing the PMMA block near the end of the arms of the A-SRRs and inside the middle of the A-SRRs is better illustrated in Figure 5.9 where a close-up of the spectra is taken with baseline correction.

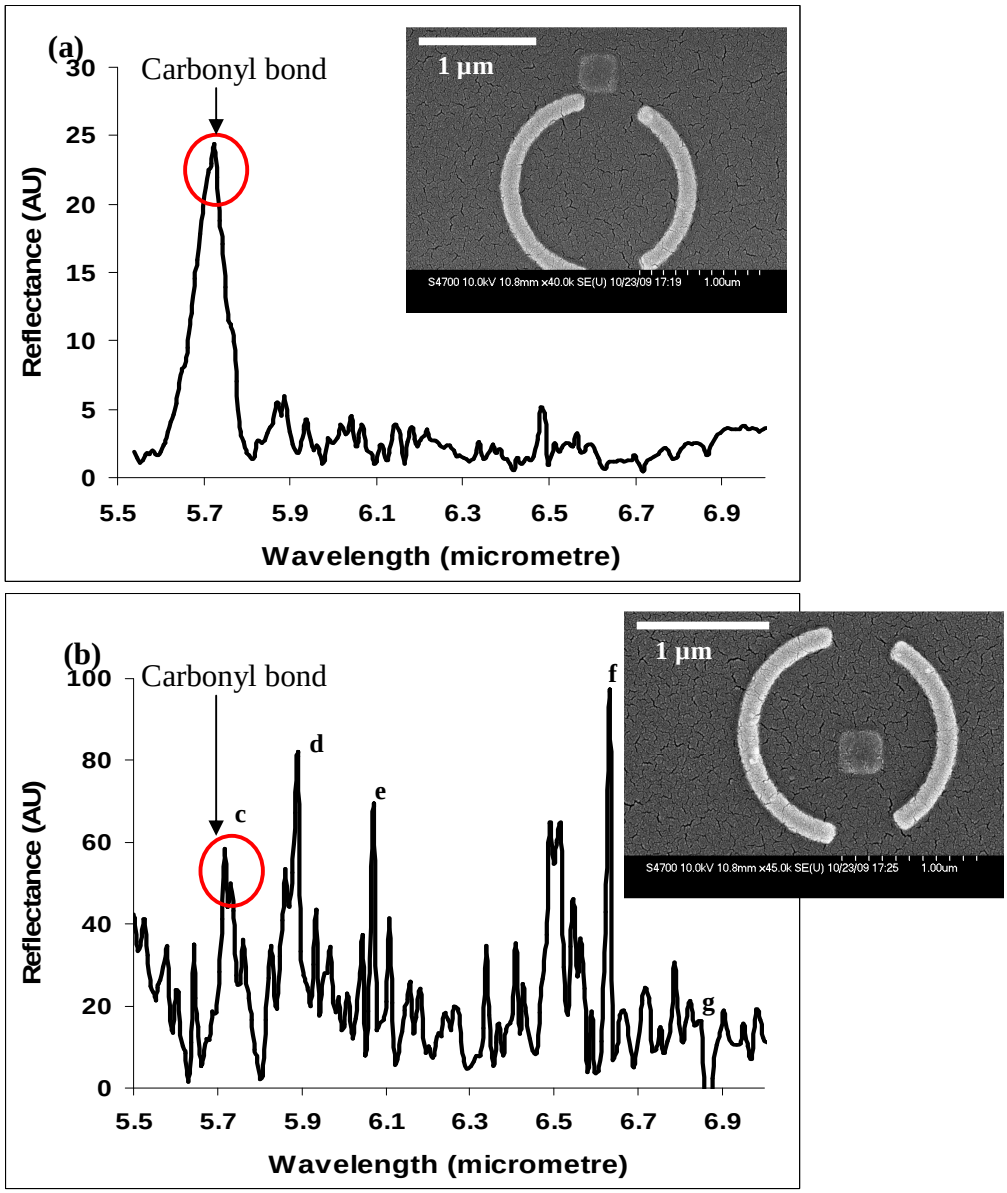


**Figure 5.9:** Comparison between the spectra obtained with (a) PMMA block localised near the end of A-SRR and (b) PMMA block localised at the middle of the A-SRRs. The encircled peak in both spectra is the carbonyl bond resonance. The various peaks obtained here (c-g) are same as in Figure 5.8 and are identified and assigned in Table 5.1.

As shown in Figure 5.9, by placing the PMMA block near the end of the A-SRR arc, only the strongest molecular feature (carbonyl bond resonance at 5.71 µm) is excited. However, by placing a similar PMMA block at the centre of the A-SRR, all the molecular resonances of the PMMA (weak and strong) are excited due to the multiple oscillations of the trapped mode. This results in the strongest molecular feature being reduced to a similar level as the other weaker resonances that have been enhanced. This effectively trade-off the stronger single feature for multiple excitation of the weaker features. No direct comparison between the intensity of spectra is implied as he FTIR software used to measure these spectra automatically performs scaling. In the case of Figure 5.8 it is evident from the apparent enhancement of the carbon dioxide spike present in 4.2 µm wavelength when compared with the same $CO_2$ spike at 4.2 µm of Figure 5.7.

It has been confirmed by simulations that by placing a block of material of size similar to that of the PMMA utilised here, with refractive index of 1.49, without a molecular absorption resonance or wavelength dependence, that the overall spectra *does not* change as much as the experimental results. This implies that the emergence of weaker molecular resonance features of PMMA and the enhancement of the strongest feature (carbonyl bond), by placing the PMMA block near the centre of the A-SRRs is primarily due to the interaction of the A-SRR's trapped mode feature to that of the molecular resonances of the PMMA. Unfortunately, little success has been obtained in modeling the molecular resonance of the PMMA at different positions and an incomplete understanding of the above effects remains. A detailed investigation onto this is in progress. Therefore; since

no simulation based result can be obtained to corroborate the above experimental result, the description of the above effect still remains a hypothesis.

The peaks obtained in the reflectance spectra of Figure 5.8 (a-g) are identified and assigned from references [13-16] - and are shown in Table 5.1

| **Peaks** | **Wavelengths (micrometers)** | **Assignments** |
|---|---|---|
| **a** | 3.42 | Stretching vibration mode of $CH_3$ and $CH_2$ |
| **b** | 4.2 ~ 4.3 | Presence of atmospheric $CO_2$ (non PMMA feature) |
| **c** | 5.71 | Free carbonyl bond |
| **d** | 5.89 | Carboxylic group of PMMA |
| **e** | 6.07 | C=C double bonding between two carbon atoms in the main chain |
| **f** | 6.63 | $CH_3$ bending |
| **g** | 6.89 | In-Phase bending vibration of $CH_3$ |

**Table 5.1:** Assignments of PMMA peaks obtained when localised near the centre of A-SRR arrays.

From Figure 5.8 it is seen that the localised PMMA in almost at the right place in the centre with one rectangle per ring ~1/20 of area covered but it has still enhanced the signal. It is estimated that the amount of material detected (PMMA) is 2.62 % of the whole volume covered by the A-SRRs.

Thus, it could be said that by localisation of the PMMA at specific points, it is possible to enhance the sharpness of the carbonyl signature more that when it is spun uniformly all over. At the same time localisation enhances other weaker resonances of the PMMA that usually remains undetectable with uniform coating and when other than the centre localised at different positions.

The use of localisation allows less material to be detected, since a small area is covered - as opposed to the full substrate. The most obvious place to localise the material is near the ends of sections of the asymmetric rings or between the splits in the rings, since this region appears to be where the field is strongest. However, from Figure 5.8 it can be seen that a substantially greater enhancement occurs when the material to be sensed and characterised is placed close to the centre of the asymmetric rings. This position allows coupling of the sensed material with the so-called trapped resonance mode in which the incoming light is effectively trapped by the split ring structure. In turn, this localisation effect allows greater interaction with the material - and hence, greater spectroscopic sensitivity. For the enhancement to occur, the size of the A-SRRs must be closely matched so as to produce a trapped mode close to spectral resonances of the material of interest.

## 5.6 Conclusions

In this chapter, two different sensing effects have been demonstrated that use A-SRRs: firstly the shift in the resonance due to the dielectric properties of the PMMA and secondly the change in line shape produced by matching the A-SRR resonances to a molecular resonance. Further enhancement is achieved by localising the PMMA block near the centre of the A-SRRs for effective coupling with the trapped mode resonance.

### Acknowledgement

The author wishes to express his gratitude to Dr. Scott McMeekin of Glasgow Caledonian University for the carrying out the modelling of all the fabricated structures shown in this chapter and for discussions regarding the analysis of the results.

# References

1. C. Debus and P. H. Bolivar, “Frequency selective surfaces for high sensitivity terahertz sensing,”Appl Phys Lett. 91, 184102 (2007).

2. C. Debus and P. H. Bolivar, “Terahertz biosensors based on double split ring arrays,” Proc. SPIE. 6987, 6987(OU) (2008).

3. V. A. Fedetov, M. Rose, S. L. Prosvirnin, N. Papasimakis and N. I. Zheludev, “Sharp Trapped-Mode Resonances in Planar Metamaterials with a Broken Structural Symmetry,” Phys Rev Lett. 99, 147401 (2007).

4. F. Neubrech, A. Pucci, T.W. Cornelius, S. Karim, A. Garcia-Etxarri, J. Aizpurua,“ Resonant Plasmonic and Vibrational Coupling in a Tailored Nanoantenna for Infrared Detection,” Phys Rev Lett. 101, 157403 (2008).

5. M. Brucherseifer, M. Nagel, P. H. Bolivar, H. Kurz, A. Bosserhoff, and R.Büttner, “ Label-free probing of the binding state of DNA by time-domain terahertz sensing,” Appl. Phys. Lett. 77, 4049 (2000).

6. J. Aizpurua, T. Taubner, F. Javier Garcia de Abjo, M. Brehm, R. Hillenbrand,“ Substrate-enhanced infrared near-field spectroscopy,” Opt. Express 16, 1529 (2008).

7. J. F. Federici, B. Schulkin, F. Huang, D. Gary, R. Barat, F. Oliveira, and D.Zimdars, “THz imaging and sensing for security applications - explosives, weapons and drugs,” Semicond. Sci. Technol. 20, S266 (2005).

8. B. Lahiri, A. Z. Khokhar, R.M. De La Rue, S. G. McMeekin and N.P. Johnson, “Asymmetric split ring resonators for optical sensing of organic materials,” Opt. Express 17, 2 (2009).

9. D.H. Williams and I. Fleming, *Spectroscopic methods in Organic Chemistry* (McGraw Hill Publications, 2nd Edition 1973), Chap. 2.

10. L-H. Lee and, W-C. Chen, "High-Refractive-Index Thin Films Prepared from Trialkoxysilane-Capped Poly(methylmethacrylate)-Titania Materials," Chem. Matter. 13, 1137-1142 (2001).

11. A. Balamurugan, S. Kannan, V. Selvaraj and S. Rajeswari, "Development and Spectral Characterization of Poly (Methyl Methacrylate) /Hydroxyapatite Composite for Biomedical Applications," Trends Biomater. Artif. Organs, 18 (1), 41 (2004).

12. P. S. Nunes, N. A. Mortensen, J. P. Kutter, and K. B. Mogensen, "Photonic crystal resonator integrated in a microfluidic system," Opt. Lett. 33, 14 1623-1325 (2008),

13. C. Wochnowski, S. Metev, G. Sepold, "UV-laser-assisted modification of the optical properties of polymethylmethacrylate," Appl. Surface Science 154, 706 (2000).

14. F.Z. Tighilt, N. Gabouze, S. Sam, S. Belhousse, K. Beldjilali, " Morphology and specific interaction of PMMA coating with the surface of porous silicon," Surface Science 601, 4217 (2007).

15. M. K. Abyaneh, R. Pasricha, S. W. Gosavi and S. K. Kulkarni, "Thermally assisted semiconductor-like to insulator transition in gold-poly(methyl methacrylate) nanocomposites," Nanotechnology 17, 4129 (2006).

16. J. Wang, X. Ni, "Interfacial structure of Poly (methyl methacrylate)/TiO2 Nanocomposites Prepared Through Photocatalytic Polymerisation," Journal of Appl. Polymer Science 108, 3552 (2008).

# Chapter 6

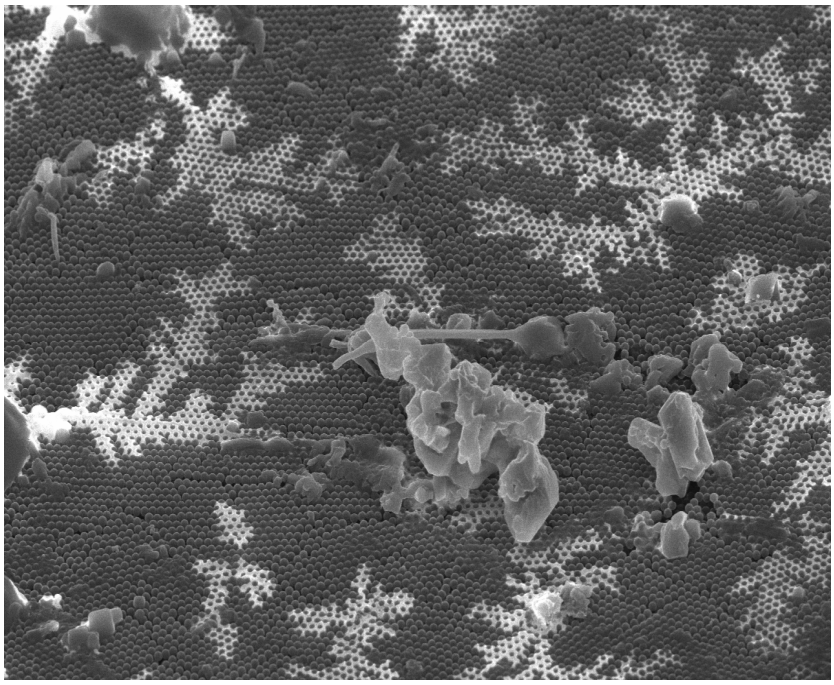

# Asymmetric split ring resonators (A-SRRs) for label-free optical biosensing of DNA oligonucleotides

From the previous two chapters, it is clear that Asymmetric split ring resonators (A-SRRs) display excellent Q-factor resonances, in the mid-infrared frequency range, that can be utilised for the detection of very thin layers of organic compounds. In this chapter the use of A-SRRs for the detection and differentiation of two different DNA (deoxyribonucleic acid) oligonucleotides is described. Oligonucleotides are short polymer chains of nucleic acid comprising twenty or fewer bases. Nucleotides, on the other hand, are molecules that form the structural units of DNA and RNA (ribonucleic acid). DNA molecules are known to exhibit molecular resonances in the mid infrared range. In this chapter the resonance of the A-SRR was tuned to match those of the DNA molecules - for accurate and label-free detection of DNA oligonucleotides. This method offers considerable potential for the creation of A-SRR based optical biosensors for different types of biomedical application.

## 6.1 Introduction

For many applications, e.g. security, forensic analysis and immuno-sensing, sensitive detection of minute amounts of chemical and biochemical substances is required [1-4]. Many of the presently available techniques for this purpose are expensive and can only be performed in specialised laboratories [2]. It is therefore highly desirable to perform inexpensive screening tests that can be carried out, almost anywhere, for preliminary detection - before referring to a specialised laboratory. There is therefore also a need to develop a low cost and portable detection system that offers high sensitivity and accuracy in the detection of various organic/biochemical compounds (e.g. changes occurring in patients' blood for early diagnosis of disease, signatures of toxins, pathogens etc).

In recent years there has been extensive development of biomolecular sensing [5-6]. Advances made in the immobilization of biomolecules onto patterned surfaces have contributed enormously towards biosensors that can detect DNA [6]. The two main methods available for the detection of DNA molecules (strands) are direct sequencing and DNA hybridization [7]. DNA hybridization is a comparatively simple approach and involves using a known single strand of DNA oligonucleotide as a probe material to find the hybridization state of the unknown DNA strand [7]. Fluorescent labelling is the most common method for the hybridization detection of unknown DNA strands [7-8]. Unfortunately, the fluorescent labeling method is not only complicated and time consuming, but also modifies the DNA strands, thereby lowering the accuracy of detection. At the same time, the fluorescent labelling approach suffers from other disadvantages such as label degradation, labelling yield fluctuation, site dependency of

fluorescent labels, and other factors [7-8]. All these disadvantages make the fluorescent labelling approach less efficient for accurate and precise analysis, as is required in important applications fields such as cancer research [7-8].

It is therefore desirable to develop alternate methods for quick and accurate, label-free detection of DNA molecules. Previous studies of both a theoretical and an experimental nature have shown that DNA molecules exhibit a large number of resonances in the mid-infrared region, primarily due to their phonon or plasmon modes [9-12]. The literature on label-free detection of DNA molecules is fairly sparse. Bolivar *et al*. [7] and Brucherseifer *et al.* [8] have worked in this field and have shown the dependence of the binding states of DNA fragments on their dielectric properties in the lower terahertz frequency region. On the other hand, utilisation of SRRs for detection of DNA is fairly novel. Cubukcu *et al.* [13] have utilised split ring resonator (SRR) resonance to couple with the infrared vibrational modes of a self-assembled monolayer of octadecanthiol molecules present in the gap region of SRRs. Similarly, Zhang *et al.* [14] have reported on an 'Asymmetric Bowtie Nano-Colorsorter' working in the visible spectrum that '*may*' be used for wavelength-selective photodetection.

In this chapter, two different types of oligonucleotides of thymine and adenine bases (5'-TTT TTT TTT TTT TTT-3'- thiolmodifier C3 CpG and 5'-AAA AAA AAA AAA AAA-3'- thiolmodifier C3 CpG), in layers with thickness ~ 5 nm each, are immobilized (attached) on gold-based 1.7 µm diameter A-SRRs, fabricated on silica substrates. In all the FTIR spectra in this chapter, they are labeled as DNA-T and DNA-A respectively. As

seen in the previous chapter, by matching the A-SRR resonance with the molecular vibrational resonance of organic compounds a large enhancement could be obtained in the resultant response that is then utilised for optical biosensing. Exactly the same principle is used in the present chapter, where the A-SRR resonance is matched with the molecular vibrational resonances of the two different DNA oligonucleotides, in order to enable their accurate, label-free, detection and differentiation.

The Thymine molecule exhibits two different conformations [15]. The two different conformations of the Thymine molecule and the labelling of their atoms are taken from Rastogi *et al.* [15] - and are shown below in Figure 6.1. Resonance peaks from both conformations are observed in the experiments discussed later.

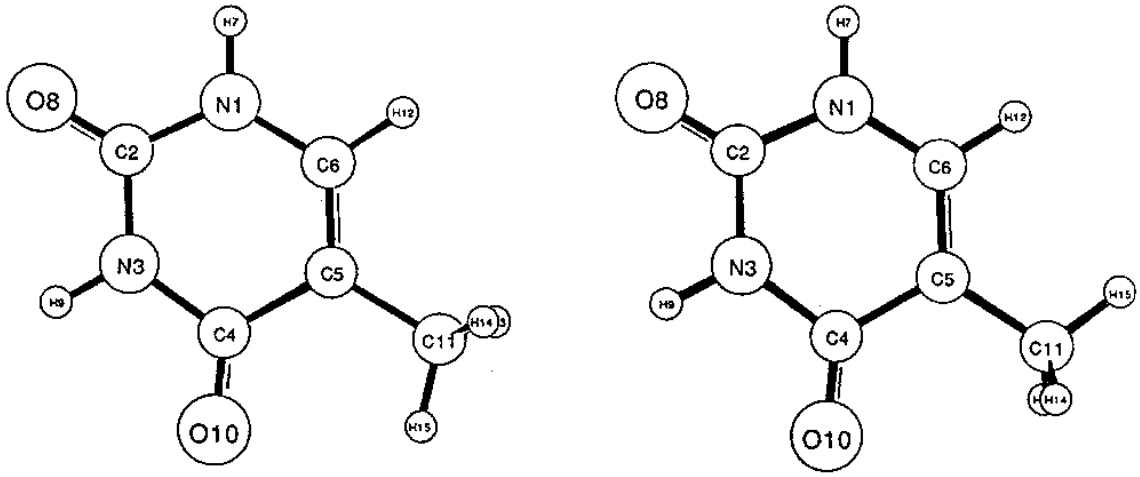


**Figure 6.1:** Conformations of Thymine molecule from reference [15].

The scheme of the Adenine molecule and the labelling of their atoms are referenced from Nowak *et al.* [16] and are shown below in Figure 6.2.

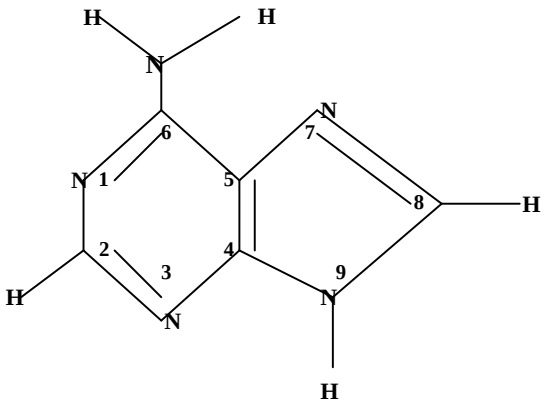


**Figure 6.2:** Schematic of Adenine molecules from reference [16].

## 6.2 Synthesis of DNA oligonucleotides

Oligonucleotides were synthesized using conventional phosphoramidite chemistry and purified by reverse-phase high-performance liquid chromatography (HPLC) (atdBio Ltd.). The sequences used are 5'-TTT TTT TTT TTT TTT-3'- thiolmodifier C3 CpG (Glen Research), and 5'-AAA AAA AAA AAA AAA-3'- thiolmodifier C3 CpG (Glen Research). Oligonucleotide concentrations were determined using extinction coefficients at a wavelength of 260 nm.

## 6.3 Immobilization of oligonucleotides

The immobilization of the oligonucleotides was performed by Dr.-Huabing Yin. Oligonucleotides were treated with 0.1 M dithiothreitol (DTT) in 0.1M $NaHCO_3$ at room temperature, for 1 hour, to activate thiol terminal groups. After the extra DTT was extracted with ethyl acetate, the oligonucleotides were de-salted using a Nap-10 column (Pharmacia) and freeze-dried to make a solution of designed concentrations. The substrate (A-SRR sample or a gold substrate) was then immersed in a 5 µM oligonucleotide solution (either T sequence or A sequence) in DI water at room temperature for 2 hours, followed by rinsing with DI water and $D_2O$. Schematics of the immobilization of DNA oligonucleotides on a gold substrate and on an A-SRR sample are shown in Figure 6.3.

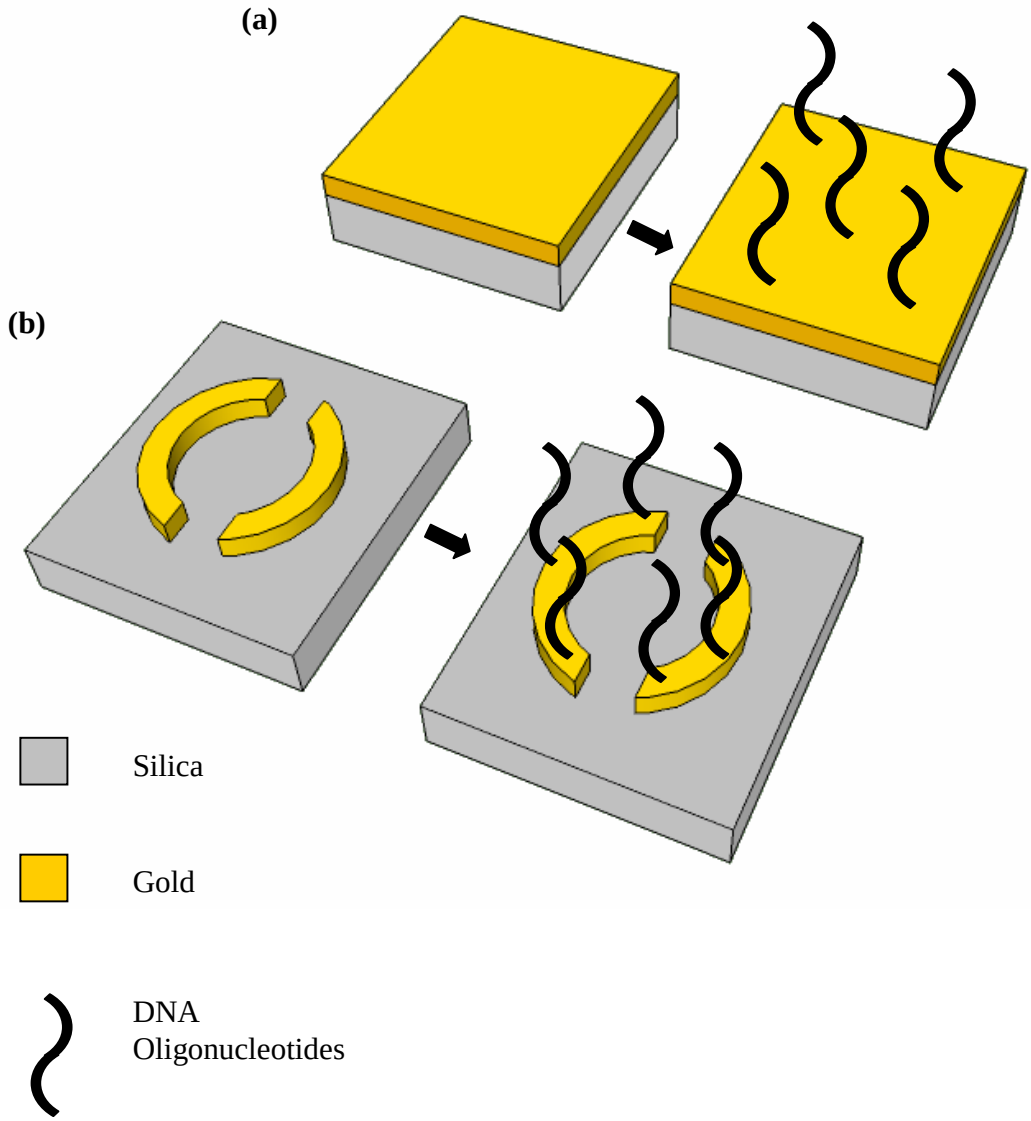


**Figure 6.3**: Schematic showing the immobilization of DNA oligonucleotides strands over the metallic A-SRRs with (a) DNA strands attaching themselves to uniform gold substrate and (b) DNA strands attaching themselves to the A-SRR.

## 6.4 Fabrication and Measurements

The fabrication and measurement techniques used in the work for this chapter are exactly the same as in the previous two chapters, involving electron beam lithography and FTIR tools. All spectra present in this chapter are given as a function of frequency specified in wavenumbers, in order to follow the norms of spectroscopic analysis methods. This consistency also helps in obtaining a ready comparison between the observed resonances and available references.

## 6.5 Results and discussions

In the detection of DNA oligonucleotides, two separate sets of experiments are carried out. In the first set of experiments, DNA oligonucleotide (Thymine-sequence) was immobilized over a 200 nm thick uniform gold substrate. An FTIR measurement was taken and a similar spectrum from a gold mirror substrate (without DNA) was subtracted from the spectrum. (In general the background was subtracted from the signal). This procedure was followed in order to bring out the specific features of the DNA attached to the gold surface.

In the second part of the same experiment, the same DNA oligonucleotide (a Thymine-sequence) was immobilized over an A-SRR sample. The FTIR spectrum of this sample was taken and then an A-SRR spectrum obtained without any DNA attached was subtracted from it. This procedure was also performed in order to bring out the features of the DNA attached to the A-SRR surface.

The resulting two different spectra (DNA on a gold-covered substrate and DNA on an A-SRR region) of the same DNA oligonucleotide (Thymine-sequence) were then compared. Figure 6.4 shows the two different spectra for comparison.

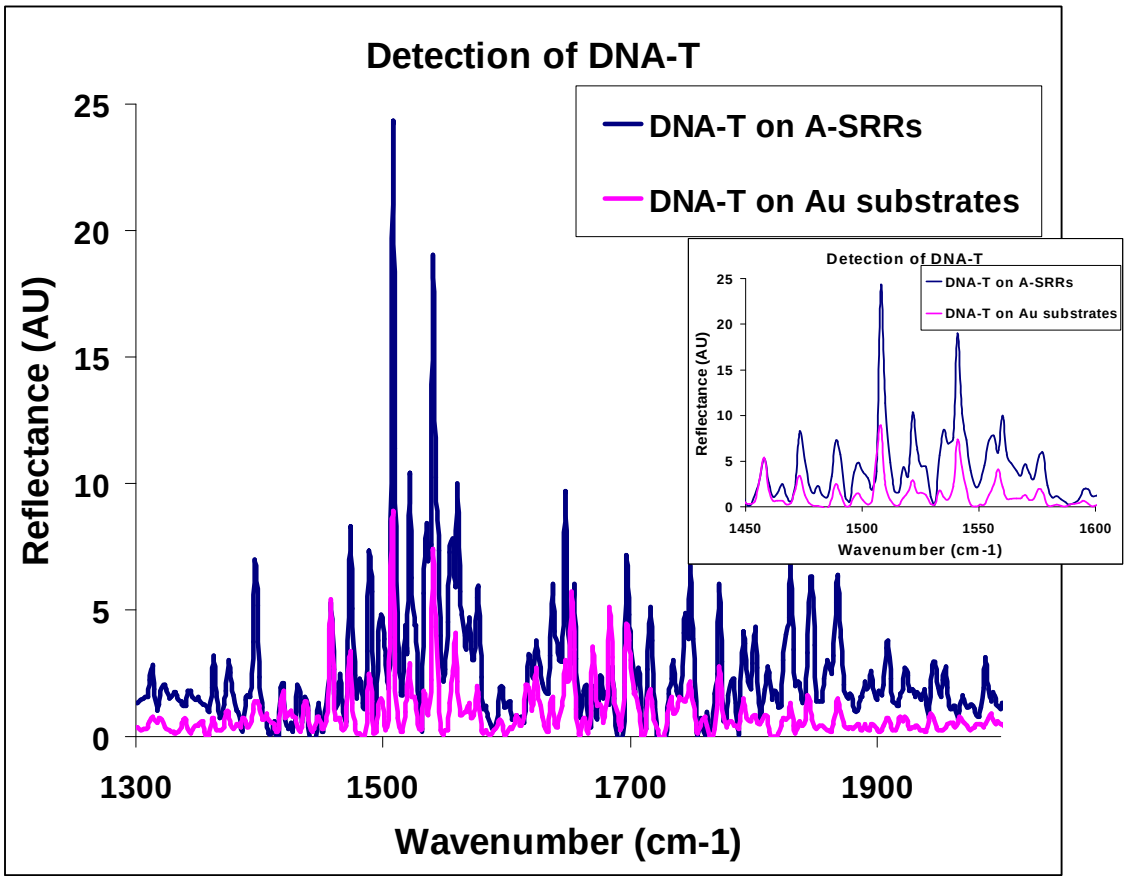


**Figure 6.4:** Enhancement of the DNA-T features by A-SRRs. The blue curve denotes the FTIR spectrum of DNA-T immobilized on A-SRRs. The pink curve denotes DNA-T immobilized on uniform gold substrates. DNA features can be seen in the same position for both samples, but much enhanced by the A-SRR sample when compared with the uniform gold substrate sample. The inset provides a more close-up view of the same spectra from 1450 $cm^{-1}$ to 1600 $cm^{-1}$. The assignments of the various peaks of the DNA-T features are given in table 6.1.

As shown in figure 6.4, the A-SRRs have enhanced the same DNA features by a factor of two or more when compared with the uniform gold substrate. This enhancement is due to the resonance of the A-SRRs matching with that of the molecular vibrational resonances of the DNA oligonucleotides. It is also observed that the FTIR spectra of DNA-T on an A-SRR array shows greater enhancement for the DNA feature around 1500 $cm^{-1}$ and 1800 $cm^{-1}$. This result is due to presence of the original A-SRR peaks at those wavenumbers. On the other hand, the DNA features around 1700 $cm^{-1}$ are not so prominent for the A-SRRs, due to the presence of the shoulder of the rising peak of 1800 $cm^{-1}$.This experiment establishes the superiority of A-SRR based biosensors over uniform metallic substrates in the detection of DNA oligonucleotides.

In the second set of experiments, two separate types of oligonucleotide (Adenine-sequence and Thymine-sequence) were immobilized on two similar A-SRR samples and the respective FTIR spectra from each sample were taken. A third A-SRR sample, similar to the previous two samples was then treated with the same solutions (DI water and $D_2O$) without immobilizing any DNA on it. The FTIR spectrum of this sample was taken and was compared with the previous two spectra of DNA attached onto the A-SRRs. This procedure was carried out in order to establish and differentiate between the resonance peaks of DNA and those of $D_2O$. The use of $D_2O$ instead of $H_2O$ in DNA FTIR spectroscopy is a standard practice and is used to differentiate the DNA spectra from the strong $H_2O$ based absorption bands present around 3 µm NIR wavelength range. The comparative spectra are shown in Figure 6.5

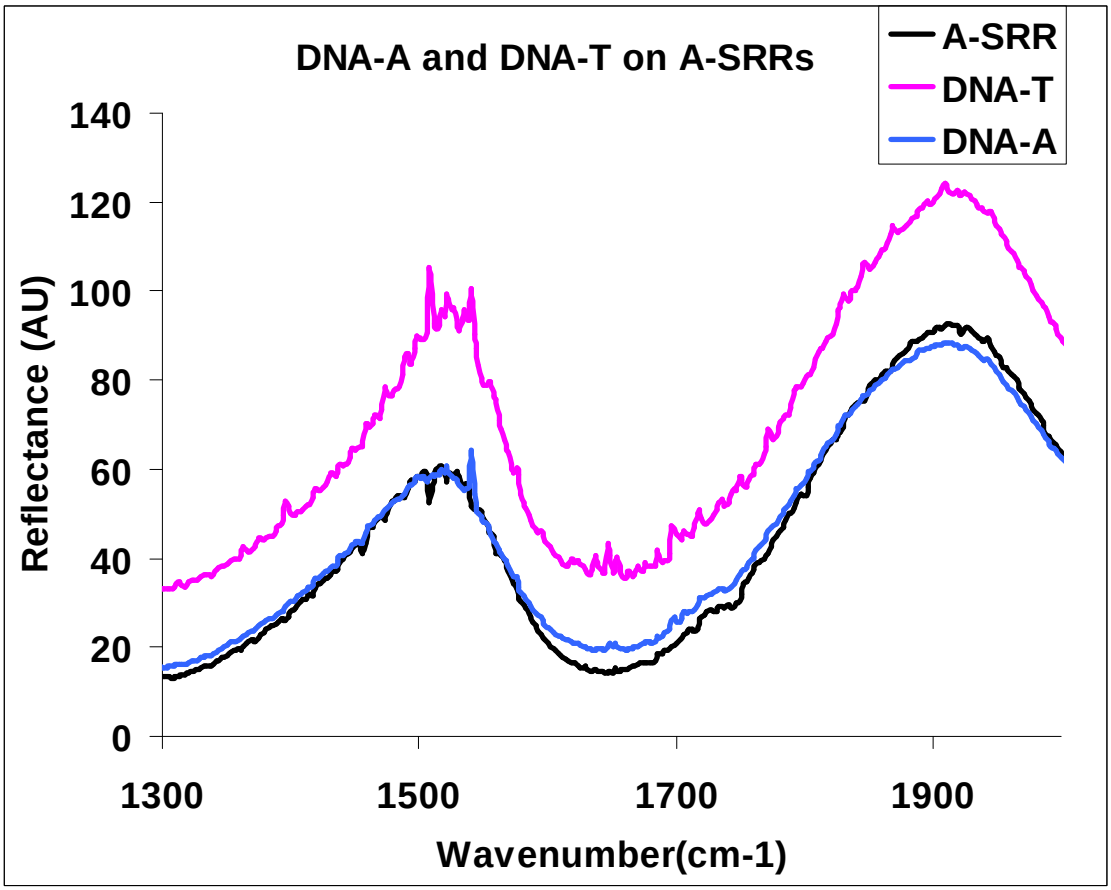


**Figure 6.5:** FTIR spectra taken from three different A-SRR samples. The black curve denotes an A-SRR sample treated sequentially with similar solutions (DI water and $D_2O$) but without any DNA immobilized on it. The pink curve denotes an A-SRR sample with DNA-T immobilized over it and the blue curve denotes an A-SRR sample with DNA-A immobilized over it.

In the final stage of this experiment, the non-DNA A-SRR spectrum was subtracted from the remaining two spectra of DNA immobilized over A-SRRs, in order to bring out the distinct DNA features. The result for detection of DNA-T is shown in Figure 6.6.

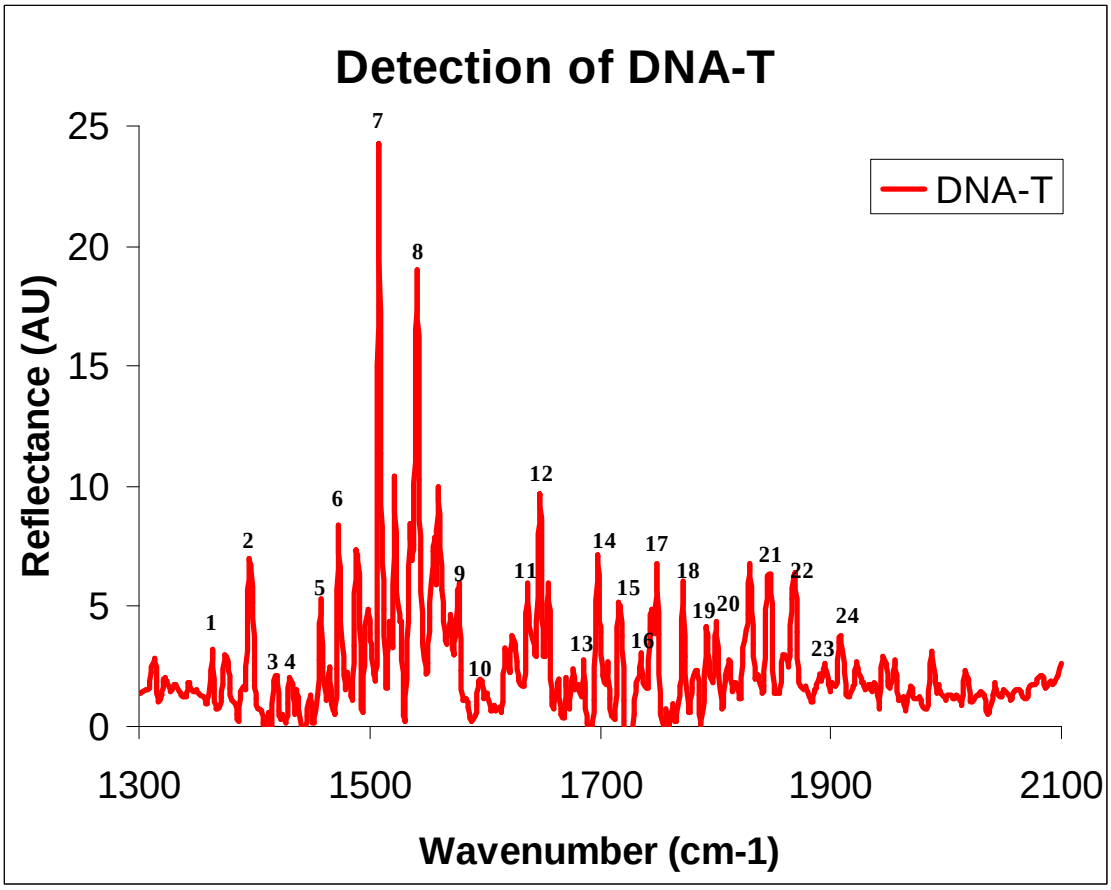


**Figure 6.6:** DNA-T spectra obtained by subtracting the A-SRR spectrum (black curve of figure 6.5) from the spectrum for DNA-T immobilized on A-SRRs (pink curves of figure 6.5), in order to bring out the different features of DNA-T. The assignments of the various peaks (1-24) are given in tables 6.1 from references [15-22].

The result for detection of DNA-A is shown in Figure 6.7.

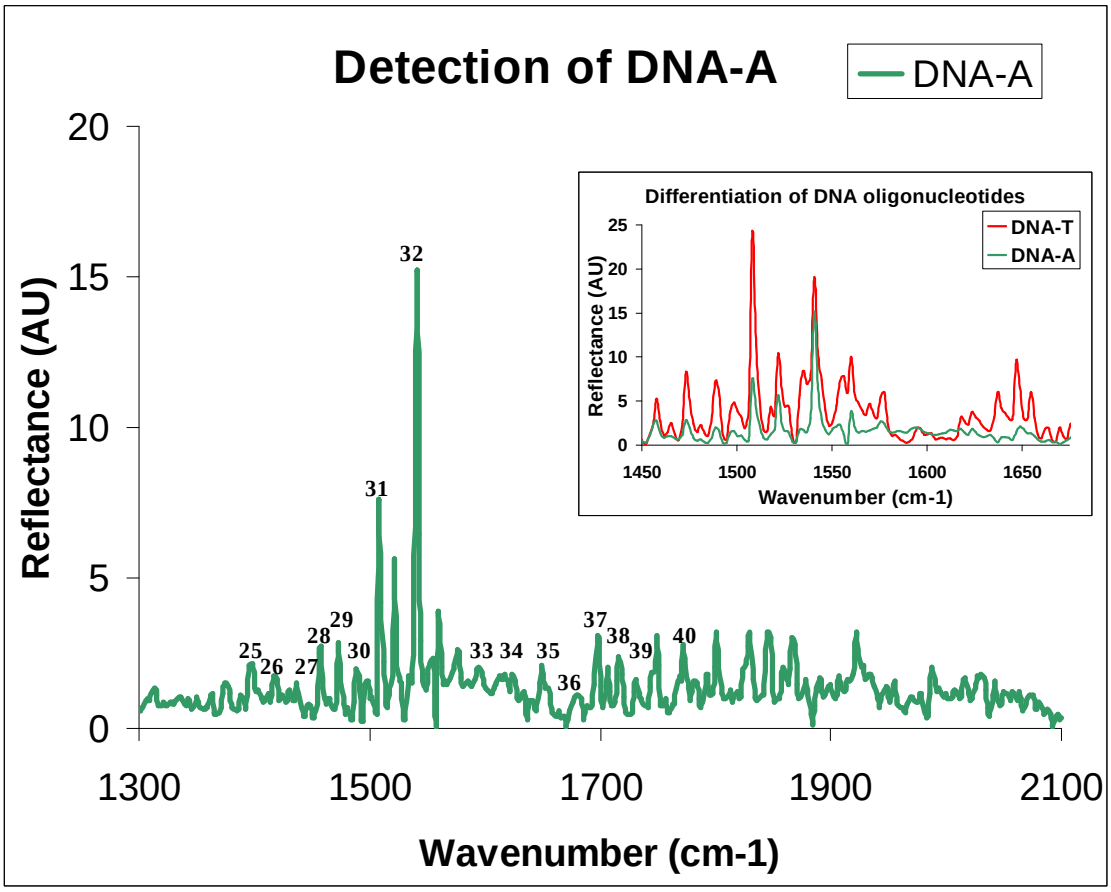


**Figure 6.7:** DNA-A spectra obtained by subtracting the A-SRR spectrum (black curve of figure 6.5) from the spectrum for DNA-T immobilized on A-SRRs (blue curves of figure 6.5), in order to bring out the different features of DNA-A. The assignments of the various peaks (25-40) are given in tables 6.2 from references [16, 23-30]. The inset shows a close-up comparison spectra of both DNA-T (red curve) and DNA-A (green curve) to illustrate that it is possible to differentiate between two different DNA strands using A-SRRs.

From Figure 6.6 and 6.7 it may be inferred that the A-SRRs are able not only to enhance the different DNA features but also make it possible to differentiate between two different types of oligonucleotide.

The peak features obtained in the FTIR spectra of DNA-T (red curve) of Figure 6.6 have been identified and assigned from references [15-22] - and are shown in Table 6.1. As noted earlier, both conformations for the Thymine molecule are observed.

| **DNA T features** | | |
|---|---|---|
| **Peak No.** | **Wavenumber ($cm^{-1}$)** | **Assignments** |
| 1 | 1363 | C6-H deformation. |
| 2 | 1400 | N3-H stretching. |
| 3 | 1419 | N3-H and C6-H in plane bending deformation. |
| 4-5 | 1436-1457 | Anti-symmetric stretching of $CH_3$. |
| 6 | 1473 | N1-H bending. |
| 7 | 1508 | N1-H angle and in-plane bending. |
| 8 | 1540 | C2=O stretching. |
| 9 | 1577 | N-H bending. |
| 10 | 1596 | $H_2O$ vibration. |
| 11 | 1637 | C=C stretching. |
| 12 | 1646 | C5=C6 ring vibration. |
| 13 | 1685 | C4=O8 stretching. |
| 14 | 1697 | C2=O2 stretching. |
| 15 | 1716 | C=C stretching. |
| 16 | 1735 | C2=O7 stretching. |
| 17 | 1749 | Carbonyl bond stretching. |

Continued onto next page

| Peak No. | Wavenumber ($cm^{-1}$) | Assignments |
|---|---|---|
| 18 | 1772 | C2=O stretching. |
| 19 | 1793 | C4=O stretching. |
| 20 | 1801 | C2=O8 stretching. |
| 21 | 1847 | C2=O stretching. |
| 22 | 1868 | C4=O, C5=C6 out of phase stretching. |
| 23 | 1895 | C4=O, C5=C6 in phase stretching. |
| 24 | 1909 | C2=O stretching. |

**Table 6.1:** Identification and assignments of the various peaks of DNA-T spectrum from references [15-22].

The peaks obtained in the FTIR spectra of DNA-A (green curve) of Figure 6.7 are identified and assigned from references [16, 23-30] and are shown in Table 6.2

| DNA-A features | | |
|---|---|---|
| **Peak No.** | **Wavenumber ($cm^{-1}$)** | **Assignments** |
| 25 | 1398 | Bending of N9-H, C2-H and C8-N9. |
| 26 | 1419 | Stretching of C4=C5 and C4-N9. |
| 27 | 1436 | C5-C6-N6 bending. |
| 28 | 1457 | N1=C6 stretching. |
| 29 | 1473 | N7=C8-H bending. |
| 30 | 1488 | N-H and C-H in plane deformation. |
| 31 | 1508 | N7=C8 stretching and C8-H bending. |

Continued onto next page

| | | |
|---|---|---|
| 32 | 1540 | C=N stretch. |
| 33 | 1598 | Stretching of $NH_{2.}$ |
| 34 | 1625 | C=N and C=C ring vibrations. |
| 35,36,37 | 1648,1681,1697 | Scissoring of $NH_{2.}$ |
| 38 | 1706 | C=O and C=C bending. |
| 39 | 1716 | C6-N6 stretching. |
| 40 | 1772 | Scissoring of $NH_{2.}$ |

**Table 6.2:** Identification and assignments of the various peaks of the DNA-A spectrum from references [16, 23-30].

## 6.6 Conclusions

A-SRRs have been used for the label-free detection of two different types of oligonucleotides. By matching the A-SRR resonance with the molecular vibrational resonance of DNA strands immobilised on them, enhanced detection as well as possible differentiation between two separate DNA oligonucleotides strands is obtained.

**Acknowledgement**

I am grateful to Dr. Huabing Yin for carrying out the processes for immobilizing the DNA strands onto the A-SRR and gold samples and for discussions regarding the analysis of the results

# Reference


1. B. Lahiri, A. Z. Khokhar, R.M. De La Rue, S. G. McMeekin and N.P. Johnson, "Asymmetric split ring resonators for optical sensing of organic materials," Opt. Express 17, 2 (2009).

2. J. F. Federici, B. Schulkin, F. Huang, D. Gary, R. Barat, F. Oliveira, and D.Zimdars, "THz imaging and sensing for security applications - explosives, weapons and drugs," Semicond. Sci. Technol. 20, S266 (2005).

3. C. Debus and P. H. Bolivar, "Frequency selective surfaces for high sensitivity terahertz sensing,"Appl Phys Lett. 91, 184102 (2007).

4. C. Debus and P. H. Bolivar, "Terahertz biosensors based on double split ring arrays," Proc. SPIE. 6987, 6987(OU) (2008).

5. J. Wang, "From DNA biosensors to gene chips", Nucl. Acids Res. 28, 3011-3016 (2000).

6. H. B. Yin, T. Brown, J. S. Wilkinson, R. W. Eason and T. Melvin, "Submicron patterning of DNA oligonucleotides on silicon," Nucl. Acids. Res. 32, 14, 1-7(2004).

7. P.H. Bolivar, M. Nagel, F. Richter, M. Brucherseifer, H. Kurz, A. Bosserhoff and R. Buttner, "Label-free THz sensing of genetic sequences: towards 'THz biochips'," Phil. Trans. R. Soc. London A, 362, 323-335 (2004).

8. M. Brucherseifer, M. Nagel, P.H. Bolivar and H. Kurz, A. Bosserhoff and R. Buttner, "Label-free probing of the binding state of DNA by time-domain terahertz sensing," Appl. Phys. Lett. 77, 24, 4049-4051 (2000).

9. L.L. Van Zandt and V.K. Saxena, “Millimiter-microwave spectrum of DNA-six predictions for spectroscopy,” Phys. Rev. A, 39, 2672-2674 (1989).

10. W. Zhuang, Y. Feng and E.W. Prohofsky, “Self-consistent calculation of localized DNA vibrational properties at a double-helix-single-strand junction with anharmonic potential,” Phys. Rev. A, 41, 7033 (1990).

11. H. Urabe and Y.Tominaga, “Low frequency Raman spectra of DNA,” Biopolymers 21, 2477-2481 (1982).

12. A. G. Markelz, A. Roitberg and E.J. Heilweil, “Pulsed terahertz spectroscopy of DNA, bovine serum albumin and collagen between 0.1 and 2.0 THz,” Chem. Phys. Lett. 320, 42-48 (2000).

13. E. Cubukcu, S. Zhang, Y-S. Park, G. Bartal, and X. Zhang, “Split ring resonator sensors for infrared detection of single molecular monolayers,” Appl. Phys. Lett. 95, 043113 1-3 (2009).

14. Z. Zhang, A. Weber-Bargioni, S. W. Wu, S. Dhuey, S. Cabrini and P. J. Schuck, “Manipulating Nanoscale Light Fields with the Asymmetric Bowtie Nano-Colorsorter,” Nanoletters 9,12, 4505-4509 (2009).

15. V. K. Rastogi, C. Singh, V. Jain and M. A. Palafox, “FTIR and FT-Raman spectra of 5-methyluracil (thymine),” J. Raman Spectrosc. 31, 1005–1012 (2000).

16. M. J. Nowak, L. Lapinski, J. S. Kwiatkowski and J. Leszczynski, “Molecular Structure and Infrared Spectra of Adenine. Experimental Matrix Isolation and Density Functional Theory Study of Adenine $^{15}$N Isotopomers”, J. Phys. Chem. 100, 3527-3534 (1996).

17. S. Missailidis and R. E. Hester, “FTIR spectra of Deoxyoligonucleotide-Noglamycin Complexes,” Biospectroscopy, Vol. 1, 91-99 (1995).

18. S. H. Brewer, S. J. Anthireya, S. E. Lappi, D. L. Drapcho and S. Franzen, “Detection of DNA Hybridization on Gold Surfaces by Polarization Modulation Infrared Reflection Absorption Spectroscopy,” Langmuir. 18, 4460-4464 (2002).

19. K. Szczepaniak, M. M. Szczesniak, and W. B. Person, “Raman and Infrared Spectra of Thymine. A Matrix Isolation and DFT Study”, J. Phys. Chem. A**,** 104, 3852-3863 (2000).

20. J. S. Singh, “FTIR and Raman spectra and fundamental frequencies of biomolecule: 5-Methyluracil (thymine),” J. Molec. Struct. 876, 127-133 (2008).

21. C. Dagneaux, J. Liquier, and E. Taillandier, “FTIR Study of a Nonclassical $dT,_{*}dA_{10}$-$dT_{10}$ Intramolecular Triple Helix”, Biochemistry**,** 34**,** 14815-14818 (1995).

22. M. Aida, M. Kaneko, M. Dupuis, T. Ueda, K. Ushizawa, G. Ito, A. Kumakura, M. Tsuboi, “Vibrational modes in thymine molecule from an ab initio MO calculation”, Spectrochimica Acta Part A. 53, 393-407 (1997).

23. M. Banyaya, M. Sarkarb, A. Graslund, “A library of IR bands of nucleic acids in solution”, Biophysical Chemistry. 104, 477–488 (2003).

24. J. Maranon, J.R. Grigera, “Variable charge molecular dynamics simulation-adenine molecule in water”, J.of Molec. Struct. (Theochem). 490, 243–248 (1999).

25. M. Tsuboi, “Application of Infrared Spectroscopy to Structure Studies of Nucleic Acids”, Appl. Spectroscopy Rev. 3, 1, 45-90 (1970).

26. G. I. Dovbeshko, V. I. Chegel, N. Y. Gridina, O. P. Repnytska, Y. M. Shirshov, V. P. Tryndiak, I. M. Todor, G. I. Solyanik, “Surface Enhanced IR Absorption of Nucleic Acids from Tumor Cells: FTIR Reflectance Study”, Biopolymers (Biospectroscopy), Vol. 67, 470–486 (2002).

27. L. E. Bailey, R. Navarro, A. Hernanz, “Normal Coordinate Analysis and Vibrational Spectra of Adenosine”, Biospectroscopy Vol. 3, 47-59 (1998).

28. M. Majoube, “Vibrational Spectra of Adenine and Deuterium-Substituted Analogues”, J. of Raman Spectrspy. Vol. 16, 98-110 (1985).

29. J. Florih, P. Mojzei and J. Stepinek, “Scaled Quantum Mechanical Force Fields and Vibrational Spectra of Solid-state Nucleic Acid Constituents.3.2-Aminoadenine”, J. Phys. Chem**.** Vol. 96, 9278-9282 (1992).

30. M. Majoube and P. Millie, P. Lagant and G. Vergoten, “Resonance Raman Enhancement for Adenine and Guanine Residues”, J. of Raman Spectrspy. Vol. 25, 821-836 (1994).

# Chapter 7

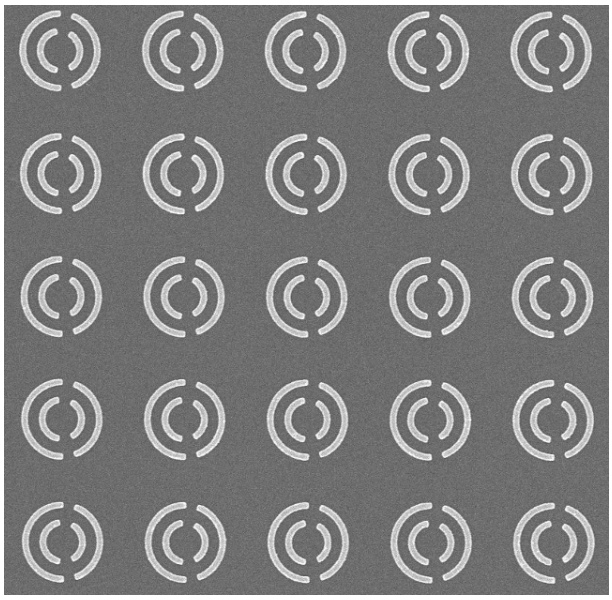

# Future work suggestions, summary and conclusions

This is the final and concluding chapter of this thesis. This chapter describes work that is still in progress and yet not been fully and comprehensively analysed and explained. As suggested in chapter 4, the effect of the periodic arrangement of A-SRRs in an array on their overall response has not been considered. Here, an attempt made to understand the impact of periodic arrangements on the A-SRRs responses. This chapter also describes the double A-SRRs (DA-SRRs). The DA-SRRs contains four concentric arcs of different sizes. The two smaller arcs form the inner A-SRRs which are concentric with the two larger arcs forming the outer A-SRRs. It is observed that the DA-SRRs produce a steeper response of high amplitude than single A-SRRs. Finally, a suggestion is made to add functionality to the SRRs with the use of silicon substrate. Silicon being an active material; its resonance response can be controlled by applying an external optical pulse to excite free charge carriers. These free charge carriers can short out the SRR gap, thereby turning off the LC resonance. This process provides a switching mechanism for dynamic control / tunability over the resonant response of SRR based metamaterials. The overall summary and conclusions of the entire thesis is presented at the end.

## 7.1 Impact of different lattice spacing on the overall response of A-SRRs

As shown in chapter 4, the two asymmetric arcs of the A-SRR (left-hand arc and right-hand arc) interact with each other and produce a steep response. However, since the A-SRRs (or any SRRs) are arranged in an array structure, there is a strong possibility of similar interaction between the nearest neighbours. Papasimakis *et al.* [1] has shown that by introducing random disorder into the array arrangement of A-SRRs, their characteristic response disappears. But there is no mention of what happens by changing the periodic arrangements and the lattice spacing between the A-SRRs. In this experiment the period/lattice spacing (a) of the A-SRRs (centre to centre distance between two nearest neighboring A-SRRs) is varied and its overall impact on the resonance is observed. All other factors including the diameters of A-SRRs are kept constant at 1.25 µm in all cases. A square periodic arrangement is maintained throughout. Figure 7.1 shows the SEM image of one such array.

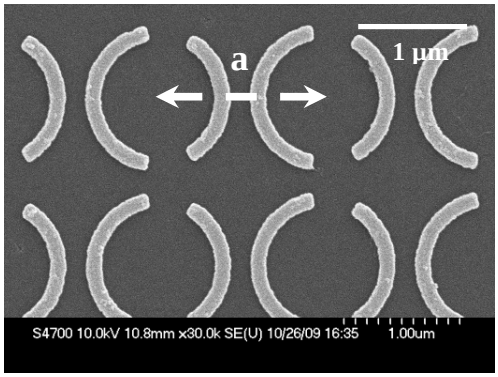


**Figure 7.1:** SEM image of A-SRR array with the period/lattice spacing (a) of 1.45 µm. In all of the subsequent experiments the period (a) is increased keeping all other parameters constant. A square periodic arrangement is maintained throughout.

Figure 7.2 provides the response of A-SRR arrays with different lattice spacing.

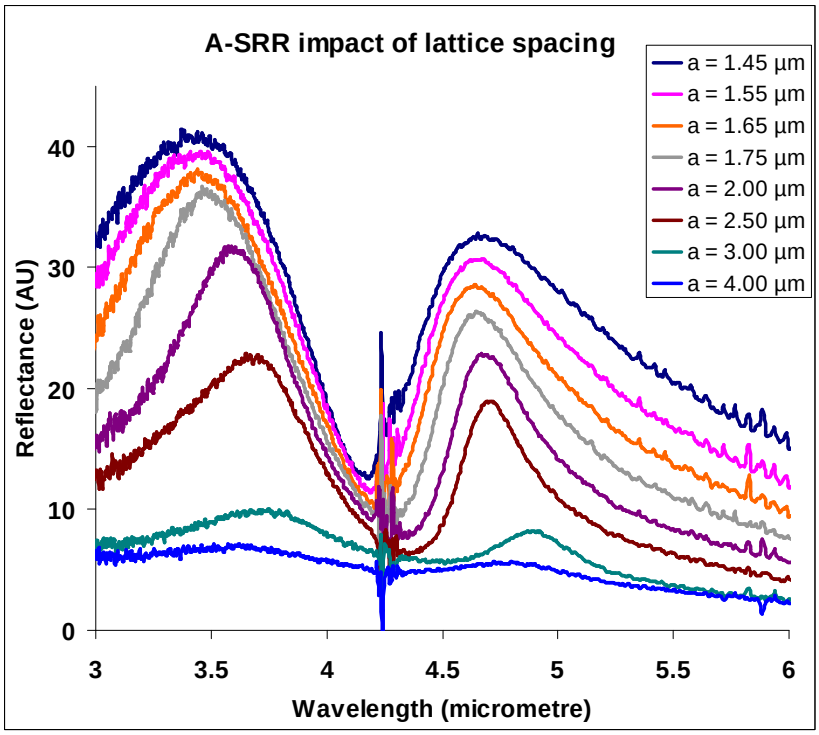


**Figure 7.2:** Reflectance spectra of A-SRRs with increasing lattice spacing (a). It could be seen that by increasing the lattice spacing (a) there is an almost linear decrease in amplitude of resonance. At the same time, the line width of both the resonance peaks gets narrower with increase in lattice spacing till they reach an optimum value for (a).

From Figure 7.2 it is observed that as the lattice spacing between the A-SRRs increased, their reflectance amplitude goes down linearly. On the other hand, both the resonances (longer and shorter wavelength) becomes narrower by increasing the lattice spacing up to a certain point and then starts to broaden again. Therefore, it could be inferred that the lattice spacing in the A-SRRs has an optimal value, at which the linewidth of the resonance peaks are narrowest (with highest Q-factor), which becomes broader with any change (increase or decrease) in the lattice spacing. As the period of the A-SRRs is increased the whole array becomes dilute (sparse) with less and less metal per unit cell.

This results in reduction of the reflectance amplitude with increased lattice spacing. In Figure 7.3 the reflectance amplitude of the asymmetric mode (longer wavelength peak) is plotted with respect to the lattice spacing.

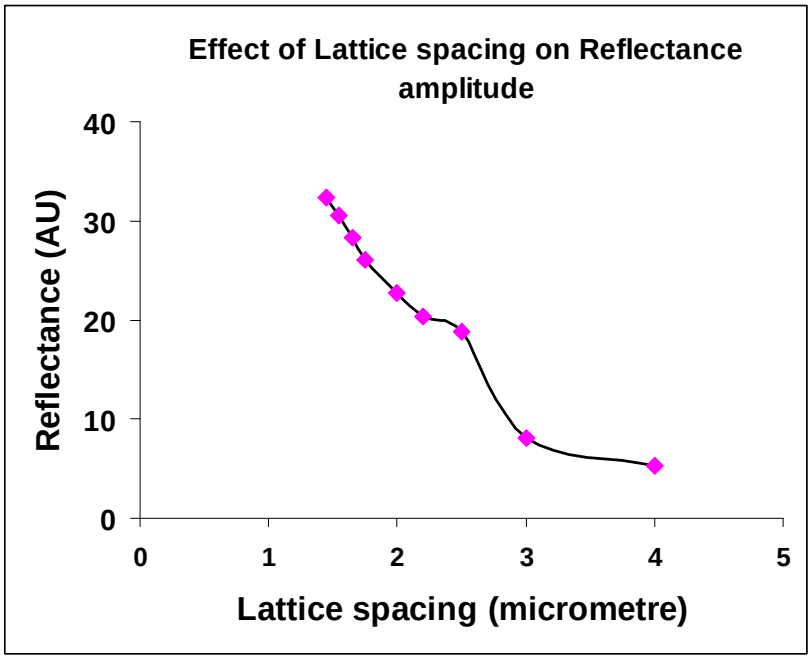


**Figure 7.3:** The reflectance of A-SRR array as a function of the lattice spacing (a) at the longer wavelength peak. It could be seen that by increasing the lattice spacing the reflectance of the array reduces almost linearly.

In Figure 7.4 the Q-factor of the asymmetric mode (longer wavelength peak) is compared with the lattice spacing of the A-SRRs.

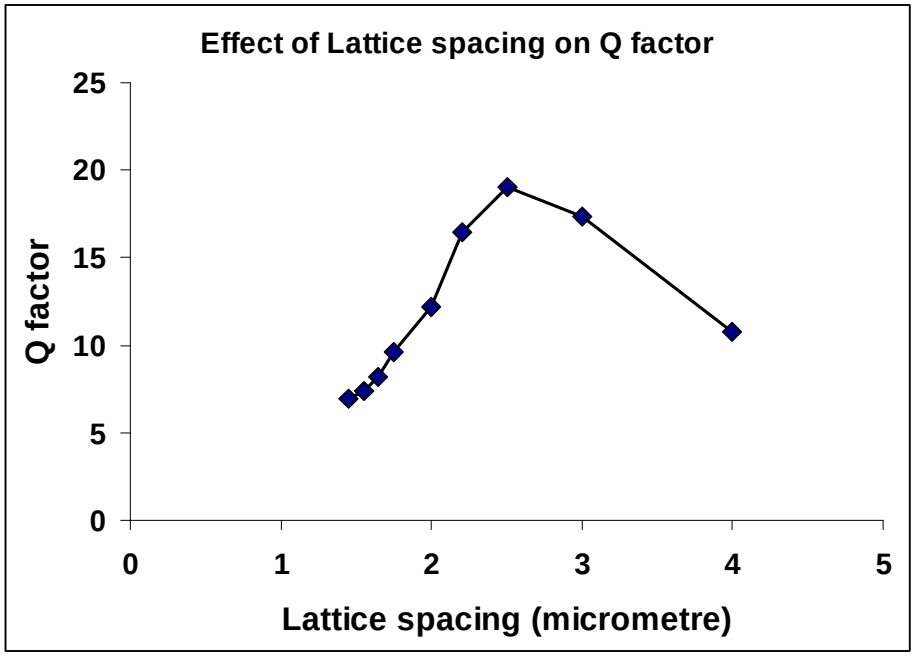


**Figure 7.4:** Plot of Quality factor of A-SRR's longer wavelength resonance peak with respect to the lattice spacing of the array. The highest Q-factor is achieved at a period of 2.5 µm that is the exact double the A-SRR diameter.

From Figure 7.3 the quality factor achieves its highest value at a lattice spacing of 2.5 µm after which it progressively reduces. Now, 2.5 µm is exactly double the A-SRR diameter of 1.25 µm. So, the best quality factors are achieved when the following condition is fulfilled.

$$a = 2d \qquad (7.1)$$

Where $a$ is the period of the A-SRRs and $d$ is the diameter.

Thus, the A-SRR array achieves the highest Q-Factor for its asymmetric mode (longer wavelength resonance) when each A-SRR is separated by the exact same distance as its diameter, from its nearest neighbour. The Q-Factor of the symmetric mode (shorter wavelength resonance) behaves similarly.

The explanation for this can be taken from Chapter 4. When two nearest neighbouring A-SRRs are separated almost by their diameter, for both asymmetric and symmetric modes, the charges accumulated at the end of arcs are equidistant from one another. Thus, the interaction (charge oscillation) between the two arcs of the A-SRRs (left-hand arc and right-hand arc) becomes almost similar to the interaction between the arcs of the nearest neighbouring A-SRRs. In all other case, the interactions between nearest neighbouring arcs of A-SRRs are dissimilar to that of the interaction between themselves. Thus, the best response is obtained in an A-SRR array when individual A-SRRs resonate in the exact same manner as they resonate with their nearest neighbour.

The reason for the sudden shift of the resonance peaks for A-SRRs of a = 3 μm and above towards the longer wavelength is still unknown and a critical analysis of this is under progress. At the same time, other periodic arrangements such as hexagonal period, honeycomb period, quasi period etc are being explored to arrive at an optimal value for the Q-factor.

## 7.2 Double asymmetric split ring resonators (DA-SRRs)

In a double asymmetric split ring resonator (DA-SRR) there are two sets of A-SRRs (inner and outer) concentric to one another. The steep response produce by the inner A-SRR is further augmented by the outer A-SRR encircling it. Figure 7.4 shows the SEM image and the reflectance spectra of such a DA-SRR.

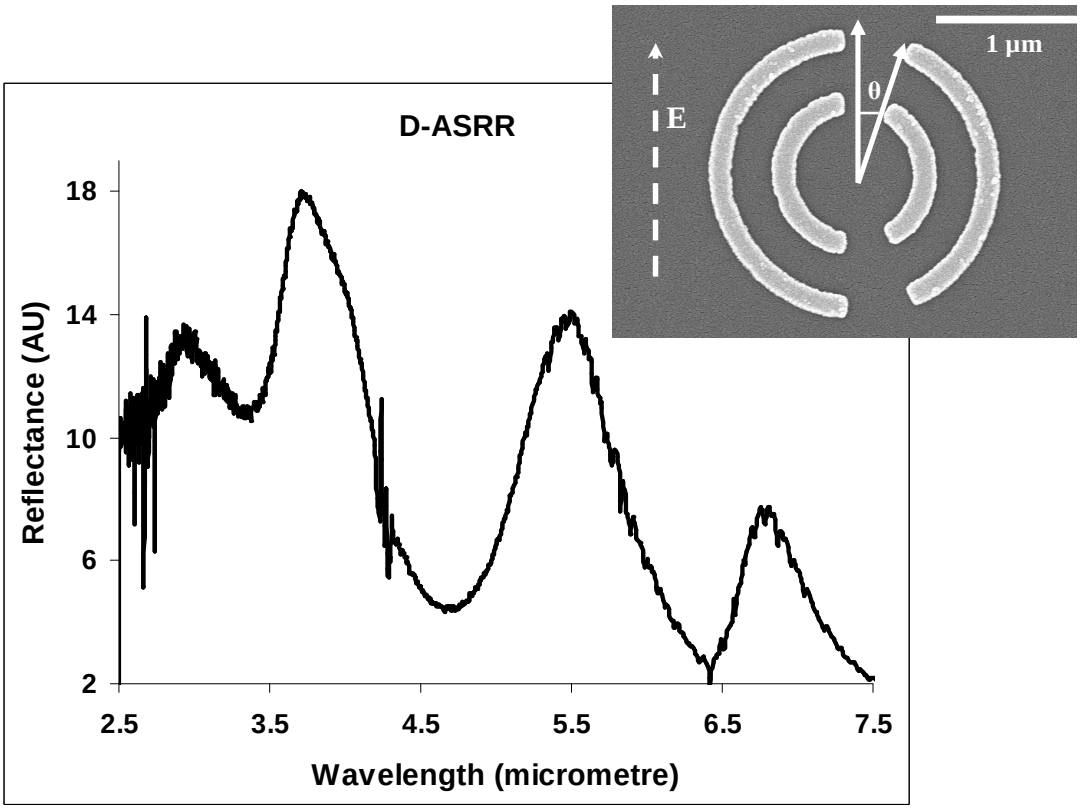


**Figure 7.4:** SEM image (inset) of a double A-SRR (DA-SRR) with a smaller (inner) A-SRR encircled by a larger (outer A-SRR) along with its corresponding reflectance spectra. The angular gaps between the inner and outer A-SRRs are kept constant at $\theta \sim 25^0$. The measurement is done for normal incidence with the E- field placed perpendicular to the gaps as shown by the dotted arrow.

As shown in Figure 7.4, all four different sized arcs of the DA-SRR interact among each other to produce four different resonance peaks. The resonance peak at 3.69 µm has both higher amplitude as well as higher Q-factor when compared with the shorter wavelength resonance of a single A-SRR. A detailed analysis of all these resonance peaks as well as the working of the DA-SRR is in progress.

## 7.3 Dynamic switching of SRR resonances at telecom frequencies

For many potential applications like secure short range communication, spectroscopic imaging etc it is require to create metamaterials with a tuneable response [2-3]. The objective here is to produce a switching mechanism for dynamic control / tunability over the resonant response of metamaterials in the telecom wavelength range. It has been observed that for metamaterials fabricated on semiconductor substrates, the resonance response can be controlled by applying external stimuli [2-5]. By applying an external optical pulse of suitable duration, repetitive rate and specific centre wavelength, to the substrate, free charge carriers can be excited. These free charge carriers short out the SRR gap, thereby turning off the LC resonance [2, 5]. This process is governed by optical generation, recombination and electrical transport of carriers and so the material selection and fabrication process are vital. By using femtosecond optical pulse, very fast switching is possible, which is a clear advantage over applying external voltage for somewhat similar effects.

The work done on the dynamic control of metamaterial properties is limited, with mostly performed in the low terahertz frequency range [2-3, 5]. No result has been shown so far, which depicts optical switching properties at telecom frequencies (~200 THz) for SRRs fabricated on semiconductor substrates. The SRRs described in this thesis (Chapter 2 and Chapter 3) are fabricated on the common semiconductor substrate of silicon, due to its availability, cost efficiency, fabrication tolerance, robustness and above all the favorable position it commands in the semiconductor industry. Both gold and aluminium metals have been used to fabricate the SRRs. The silicon substrate metallic SRRs fabricated here, demonstrates resonances at telecom frequencies. By using a laser of wavelength less than the band edge of silicon (< 1.1 μm) and focusing it on the SRR substrate, it is possible to generate large number of electron and hole pairs. The pumping power of the laser should be high so that enough photo-carriers are generated that shorts the SRR gap and thus, shunts the LC resonance. Since silicon is an indirect band gap semiconductor, indirect recombination is expected. The recombination process will occur in indirect transition via localised energy states in the forbidden energy gap.

Thus, it is believed that such a device would not only be unique in demonstrating control at high frequency for potential telecom applications but it would also be welcomed by the industry due to its simplicity in fabrication (with the use of aluminium). These are the two very clear and distinct advantages in fabricating metallic SRRs over silicon (semiconductor) substrates. A detailed working and investigation on all these experiments are in progress.

## 7.4 Summary and conclusions

As it has been shown throughout this thesis, that split ring resonator (SRR) based metamaterials display very interesting electromagnetic properties. In the first three chapters the fundamental workings and properties of nano-scale SRRs resonating in the (near and mid) infrared and the visible spectrum were presented with the effect of various metals and substrates considered. In the last three chapters of this thesis, the steep resonance response of asymmetric split ring resonator (A-SRRs) are utilised for the optical detection of very small amount of organic materials (PMMA) and biochemical substances such as oligonucleotides (DNA strands). Therefore, it can be concluded that metamaterials offer exciting and challenging possibilities for novel electromagnetic responses and hence, research is encouraged to continue to utilize their properties for various applications ranging from optical biosensing to telecommunication and more.

# References

1. N. Papasimakis, V. A. Fedotov, Y. H. Fu, D. P. Tsai and N. I. Zheludev, “Coherent and incoherent metamaterials and order-disorder transitions,” Phys. Rev. B, 80, 041102 1-4 (2009).

2. H.T.Chen, W.J. Padilla, J.M.O. Zide, Seth R. Bank, Arthur C. Gossard, Antoinette J. Taylor, R.D. Averitt, “Ultrafast optical switching of terahertz metamaterials fabricated on ErAs/GaAs nanoisland superlattices,”Optics Lett. 32, 12, 1620-1622 (2007).

3. W.J. Padilla, A.J. Taylor, C. Highstre, Mark Lee, R.D. Averitt, “Dynamic Electric and Magnetic Metamaterial Response at Terahertz Frequeicies,” Phys.Rev. Lett., 96, 107401 1-4 (2006).

4. Z. Sheng and V.V, Varadan, “Tuning the effective properties of metamaterials by changing the substrate properties,” J. Appl. Physics. 101, 014909 4-7 (2007).

5. H-T Chen, W. J. Padilla, J. M. O. Zide, A. C. Gossard, A. J. Taylor and R. D. Averitt, “Active terahertz metamaterial devices,” Nature, 444, 597-600 (2006).